République Algérienne Démocratique et Populaire

Ministère de l'enseignement supérieur et de la Recherche Scientifique

Université Ferhat Abbas -Sétif 1-



Institut d'Architecture et des Sciences de la Terre

Département des sciences de la terre

THÈSE PRÉSENTÉE EN VUE DE L'OBTENTION DU DIPLÔME DE DOCTORAT TROISIÈME CYCLE –LMD-

OPTION : Hydrogéologie

SUR LE THÈME :

Apport de la télédétection, du SIG, de l'hydrochimie et de la modélisation dans l'étude des ressources en eau dans la région de Sétif. Cas du bassin versant de Bousselam.

PAR :

Khemmal Hichem Yakoub

Devant le jury :

PRÉSIDENT:	**CHABOU Moulley Charaf**	**Pr. UFAS 01. SETIF**
DIRECTEUR DE THÈSE :	**HANI Azzedine**	**Pr. UBM. ANNABA**
EXAMINATEURS :	**DEMDOUM Abdeslam**	**Pr. UFAS 01. SETIF**
	BOUGHERIRA Nabil	**Pr. UBM. ANNABA**
	BOUDJEMA Sabrine	**MCA. UAB. TLEMCEN**

Année universitaire : 2025/2026

FERHAT ABBAS SETIF 1

DOCTORAL THESIS

Contribution of Remote Sensing, GIS, Hydrochemistry and Modeling to the Study of Water Resources in the Region of Sétif: Case Study — Northern Upper Bousselam

Author: Khemmal Hichem Yakoub
Khemmalhichem@gmail.com

Supervisor:Pr. Hani Azzedine
Haniazzedine@yahoo.fr

A thesis submitted in fulfillment of the requirements for the degree of Doctorat

in the

Institute of Architecture and Earth Sciences
GeologyEarth Sciences

January 6, 2026

FERHAT ABBAS SETIF 1

Abstract

Institute of Architecture and Earth Sciences
GeologyEarth Sciences

PhD Student

Contribution of Remote Sensing, GIS, Hydrochemistry and Modeling to the Study of Water Resources in the Region of Sétif: Case Study — Northern Upper Bousselam

by Khemmal HICHEM YAKOUB

Abstract

This thesis develops and applies an integrated, reproducible workflow—combining remote sensing, GIS, hydrochemistry and multi-criteria decision modeling—to delineate and understand groundwater recharge potential on the semi-arid high plateau of Sétif, Algeria. It begins with a detailed digitization of the regional geological map to characterize lithological units and aquifer materials. High-resolution ASTER GDEM v3 data are then hydro-conditioned in QGIS to derive drainage density and slope layers that quantify how terrain morphology governs the balance between infiltration and runoff. Concurrently, NASA-POWER precipitation and temperature records (1980–2019) are processed to generate spatially continuous annual rainfall and temperature surfaces. These surfaces reveal the onset of the recharge period and guide the timing of land-cover classification using Landsat 8 OLI/TIRS imagery at the moment when aquifer replenishment begins. Landsat 8 OLI/TIRS imagery—interpreted alongside the geological map—is also employed to extract structural lineaments that control subsurface flow pathways. Field-based hydrochemical investigations—including piezometric profiling, major-ion ratio analysis and total dissolved solids (TDS) measurements—trace recharge signatures in groundwater and provide empirical constraints for model calibration. Six thematic layers (lithology, lineament density, slope, drainage density, rainfall intensity and land cover) are weighted through the Analytic Hierarchy Process and overlaid in QGIS to produce a groundwater recharge potential zoning map. Independent split-sample ROC analysis and TDS-based thresholds confirm the model's ability to discriminate recharge-rich from recharge-poor zones. The results highlight the northern sector—characterized by high rainfall intensity, permeable formations and low drainage density—as the most promising target for recharge enhancement. By integrating geological, geomorphological, climatic and hydrochemical evidence, this methodology provides a robust decision-support tool for prioritizing field investigations and designing adaptive water-management strategies in semi-arid basins.

Résumé

Cette thèse développe et applique un protocole intégré et reproductible—combinant télédétection, SIG, hydrochimie et modélisation multicritère—pour délimiter et comprendre le potentiel de recharge des eaux souterraines sur le plateau aride de Sétif, Algérie. Elle débute par la numérisation détaillée de la carte géologique régionale afin de caractériser les unités lithologiques et les matériaux aquifères. Des données ASTER GDEM v3 à haute résolution sont ensuite hydro-conditionnées dans QGIS pour dériver les couches de densité de drainage et de pente, quantifiant l'influence de la morphologie du terrain sur l'équilibre infiltration/ruissellement. Parallèlement, les séries de précipitations et de températures NASA-POWER (1980–2019) sont traitées pour générer des surfaces spatiales annuelles de précipitations et de températures. Ces surfaces révèlent le début de la période de recharge et guident le moment de la classification de l'occupation du sol à partir des images Landsat 8 OLI/TIRS, au démarrage de l'alimentation de l'aquifère. Les images Landsat 8

OLI/TIRS—interprétées de concert avec la carte géologique—permettent également l'extraction de linéaments structuraux contrôlant les écoulements souterrains. Les investigations hydrochimiques sur le terrain—profilage piézométrique, analyse des rapports d'ions majeurs et mesures des solides dissous totaux (TDS)—mettent en évidence les signatures de recharge dans les eaux souterraines et apportent des contraintes empiriques pour la calibration du modèle. Six couches thématiques (lithologie, densité de linéaments, pente, densité de drainage, intensité pluviométrique et occupation du sol) sont pondérées selon le Processus d'Analyse Hiérarchique puis superposées dans QGIS pour produire une carte de zonage du potentiel de recharge. Une validation indépendante par analyse ROC en échantillonnage fractionné et des seuils basés sur les TDS confirment la capacité du modèle à discriminer zones à fort potentiel de recharge et zones à faible potentiel. Les résultats soulignent le secteur nord—caractérisé par une forte intensité pluviométrique, des formations perméables et une faible densité de drainage—comme la zone la plus prometteuse pour renforcer la recharge. En intégrant des données géologiques, géomorphologiques, climatiques et hydrochimiques, cette méthodologie offre un outil décisionnel robuste pour prioriser les campagnes de terrain et élaborer des stratégies de gestion adaptative de la ressource en eau dans les bassins semi-arides.

ملخص علمي

تطوّر هذه الأطروحة منهجية متكاملة وقابلة للتكرار لتحديد وتقييم إمكانات تغذية المياه الجوفية على الهضاب العليا شبه الجافة بولاية سطيف، الجزائر، عبر دمج أدوات [الاستشعار عن بعد] و[نظم المعلومات الجغرافية] و [الهيدروكيمياء] و[نمذجة اتخاذ القرار متعددة المعايير]. تبدأ العملية برقمنة الخريطة الجيولوجية الإقليمية لتوصيف الوحدات الليثولوجية ومواد الخزان، ثم معالجة نموذج الارتفاع الرقمي [ASTER GDEM v3] هيدرولوجيًا في بيئة [QGIS] لاشتقاق طبقات الانحدار وكثافة التصريف التي تتحكم في توازن [التسرب] مقابل [الجريان السطحي]. تُستخرج أسطح مكانية سنوية للهطول ودرجة الحرارة من سجلات [NASA POWER] (1980–2019) لتحديد بداية موسم التغذية وتوقيت تصنيف الغطاء الأرضي باستخدام صور [Landsat 8 OLI/TIRS] والتي تُستخدم أيضاً لاستخراج [الخطوط البنيوية] المؤثرة في مسارات الجريان تحت السطحي . تدعم بيانات الحقل الهيدروكيميائية — بما في ذلك ملفات القياس [البيزومتري]، تحليل نسب الأيونات، وقياسات المواد معايرة النموذج وتحديد بصمات التغذية
جُمعت ست طبقات موضوعية — ([TDS]) الصلبة الذائبة الكلية الليثولوجيا؛ كثافة الخطوط البنيوية؛ الانحدار؛ كثافة التصريف؛ شدة الهطول؛ الغطاء الأرضي) ووزنت باستخدام [عملية التحليل الهرمي AHP]
ثم دمجت في [QGIS] لإنتاج خريطة إمكانية تغذية المياه الجوفية
أظهرت اختبارات التحقق المستقلة (تحليل [ROC] وتقاطع عتبات [TDS]) قدرة جيدة على تمييز المناطق الغنية عن الفقيرة بالتغذية، مع بروز القطاع الشمالي كمنطقة واعدة لتعزيز التغذية بفضل هطول أعلى وتكوينات نفوذية وكثافة تصريف منخفضة. توفر المنهجية أداة دعم قرار كمية ومؤسسية لتحديد أولويات التحقيقات الميدانية وتصميم استراتيجيات إدارة مياه تكيفية في أحواض شبه جافة

Acknowledgements

This doctoral journey has been shaped by the guidance, patience, and generosity of many remarkable people.

I am deeply indebted to my supervisor, **Prof. Hani Azeddine**, whose insight, encouragement, and high standards have continually pushed me to refine my thinking and strengthen my work. His mentorship has been both a compass and a source of inspiration.

My heartfelt gratitude goes to my Family, whose unwavering belief in me has been my anchor through every challenge. Their sacrifices, patience, and love have sustained me far beyond the academic sphere.

I also wish to thank my friends and colleagues — within and beyond the **University of Ferhat Abbas Sétif 1, University of Kasdi Merbah Ouergla, and Badji Mokhtar Annaba** — for their camaraderie, stimulating discussions, and readiness to lend a hand, whether in the field, the lab, or over a much-needed coffee.

Special appreciation is due to the technical and administrative staff whose quiet efficiency ensured that the practical aspects of this research ran smoothly.

To all who have, in ways large and small, left their mark on this thesis — whether through advice, encouragement, or shared effort — I extend my sincere thanks. This work is as much a reflection of your contributions as it is of my own. ...

Contents

AbstractAbstract **iv**

Acknowledgements **vii**

1 Overview of the Study area **1**
1.1 Geographical context . . . 1
1.2 Vegetation Cover . . . 2
1.3 Hydrological Overview . . . 3
1.4 Climate . . . 4
1.5 Geology . . . 5
1.5.1 Local Geological Context . . . 6
Quaternary and Neogene Formations with Minimal Tectonization . . . 7
Continental Mio-Pliocene . . . 8
The Domain of Flyschs . . . 8
The Tellian Nappes . . . 8
Relative Autochthonous of Djebels Anini and Guergour; and the South Setifian Allochthonous Assembly . . . 11
Exotic or Extrusive Trias . . . 12
Sebkha Soils: . . . 12
1.6 Research Rationale and Objectives . . . 12
1.6.1 Literature Review and Knowledge Gaps . . . 13

2 DEM-Based Drainage Network Delineation and Morphometric Analysis. **15**
2.1 Abstract . . . 15
2.2 Introduction . . . 15
2.3 Method . . . 16
2.3.1 Data Sources . . . 16
2.3.2 Analytical Approach . . . 16
2.4 Results and discussion . . . 19
2.5 Linear morphometric parameters . . . 19
Stream Order . . . 19
Stream Number . . . 20
Bifurcation Ratio . . . 20
Stream Length . . . 20
Mean Stream Length . . . 21
Stream Length Ratio . . . 21
2.5.1 Discussion of Linear Morphometric Parameters . . . 21
Spatial Variability in Linear Parameters . . . 21
Hydrological Implications . . . 22
2.6 Areal morphometric parameters . . . 24
Basin Area and Perimeter . . . 24
Form Factor and Elongation Ratio . . . 24

Circularity Ratio . . . 25
Drainage Density and Texture . . . 25
Drainage Intensity . . . 25
Stream Frequency . . . 25
Average Overland Flow Length . . . 25
Constant of Channel Maintenance . . . 26
Infiltration Number . . . 26
2.6.1 Discussion of Areal Morphometric Parameters . . . 26
2.7 Relief aspect . . . 27
Total Basin Relief . . . 28
Relief Ratio . . . 28
Ruggedness Number . . . 28
2.7.1 Discussion of Relief Morphometric Parameters . . . 29
2.8 Mapping Drainage density and Slope . . . 29
2.9 Conclusion . . . 31

3 Climatology **33**
3.1 Abstract . . . 33
3.2 Introduction . . . 33
3.3 Methodology . . . 34
3.3.1 Data Sources . . . 34
3.3.2 Data Processing . . . 34
3.3.3 Resolution Enhancement . . . 35
3.3.4 Geospatial Analysis . . . 35
3.3.5 Climate Classification . . . 35
3.4 Results . . . 36
3.4.1 Precipitation analyses . . . 36
3.4.2 Temperature analysis . . . 39
3.4.3 Climate determination . . . 40
The Bagnouls-Gaussen diagram . . . 40
De Martonne Aridity Index Analysis . . . 42
Emberger Classification Analysis . . . 42
3.5 Discussion . . . 43
3.6 Precipitation intensity Mapping . . . 43
3.7 Conclusion . . . 44

4 Remote Sensing across Landsat 8 OLI/TIRS **47**
4.1 Abstract . . . 47
4.2 Introduction . . . 47
4.3 Methodological Overview and Landsat 8 Data Processing . . . 48
4.4 Materials and Methods . . . 48
4.4.1 Selection and Preprocessing of Landsat Imagery . . . 48
4.4.2 Derivation of Spectral Indices and Training Data . . . 49
4.4.3 Extraction of Lineaments via PCA and Manual Digitization . . . 51
4.4.4 Seasonal LULC Mapping with April and July 2019 Imagery . . . 52
4.5 Results . . . 53
4.5.1 Land Use/Land Cover (LULC) Classification . . . 53
Accuracy of the Classification . . . 53
4.5.2 Lineament Extraction and Density Mapping . . . 55
4.5.3 Validation with Seasonal Imagery and DSA Data . . . 55
April 2019 Land-Cover Classification . . . 55

July 2019 Land-Cover Classification . . . 56
Combined Land-Use Classification . . . 58
4.5.4 Comparison with DSA Statistics . . . 59
4.6 Discussion . . . 60
4.6.1 LULC Mapping at the Onset of the Recharge Period . . . 60
4.6.2 Lineament Density and Hydrogeological Implications . . . 60
4.6.3 Seasonal Dynamics and Crop Phenology . . . 61
4.6.4 Validation with DSA Statistics . . . 61
4.6.5 Integrated Framework for Recharge Assessment . . . 61
4.7 Conclusion . . . 62

5 Hydrochemistry **63**
5.1 Abstract . . . 63
5.2 Introduction . . . 63
5.3 Methodology . . . 64
5.3.1 Piezometric Survey . . . 65
5.3.2 Total Dissolved Solids (TDS) Distribution . . . 65
5.3.3 Hydrochemical Analysis . . . 66
5.3.4 Data Integration and Statistical Analysis . . . 66
5.3.5 Implications . . . 66
5.4 Results and Discussion . . . 67
5.4.1 Piezometric Survey Results . . . 67
Figure Descriptions . . . 67
5.4.2 Piezometric Map Analysis . . . 69
5.4.3 Hydrochemical Analysis Results . . . 70
Calcium (Ca^{2+}) Distribution . . . 70
Magnesium (Mg^{2+}) Distribution . . . 71
Sodium (Na^{+}) Distribution . . . 71
Potassium (K^{+}) Distribution . . . 71
Bicarbonate (HCO_3^{-}) Distribution . . . 72
Sulfate (SO_4^{2-}) Distribution . . . 72
Chloride (Cl^{-}) Distribution . . . 72
5.4.4 Hydrogeochemical Discussion . . . 72
Calcium (Ca^{2+}) . . . 72
Magnesium (Mg^{2+}) . . . 73
Sodium (Na^{+}) . . . 73
Potassium (K^{+}) . . . 73
Bicarbonate (HCO_3^{-}) . . . 73
Sulfate (SO_4^{2-}) . . . 73
Chloride (Cl^{-}) . . . 74
Overall Implications . . . 74
5.5 Data Analysis Results . . . 74
5.5.1 Correlation Matrix Analysis . . . 74
5.5.2 Linear Regression Analysis . . . 75
5.6 Data Analysis Discussion . . . 78
5.7 Ionic Ratio Analysis . . . 79
5.7.1 Ionic Ratio Results . . . 80
5.7.2 Ionic Ratio Discussion . . . 86
5.8 Piper Diagram . . . 89
5.8.1 Anini, Boussellam, and Mkhalfa subcatchments . . . 90
5.8.2 Saber subcatchment . . . 91

5.8.3 Discussion of Piper Diagram 92
Anini, Boussellam and Mkhalfa Subcatchments 92
Saber Subcatchment 92
5.8.4 Schoeller-Berkaloff Diagram Results 93
5.8.5 Schoeller-Berkaloff Diagram Discussion 96
5.8.6 Wilcox and Riverside Diagrams 98
Riverside Diagram 98
Wilcox Diagram 98
Riverside Results 98
Wilcox Results 99
Discussion – Riverside 100
Discussion – Wilcox 101
5.8.7 Other Implications of Hydrochemical Sampling 101
5.9 Conclusion 101

6 Modeling Groundwater Recharge Potential Zones **103**
6.1 Abstract 103
6.2 Introduction 103
6.2.1 Review of Literature 104
6.3 Methodology 105
6.3.1 Rating Maps using AHP 106
6.3.2 Validation of the Model 107
6.4 Discussion 109
6.5 Conclusion 110
6.6 General Conclusion 110

Bibliography **113**

List of Figures

1.1 Geographical Situation of the State of Sétif 1
1.2 A Geographical Study of Water Basins in Sétif, Algeria 4
1.3 Detailed Local Geology Map of the Study Area 6

2.1 Workflow for DEM conditioning and stream extraction 18
2.2 Drainage density map of the northern Upper Boussellam catchment, computed on a 1 km^{-2} grid using a conditioned ASTER DEM. 30
2.3 Slope gradient map of the northern Upper Boussellam catchment, derived from ASTER GDEM v3 (30 m resolution). 31

3.1 Average monthly precipitation (in mm) for the period 1980–2018. Each subfigure shows the mean precipitation for the corresponding month. 37
3.2 Annual precipitation (in mm), computed as the sum of the monthly averages over the period 1980–2018. 38
3.3 Average monthly temperature (°C) for the period 1980–2018. Each subfigure represents the average temperature for the corresponding month. 39
3.4 Bagnouls–Gaussen ombrothermic diagrams 41
3.5 Upper Boussellam on Emberger climagram 42
3.6 Annual precipitation intensity in the Northern Upper Boussellam, interpolated via kriging from NASA-POWER data (1980–2021). Values range from <418.20 mm/year (42.54% area coverage) to a maximum of 703 mm/year (2.84% area coverage). 44

4.1 True color composite of the Northern Upper Boussellam from November 2022 Landsat 8 OLI/TIRS imagery. 49
4.2 Normalized Difference Water Index (NDWI) of the Northern Upper Boussellam from November 2022 Landsat 8 OLI/TIRS imagery, where water bodies are represented in white. 50
4.3 Normalized Difference Vegetation Index (NDVI) of the Northern Upper Boussellam from November 2022 Landsat 8 OLI/TIRS imagery, classified into five classes. 50
4.4 Principal Component Analysis outputs from Landsat 8 OLI imagery highlighting linear geological features. 51
4.5 LULC classification of the Northern Upper Boussellam from November 2022 Landsat 8 OLI/TIRS imagery. 53
4.6 False color composite (bands 7–5–3) with validation points used for accuracy assessment of the November 2022 classification. 54
4.7 Lineament density map of the Upper Boussellam basin derived from PCA-enhanced Landsat 8 imagery and geological data. 55
4.8 Landsat 8 OLI imagery of the Setifian High Hills, April 2019. 56
4.9 Supervised land-cover map for April 2019 from the pansharpened false-color composite. 56

4.10 Landsat 8 OLI imagery of the Setifian High Hills, July 2019. 57
4.11 Supervised land-cover map for July 2019, from maximum-likelihood classification of the pansharpened false-color composite. 57
4.12 Combined land-use classification map for April and July 2019. April-derived classes are shown with lighter tints, while July-derived classes (herbs and annual crops) are overlaid in more saturated hues to emphasize seasonal change. 59

5.1 Spatial distribution of Total Dissolved Solids (TDS) across the basin based on 44 sampled boreholes, showing low TDS in northern recharge zones and higher TDS in southern downgradient sectors. 66
5.2 Google Hybrid map displaying the 120 sampling points used for constructing the piezometric map along with the 39 sampling points used for hydrochemical analysis. 67
5.3 Geological map showing the 39 sampling points used for hydrochemical analysis. 68
5.4 Google Hybrid map illustrating the piezometric contours. 68
5.5 Geological map displaying piezometric contours. 69
5.6 Spatial distribution of major ions (mg/L) interpolated via IDW in QGIS: (a) Ca^{2+}, (b) Mg^{2+}, (c) Na^{+}, (d) K^{+}, (e) HCO_3^{-}, (f) SO_4^{2-}, (g) Cl^{-}. 70
5.7 Linear regression plots of electrical conductivity against major cations and anions. Panels (a–c) show cations (Ca^{2+}, Mg^{2+}, Na^{+}) and (d–e) show anions (SO_4^{2-}, Cl^{-}). 76
5.8 Inter-ionic linear regression plots among major solutes. Panels (a–h)quantify the strength of each pairwise relationship, showing best-fit lines and R^2 values. 77
5.9 Ca^{2+}/Mg^{2+} ratio: (a) sample-by-sample binary diagram; (b) IDW-interpolated spatial distribution. 80
5.10 Ca^{2+}/HCO_3^{-} ratio: (a) sample-by-sample binary diagram; (b) IDW-interpolated spatial distribution. 81
5.11 Ca^{2+}/SO_4^{2-} ratio: (a) sample-by-sample binary diagram; (b) IDW-interpolated spatial distribution. 81
5.12 Mg^{2+}/HCO_3^{-} ratio: (a) sample-by-sample binary diagram; (b) IDW-interpolated spatial distribution. 82
5.13 Mg^{2+}/SO_4^{2-} ratio: (a) sample-by-sample binary diagram; (b) IDW-interpolated spatial distribution. 83
5.14 Na^{+}/Cl^{-} ratio: (a) sample-by-sample binary diagram; (b) IDW-interpolated spatial distribution. 83
5.15 HCO_3^{-}/SO_4^{2-} ratio: (a) sample-by-sample binary diagram; (b) IDW-interpolated spatial distribution. 84
5.16 Na^{+}/HCO_3^{-} ratio: (a) sample-by-sample binary diagram; (b) IDW-interpolated spatial distribution. 85
5.17 $(Ca^{2+}+Mg^{2+})/HCO_3^{-}$ ratio: (a) sample-by-sample binary diagram; (b) IDW-interpolated spatial distribution. 85
5.18 $(Ca^{2+}+Mg^{2+})/SO_4^{2-}$ ratio: (a) sample-by-sample binary diagram; (b) IDW-interpolated spatial distribution. 86
5.19 Piper trilinear diagram summarizing the major-ion chemistry of groundwater samples from the Anini, Boussellam and M'khalfa subcatchments. 90
5.20 iper trilinear diagram summarizing the major-ion chemistry of groundwater samples from Ouled Saber subcatchment. 91

5.21 Schoeller–Berkaloff diagrams of major-ion concentration profiles for the northern sector. 94
5.22 Schoeller–Berkaloff diagrams of major-ion concentration profiles for the middle sector. 95
5.23 Schoeller–Berkaloff diagram of major-ion concentration profiles for the lower sector. 96
5.24 Riverside hydrochemical polygon diagrams. 99
5.25 Wilcox diagrams of groundwater quality for (A) The Eastern subcatchments and (B) Ouled Saber subcatchment. 100

6.1 Thematic layers rescaled on a 1–10 scale according to their contribution to groundwater recharge: (a) drainage density; (b) slope; (c) LULC; (d) lithology; (e) lineament density; (f) precipitation intensity. . 106
6.2 Groundwater-Recharge Potential Zone classes map (GWRPZ), generated via the AHP-weighted overlay (Eq. 6.2). Source: Khemmal et al. (2025) 107
6.3 Spatial distribution of TDS sampling points overlaid on the groundwater recharge potential zones map. Source: (Khemmal et al., 2025) . . 108
6.4 Receiver Operating Characteristic (ROC) curve for the groundwater recharge potential zones model, illustrating classification performance. Source: Khemmal et al. (2025) 108
6.5 Modeling Groundwater Recharge Potential Zone across Remote Sensing, GIS, and Hydrochemistry: integrated framework with AHP and validation. 111

List of Tables

2.1 Linear Characteristics of Drainage Basins. 19
2.2 Areal Morphometric Characteristics of Drainage Basins. 24
2.3 Relief Morphometric Characteristics of Drainage Basins. 27

3.1 Precipitation analysis in the study area. Drainage basin precipitation (mm) – monthly averages (Jan–Dec) and annual totals. 38
3.2 Mean temperature analysis in the study area. Drainage basin temperature (°C)—monthly averages (Jan–Dec) and annual averages. 40
3.3 Emberger Classification Results 43

4.1 Confusion matrix for November classification 54
4.2 Surface area for each class in the combined land use map. 59
4.3 Comparison between results obtained from Landsat 8 OLI/TIRS and DSA statistics. 60

5.1 Correlation Matrix of Ion Concentrations and Conductivity 74

To my beloved family, my esteemed supervisor, and my dear friends and colleagues, each of whom has left an indelible mark on this work.

And We send down water from the sky, by which We give life to the earth after its death; and thus you will be brought forth." (Qur'an, Surah Ar-Rum (30:19))

And you see the earth barren, but when We send down upon it water, it stirs and swells and brings forth every kind of beautiful growth. That is because Allah is the Truth, and it is He who gives life to the dead, and He is over all things competent.(Qur'an, Surah Al-Hajj (22:5))

Chapter 1

Overview of the Study area

1.1 Geographical context

Water resources are a critical component in the sustainable development of any region, including Sétif. Located in the eastern part of Algeria within the High Plateaus, as shown in Figure 1.1, Sétif is a significant hub in the country's transportation network. Its strategic location and significant population increase the demand for water resources.

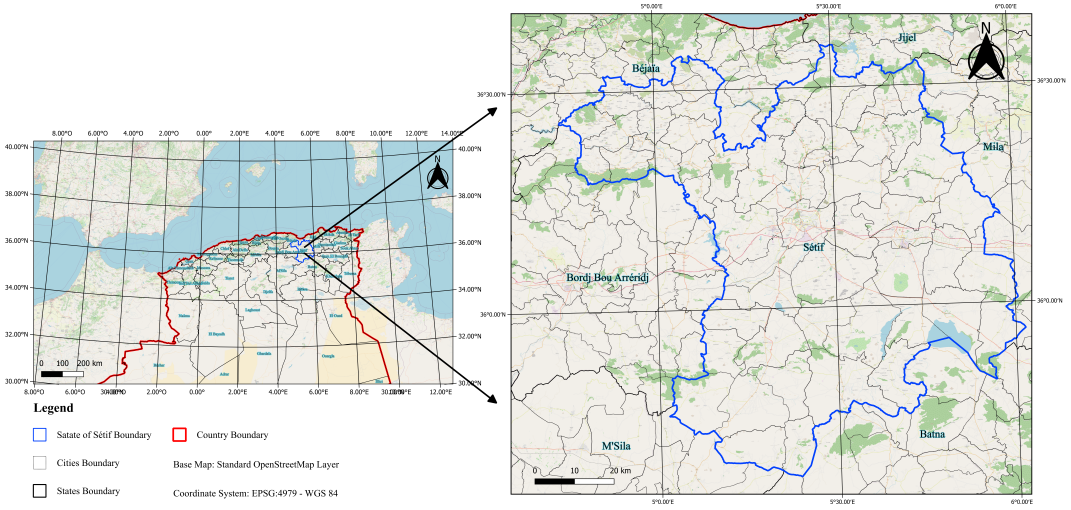


FIGURE 1.1: Geographical Situation of the State of Sétif, illustrating its location and geographical context within Algeria.

The region's robust transportation network facilitates the movement of goods, across the country. Sétif's role as a transit point for convoys of goods coming from the South and heading towards the ports of Bejaia and Jijel. However, the harsh continental climate and geographical positioning on the highlands could pose challenges to water availability.

Sustainable management of water resources in Sétif is therefore critical. This involves understanding the region's water needs, assessing the availability of water resources, and implementing strategies to ensure their sustainable use. Factors such as rainfall intensity, groundwater recharge potential, and the impact of climate change need to be considered. Efficient logistics can ensure that water and other essential goods reach the people who need them most.

Sétif's strategic location, significant population, and robust transportation network underscore its importance in Algeria's socio-economic landscape, the sustainable management of water resources is crucial to ensure the region's continued growth and development. The focus should be on ensuring that water - a vital resource - is available to all in a sustainable manner, aligning with global efforts towards achieving water security and sustainable development goals.

1.2 Vegetation Cover

The Sétif region, located in the High Plateaus of eastern Algeria, exhibits a diverse and evolving vegetal cover shaped by both natural conditions and human activity. According to the Directorate of Agricultural Services, the total agricultural surface (T.A.S) spans approximately 557,070 hectares, of which 364,913.25 hectares represent the Useful Agricultural Surface (U.A.S). This includes 37,081.75 hectares of irrigated land and 53,850 hectares of pasture. Land zoning across the region is heterogeneous: 31.33% corresponds to northern mountainous terrain, 12.10% to foothills, 20.03% to plains, 28.56% to agro-pastoral zones, and 7.98% to southern mountains. In terms of legal status, the land is distributed as 63% Melk (including 18% unregistered), 22% communal arch, and 15% state-owned private lands.

The region's 2017/2018 cropping plan reveals a strong emphasis on cereal cultivation, which accounts for nearly 52% of the U.A.S—and nearly 79% when fallow is included. Cropped areas include 197,006.75 hectares of cereals, 25,173 hectares of fodder (10,173 of which are green fodder), 21,986 hectares of vegetable crops (including 1,754 hectares of potatoes), 1,073 hectares of industrial crops, 36,269 hectares of arboriculture (dominated by 22,914 hectares of olive trees), and 25.58 hectares of vineyards.

Sétif holds a notable position at the national level in agricultural production: it ranks first in cereal output (3,196,620 quintals), second in tobacco (21,434 quintals), and eighth in fodder crops (1,792,621 quintals). It is also among the top contributors to the national supply of vegetables, onions, potatoes, fruits, and olives. While the agricultural potential remains high, the U.A.S per inhabitant stands at 0.22 hectares—slightly below the national average—highlighting the need for more efficient land use and fallow reduction.

Durum wheat cultivation forms the backbone of local agro-economics, playing a crucial role in food security and rural livelihoods (Mezrag, 2018). However, these practices exert considerable pressure on groundwater resources, underscoring the importance of integrated water–land management strategies. Sustainable water use, especially in support of agriculture, is thus central to ensuring long-term viability in the region.

Ecologically, the northern part of Sétif—particularly Djebel Mégriss—hosts diverse vegetation types and habitats. According to Boulaacheb (2010), this area encompasses a mosaic of terrestrial and aquatic environments, including plateau grasslands, low matorrals, temporary wetlands, springs, marshes, and flood-prone meadows. It supports a remarkably rich flora: 500 recorded plant species, 22 subspecies,

276 genera, and 72 families. Mediterranean elements constitute 40% of this flora, followed by Nordic (24%), transitional (19%), endemic (10%), cosmopolitan (5%), and tropical (2%) species.

Nevertheless, the region faces growing threats from anthropogenic pressures such as overgrazing, habitat fragmentation, water abstraction, and pollution (Boulaacheb, 2010). These changes highlight the urgent need for conservation and sustainable land-use planning to preserve biodiversity and support ecosystem resilience.

In conclusion, the vegetal cover of Sétif, especially in the northern mountainous zones, reflects a critical intersection between biodiversity, agriculture, and hydrological sustainability. Agricultural practices and natural vegetation dynamics play pivotal roles in shaping regional water balance. As such, any assessment of groundwater recharge potential must account for the spatial and seasonal patterns of land use and vegetation, as addressed in this study.

1.3 Hydrological Overview

The administrative boundaries of the Wilaya of Sétif encompass four principal hydrological basins. As illustrated in Figure 1.2, the northern part integrates segments of the Coastal Constantinois, Soummam, and Rhummel basins, all of which direct surface waters toward the Mediterranean Sea. In contrast, the southern domain—comprising areas of Hodna and portions of the Constantinois—exhibits endorheic hydrographic behavior, where surface water accumulates in closed depressions such as the Chotts. The central region is hydrologically divided: its western flank is primarily associated with the Soummam basin, while the eastern sector drains into the Rhummel. Notably, the Soummam basin occupies the largest hydrological footprint within the Wilaya.

The Upper Boussellam catchment, located in the north of the Sétif province, constitutes a pivotal component of the region's water network. It comprises nine subcatchments, all contributing to the main course of the Oued Boussellam. A central element of this system is the Ain Zada Dam, positioned approximately 23 km west of Sétif and 37 km northeast of Bordj Bou Arréridj. According to the National Agency of Dams and Transfers (ANBT), this infrastructure plays a dual role: it supports irrigation across water-scarce agro-zones of Sétif and Bordj provinces, and also supplies potable water to several urban centers, including Sétif, Eulma, Bougaa, and Bordj Bou Arréridj.

This thesis focuses on the northern portion of the Upper Boussellam basin, which includes four sub-catchments and the Boussellam spring that originates from Djebel Mégriss. This mountainous area constitutes the primary source of surface water feeding the Oued Boussellam, which in turn contributes significantly to the Soummam River system. The region lies between latitudes 36.00° and 36.35°N and longitudes 5.12° and 5.60°E, and is bordered by the Tellian Atlas to the north and the Saharan Atlas chain to the south, with fertile plains stretching between.

Prominent geomorphological landmarks include the Anini, Mégress, Mnaguer, and Merouane mountains to the north, and the Youssef and Zdim ranges and Sebkhat Melloul to the south. The four targeted sub-catchments span a total of 1,200 km²—approximately 62% of the entire Upper Boussellam basin—and intersect several municipalities: Sétif, Ouricia, Ain Abassa, Mahouane, Mezloug, Ain Arnat, Guidjal, Ras El Ma, and Ouled Saber.

This northern sector is particularly significant due to elevated precipitation patterns, especially in the upstream mountainous zones, and because it encompasses

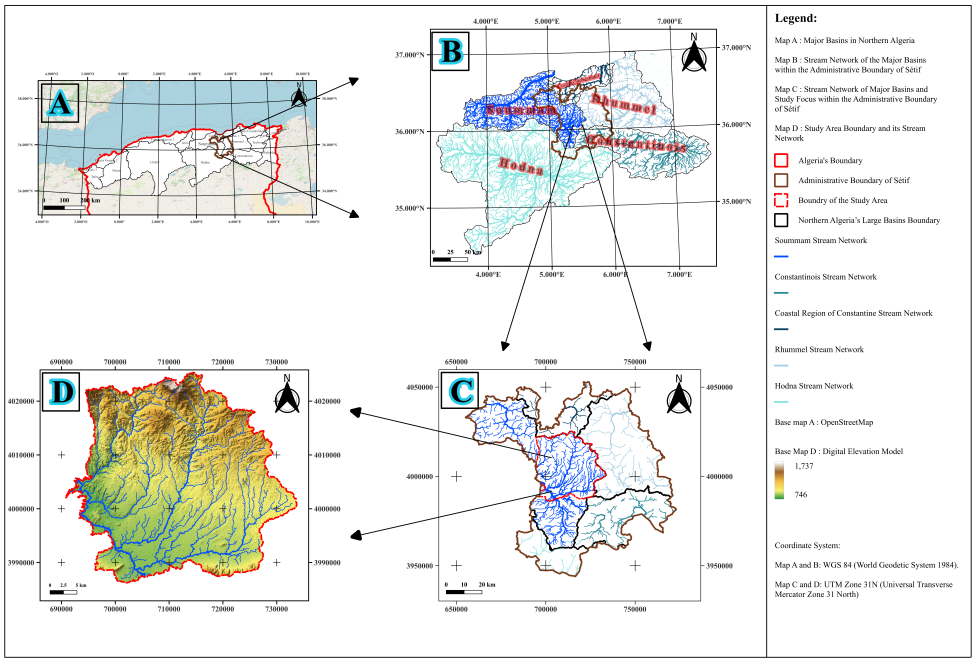


FIGURE 1.2: Hydrological distribution of the main surface water basins in Sétif Province.

the principal hydrographic artery feeding the Ain Zada Dam (**Boulgueraguer2022**). Its physiographic and geological complexity makes it a compelling site for groundwater recharge assessment and water resource planning.

1.4 Climate

Algeria's climate ranges from Mediterranean along the coast to arid in the Sahara, with five bioclimatic zones:

- **Humid:** Coastal Tellian slopes (eastern coast).
- **Sub-humid:** Fringe areas of the Tellian Atlas.
- **Semi-arid:** Interior basins of the Tellian Atlas and the High Plateaus.
- **Sub-arid:** Southern foothills of the Saharan Atlas.
- **Arid:** Central and southern Sahara.

The Tell Atlas acts as a climatic barrier: moisture-laden Mediterranean air rises, cools, and precipitates on the northern slopes, while leeward areas lie in rain shadow.

Regional climate of Sétif. The Sétif plateau falls within the semi-arid to sub-humid transition. Mean annual temperature is ∼15 °C (winter minima <5 °C; summer maxima up to 35 °C). Precipitation is strongly seasonal: 80% of the 500–700 mm yr^{-1} in the northern plain falls between October and April, with peaks in December–January. The Babor massif to the north receives >1 000 mm yr^{-1}, while summer

months (June–August) contribute <10% of annual rainfall, creating pronounced hydrological deficits.

Impacts on water resources. Recurrent summer droughts and high potential evapotranspiration reduce surface flows and depress groundwater levels, intensifying competition between agricultural, domestic, and ecological uses. Winter snowpack in the highlands (December–January) provides a delayed runoff pulse that recharges alluvial aquifers.

Data and methods. To quantify spatial and temporal variability, we analyzed long-term rainfall and temperature records using NASA POWER datasets and processed them in QGIS. Daily and monthly gridded data were used to:

1. Map seasonal rainfall and temperature distributions across the four sub-catchments.

Detailed methodology and results are presented in Chapter 3.

It's important to note that managing water resources in the face of climate variability and recurrent droughts is a significant challenge. It requires effective strategies for water conservation, efficient use, and sustainable management practices.

In order to understand the impact of climate on water availability and the ecosystem within the northern part of the upper Boussellam catchment and its four sub-catchments we analyzes long-term spatial and temporal patterns in rainfall and temperature data Using NASA LARC POWER data and QGIS More detail are in Chapter 3.

The semi-arid climate of Sétif can be better understood through our analysis. This can provide a detailed picture of how these climatic factors interact and influence each other. Moreover, understanding these patterns can help predict future climatic trends and potential impacts on water availability in the northern part of the upper Boussellam catchment and its four sub-catchments. This could be crucial for developing effective water management strategies and ensuring the sustainability of the local ecosystem. Our study is leveraging advanced data analysis and geographic information system tools to unravel the complexities of Sétif's climate.

In summary, Sétif's semi-arid climate—with its marked seasonality, orographic rainfall in the north, and extended dry summers—exerts a primary control on surface water availability and groundwater recharge potential in the Upper Boussellam catchment.

1.5 Geology

In the geological study of the Sétif region, a multi-scale approach was adopted to provide a comprehensive understanding of the area. The focus of the study is not the entire state, but specifically the northern part of the upper Boussellam, which contains four subcatchments and the main stream that drains these subcatchments.

Initially, The region's structural framework was delineated using an interpretative geological map (ANRH, 2008; scale 1:200,000). The original map was obtained from ANRH and provided to the author for academic use. The map was digitally/geometrically adjusted and annotated by the author to incorporate field observations.

Detailed Map: To delve into more detail and provide a comprehensive understanding of the study area, and for a more granular analysis, detailed maps scaled at 1:50,000 were used. As illustrated in Figure 1.3, these maps offered an in-depth view of the local geology, incorporating data from maps such as Setif 93 and Mezloug 117,

and supplemented by additional coverage from Boussellam 92, Ain Taghrout 116, Eulma 94, Bir El Arch 118, and Kherrata 70. This comprehensive approach ensured thorough analysis of the study area. these sheets (Setif 93, Mezloug 117, Boussellam 92, Ain Taghrout 116, Eulma 94, Bir El Arch 118, Kherrata 70) are based on the work of JM (1980) and were supplemented and updated by the author to reflect field observations. The maps were georeferenced and digitally edited by the author.

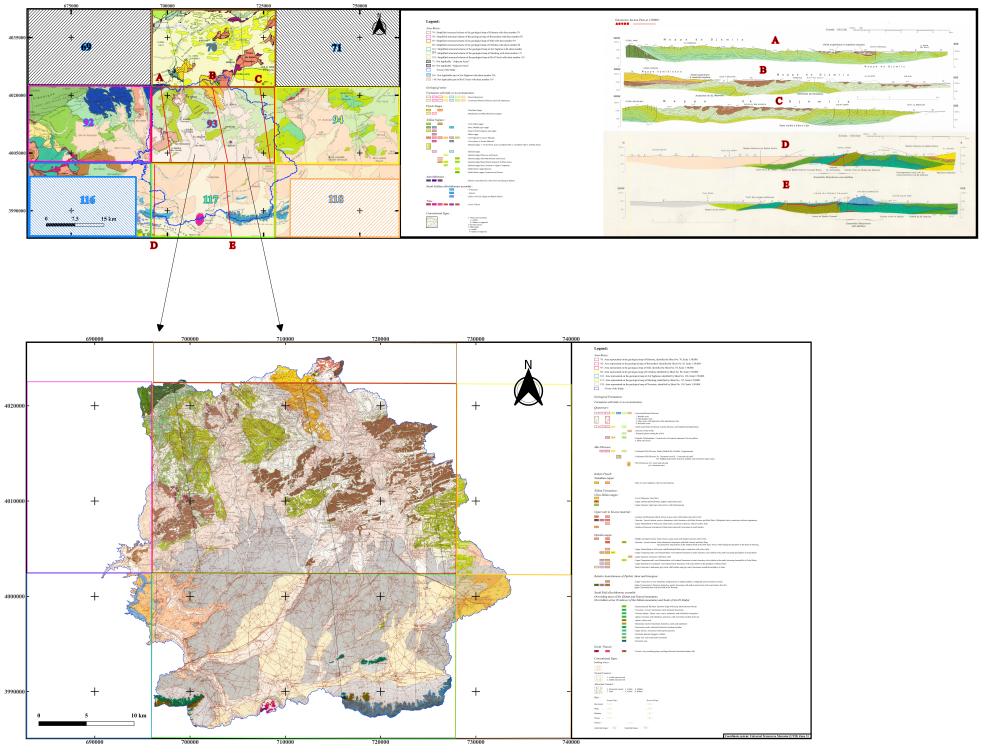


FIGURE 1.3: Detailed Local Geology Map of the Study Area: Detailed maps at a 1:50,000 scale —including Setif 93 and Mezloug 117, with supplementary coverage from Boussellam 92, Ain Taghrout 116, Eulma 94, Bir El Arch 118, and Kherrata 70.

This combination of maps, ranging from a broad overview to detailed views, facilitated a comprehensive understanding of the complex interplay of various geographical and environmental factors within the study area. It provided insights into the intricate relationships between different environmental elements and their impact on the region's geology. This multi-scale approach is crucial for geological studies, helping to reveal the detailed geological structure and dynamics of the Sétif region.

1.5.1 Local Geological Context

The study region, situated in Northern Algeria, is marked by its geological diversity. It comprises a variety of terrains that are integral to the region's distinct structural domains. The geological units identified within our study area include according to JM (1980)

- 1. Quaternary and Neogene Formations: These stratigraphic units, which have undergone minimal tectonic deformation, represent the most recent epochs in the geologic time scale. They encompass sediments deposited during the Quaternary (the last 2.6 million years) and the Neogene (spanning from 23 to 2.6 million years ago).
- 2. Continental Mio-Pliocene: The Continental Mio-Pliocene formation is composed of an accumulation of sands, reddish silts, and conglomerates. Its thickness can exceed 500m to the west of Mezloug. This entire formation rests in angular discordance on the Upper Cretaceous.
- 3. Flysch Domain: The Flysch domain is characterized by a sequence of sedimentary rocks that are typically deposited in deep marine facies in the foreland basin of a developing orogen. Flysch is often indicative of tectonic activity.
- 4. External Domain Represented by the Tellian Nappes: The Tellian nappes, specific to certain regions of the Maghreb, including Algeria, are thrust sheets formed by compressional tectonic forces. These forces cause sedimentary rocks to fold and fault, forming distinct structural units.
- 5. Autochthonous: This term refers to geological materials or units found in their original location. The relative autochthonous of Djebels Anini and Guergour, a natural region of Algeria located between the Tell Atlas to the north and the Saharan Atlas to the south, represents an autochthonous unit. It has remained relatively stable and unaffected by the tectonic activity that resulted in the displacement of other units.
- 6. The South Setifian Allochthonous: The South Setifian Allochthonous is a local geological unit that has been displaced from its original position due to tectonic activity. In geology, an allochthonous unit is one that is found in a location other than where it formed.
- 7. Exotic or Extrusive Trias: This corresponds to the oldest terrains known to outcrop in the region.

In the following sections, we delve into the geological formations present in our study area based on the work of JM (1980). These formations span various epochs and are indicative of the region's rich geological history and diverse structural domains. We begin by exploring the Quaternary and Neogene Formations, which have undergone minimal tectonic deformation and represent the most recent epochs on the geologic time scale. We then move on to the Flysch Domain, characterized by a sequence of sedimentary rocks indicative of tectonic activity. The discussion further extends to the External Domain represented by the Tellian Nappes, the Autochthonous, the Parautochthonous represented by the South Setifian Allochthonous, and the Exotic or Extrusive Trias. Each of these geological units contributes uniquely to the overall geological context of the region.

Quaternary and Neogene Formations with Minimal Tectonization

The Quaternary and Neogene formations are characterized by minimal tectonization. according to JM (1980) They include the following units:

• **Recent and Current Alluvium:** This formation is characterized by sediment deposited by flowing water, such as in a river bed, flood plain, or delta.

• **Boulder:** This formation surrounds high mountains such as Anini and Megriss. It contains a collection of broken rock fragments at the base of crags, mountain cliffs, or valley shoulders, Marl gangue scree, a recess in the upper edge of the moving mass during a landslide. The material from the detachment niche is transported downstream abruptly and forms a deposit whose morphology is often chaotic and Numidian scree.

• **The Quaternary:** This includes Arable land, Slope formations, Ancient alluvium, and Undetermined Quaternary.

• Quaternary (Qt): This formation is characterized by Polygenic glazes coating the reliefs. This formation is located around the South Sétif allochthonous assembly.

• Villafranchian (Qc): This formation is characterized by an alternation of clays and marls with past gravels associated with lacustrine limestones. The Villafranchian stage is a regional stratigraphic division of the early Pleistocene epoch.

Continental Mio-Pliocene

This stage is characterized by a complex assembly of continental formations, occupying vast spaces in the region. According to JM (1980) It is formed by loams and red conglomerates, pudding stones, gypseous clays, clusters of pebbles, and sparkling clays. There are also conglomerates with large gravels topped by reddish-gray clays at micro-conglomerate levels with a lignite level of about 40m thickness. Above this series, there are clays and marls, sometimes gypsiferous, alternating upwards with levels of lacustrine limestone varying in thickness between 150-200m. At the summit, the series becomes variable with lenticular intercalations of coarse pudding stones, clays, friable lignite lenses with gypseous sandstone beds to small limestone benches. The thickness varies between 150 to 200m. The series ends with varied fluvial-lacustrine deposits: Pudding stones, stratified limestones, lenses of gravel, and black clay. The thickness is approximately 150m. In addition, the Continental Mio-Pliocene formation is composed of an accumulation of sands, reddish silts, and conglomerates. Its thickness can exceed 500m to the west of Mezloug. This entire formation rests in angular discordance on the Upper Cretaceous

The Domain of Flyschs

The Domain of Flyschs is a result of compressional tectonic forces that cause sedimentary rocks to fold and fault, forming distinct structural units. According to JM (1980) It is associated with the following nappes:

• **Numidian Nappe (Oligocene):** Located in the northern half of the Sétif map (93) and the south part of Kherrata map (70) at Dj. Megriss and Chouf Karoun, this nappe comprises greenish clay at the base and an alternation of coarse sandstone and clay in its upper part. It contains bars of coarse sandstone with clay intercalations.

• **Nappe of the Mauritanian and Massylian Flyschs:** The Mauritanian Flysch, situated at the extreme west of the Boussellam map (92) at Ras El Reil, consists of Senonian and Eocene conglomerates and Oligocene mica sandstones. The Massylian Flysch, which surrounds the Mauritanian Flysch at Ras El Reil and also appears in Kantara, is composed of Albian-Aptian schist-quartzite, Cenomanian-Turonian phtanites, and Senonian marly, microbreccia, and conglomerate formations.

The Tellian Nappes

The Tellian Nappes form a significant component of the geological architecture in the Tellian domain. These nappes encompass a multitude of stratigraphic units,

each contributing to the complex geological composition of the region. According to JM (1980): • **Ultra-Tellian Nappe:** Located on the west side of Djebel Megriss, this nappe comprises several geological formations: - Lower Oligocene: Characterized by Grey Marl. - Upper Lutetian and Priabonian: Composed of slightly sandy black marls. - Upper Senonian: Consists of light marls and micrites with Globotruncana.

• **Barbacha Type Nappe:** This nappe, which only outcrops in the north of Ain Roua (it's the Baborian autochthonous of J. Glaçon), is characterized by a metamorphic Lower Cretaceous (dark, hard, chlorite metamorphic schists) and a Lias with compact limestones and flinty limestones alternating with crushed marl beds.

• **Béni-Abdallah Type Nappe:** This nappe appears in Ain Roua in Djebel Chouf Karoun and in Ouled Sidi Amor, in the klippe which appears in Boussellam 92 and Ain Taghrout 116. It is composed of the following:

- Upper Campanian: Marly of Chouf Karoun.

- Senonian: Grey or black scaly marls with intercalations of marly limestone with a jade-green patina.

• **Draa el Arba Type Nappe:** This nappe, primarily located on the ridges extending from Djebel Takoucht to the north of Djebel Babor (as per the Kherrata map 70), also appears in Boussellam in the southeast part of Bordj Zemoura. It is composed of:

- Eocene: Globigerina facies around Dra Chloha.

- Campanian: Grey or black marls with lenticular banks of black or grey micrites and abundant yellow balls.

• **Bibanic Nappe:** This nappe, constituted by a long monocline strip of Cretaceous terrains with a southern dip developed between Berrouaghia in the west and the Djebel Guergour massif, possesses:

- Upper Campanian and Lower Maastrichtian: Grey or black scaly marls with abundant yellow balls.

- Upper Coniacian and Santonian: Alternation of marls and micrites with Rosalines.

- Turonian-Coniacian: Marls and micrites with a flint marker at the base.

- Upper Albian to Cenomanian: Alternation of black marly limestone and grey marls forming a cornice.

- Lower Cretaceous: Grey pelites with marly limestone intercalation at the base, becoming sandier at the top and more marly under the cornice.

• **Upper Unit with Eocene Material:** This unit is identifiable in our study area in three distinct outcrop groups: the southwestern slope of Djebel Mégriss, the Klippe of Ain Abessa, and that of Ain Messaoud. This unit is distinguished by:

- Middle and Upper Eocene Stage: This stage is marked by a Marly Series, abundant in yellow nodules and dolomitic benches. The series extends to a considerable thickness of 400m.

- Lower Ypresian Lutetian Stage: This stage is characterized by Marly Limestones, indicative of a shallow marine environment during the early Eocene epoch.

- Upper Maastrichtian to Paleocene Stage: This stage is defined by a series of black marls, occasionally shaly, interspersed with rare yellow nodules. The series, alternating with marly limestones, reaches a thickness of at least 180m.

• **Lower Unit with Eocene Material:** This geological formation, spanning from the Ypresian stage to the lower part of the Lutetian stage, is observed in various locations. It is characterized by white bituminous limestones with black fractures and black flints. Rare glauconitic intercalations are observed in the southern third of the Setif sheet. Facies with Globigerina and debris are present in the sheet of Mezloug.

• **The Djemila Nappe:** The Djemila Nappe, a significant geological feature in the region, constitutes the majority of the landscape to the north of Sétif and El Eulma and extends eastward to the vicinity of Sidi Mérouane. It exhibits considerable variations both from north to south and from east to west. It is the only Tellian unit represented by a complete series ranging from the Lias to the end of the Eocene. For a simple reason of outcrop continuity, we can gather under the name of "Djemila Nappe" the following units:

• Bou Sellam Series: This series around Djebel Guergour, Anini, and Hellel represents a specific stratigraphic sequence in the region.

• Sétifian Domes: The vast sector of the "Sétifian domes" around Djebel Medjounés, the Djemila mountains, and Ouled Sabor represents a unique geological structure in the region. The Djemila Nappe is characterized by the following formations:

• Middle and Upper Eocene: Black, brown or gray marls with benches and rare yellow balls.

• Ypresian - Lower Lutetian: The Lower Ypresian-Lutetian stage is characterized by White bituminous limestones with black fracture and black flints, rare glauconitic intercalations in the southern third of the Setif sheet/ Facies with Globigerina and debris in the region of Mezloug. It is composed, from top to bottom, of:

- Blackish marly limestones, sandy in nature, with a thickness of 20m.

- Massive gray or white limestones rich in flint, with a thickness of 80m.

- An alternation of marls, limestones, and marly limestones, with a thickness of 100m.

• Upper Maastrichtian to Paleocene: Undifferentiated black marls, sometimes with yellow nodules. This assembly outcrops over small extents, represented by black to gray marls with rare yellow limestone nodules. At the top of the series, decimetric limestones appear with oysters and Inoceramus. This series has a very variable thickness of 100 to 150 m due to consecutive tectonic phenomena. The microfauna encountered include Globotruncana.

• Upper Campanian and Lower Maastrichtian: This stage is characterized by well-structured limestones arranged in metric benches, rich in organic debris, particularly towards the north. These limestone formations transition into lumachellic structures at Ouled Sabor. The assembly is primarily composed of carbonate, with an abundance of Lamellibranchs in these lumachellous levels. Additionally, Gastropods and Echinoderms are commonly found within these formations.

• Campanian to Lower Maastrichtian: This stage is marked by the presence of dark marls, notable for their abundance of yellow nodules. The exposure of this series is limited, not exceeding an area of 1.5 Km^2. The marls are characterized by very small yellow nodules, and towards their top, there are occasional layers of marly limestone. The series has a considerable thickness, reaching up to 150m. It is noteworthy for the presence of Globotruncana formicata from the Upper Campanian and Globotruncana at the pinnacle of the Maastrichtian series.

• Upper Santonian to Campanian: This geological stage is characterized by a well-organized sequence of marly limestones, which are particularly rich in oyster debris. This is especially noticeable around the periphery of Djebel Anini. The sequence consists of alternating layers of gray or black-gray marl and lumachellic limestone. These limestone layers are arranged in metric benches and exhibit an ocher or whitish color. They are rich in oyster fossils, indicating a marine environment. The overall thickness of this geological assembly is approximately 100 meters

• Basal Coniacian to Santonian: Gray marls with Rosaline and gray marly limestones. It is also noticeable around the periphery of Djebel Anini.

• **The Djebel Sattor Nappe:** This nappe, which appears in the southwest of Setif at the boundary of the Mezloug map 117 and Ain Taghrout 116, is composed of several distinct geological formations:

- Marine Transgressive Miocene: This formation refers to a marine transgression that occurred during the Miocene epoch.

- Upper Marly Lutetian: This layer is characterized by marly deposits from the upper part of the Lutetian stage.

- Ypresian-Lower Lutetian with Debris Forming a Limestone Bar: This layer spans from the Ypresian stage to the lower part of the Lutetian stage. It is characterized by debris that forms a limestone bar.

- Upper Lumachellic Senonian: This layer, from the upper part of the Senonian stage, is characterized by lumachellic deposits.

Relative Autochthonous of Djebels Anini and Guergour; and the South Setifian Allochthonous Assembly

This formation appears in Djebels Anini and Guergour. It spans from Upper Coniacian to Lower Santonian and Upper Cenomanian to Turonian. It is characterized by conglomeratic or nodular pebbles, eroding the neritic Turonian of Anini, dolomites, and sparitic limestones with rudists and micrites with cisalveolines from the Upper Cenomanian then with miliolids in the Turonian.

South Setifian Allochthonous Assembly In our study area, this assembly comprises two sub-units according to JM (1980). From North to South, they are:

• **Overridden series (S indices in the map) of the Zdimm mountains and Scale of Ain El Ahdjar:** This domain possesses a carbonate series ranging from the Lias to the Cenomanian. This ensemble affects the disposition of a sheared anticline at Djebel Youssef. The basal contact of the Jurassic dolomites of Djebel Youssef is slightly inclined towards the North. There is an absence of outcrops from the Senonian and Eocene.

• **Overriding mass of the Zdimm and Youssef mountains:** This ensemble is observed with a mass of Jurassic dolomite that tectonically rests on a marly limestone series of the Lower Cretaceous. This ensemble shows a series where the marine Miocene fossilizes the structures sheared by the basal contact. It is also noted that this series has a thin Senonian and Eocene cover; the abundance of biosparites (presence of pebbles attesting to a turbulent environment) indicates a shallow environment. The South Setifian Allochthonous Assembly is characterized by the following formations:

- Cenomanian and Turonian: Limestone ledge with marly intercalation at the top.

- Vraconian - Lower Cenomanian: Marls and marly limestones.

- Terminal Aptian - Albian: Clays, marls, sandstones, and milobésiées biosparites.

- Aptian: Limestone with orbitolines and layers with ovalveolina reicheli at the top.

- Aptian: Yellow marl.

- Barremian: Massive limestones, dolomites, marls, and sandstones.

- Neocomian: Marls with small bioclastic limestone benches.

- Upper Jurassic: Limestone with Clypeina jurassica.

- Dolomitic Jurassic (Dogger to Malm).

- Upper Lias: Marls and marly limestones.

- Dolomitic Lias.

Exotic or Extrusive Trias

This unit is essentially represented by evaporites. Unlike other formations, it never outcrops in a normal stratigraphic position, under the Lias strata. Instead, it presents itself in diapiric points and injected blades along tectonic accidents, without any stratification. According JM (1980), the Triassic masses mark the abnormal tangential contacts except for the southern autochthonous sectors where the Trias occupies a clearly extrusive anticlinal position.

Sebkha Soils:

Sebkha soils, also known as Sabkha, are a distinctive type of soil found in flat, low-lying areas, typically in arid or semi-arid climates. These soils are often located in coastal regions, forming a transitional zone between terrestrial and intertidal areas. They are characterized by their saline nature, resulting from the accumulation of evaporite-saline minerals due to the prevailing climatic conditions. In specific regions such as Sebkhat Bazer, Chott El Frain, Sebkhat El Hamiet, and Chott El Beida, these Sebkha soils are represented by saline silts. These silts undergo periodic inundation, especially during the rainy season, and are covered by saline crusts during the dry season. Sebkha soils are often viewed as unconsolidated, heterogeneous, and cemented, immersed in highly concentrated subsurface brines. They are generally composed of quartz sand and silt with small proportions of mud and clay and have a relatively hard crusty surface. The main cementing minerals are aragonite, gypsum, anhydrite, and halite, and these minerals vary from one location to another. These soils are known for their unique behavior. Upon wetting, they are susceptible to collapse due to the dissolution of cementing materials and their corrosive effects and heaves due to the salt crystallization/recrystallization process.

In summary, the northern Upper Boussellam catchment's exceptional geological heterogeneity—ranging from Triassic clay-gypsum sequences through Jurassic and Cretaceous carbonates to Mio-Pliocene lacustrine deposits and Quaternary alluvia—renders it an ideal natural laboratory for groundwater recharge studies. The juxtaposition of high-permeability karstified limestones and intergranular aquifers with low-permeability clays and sandstones creates distinct hydrogeological compartments whose infiltration dynamics can be contrasted and quantified. For these reasons, the study area was specifically chosen to integrate geological complexity into a robust assessment of recharge potential zones, ensuring that model outputs reflect the full spectrum of subsurface conditions encountered in semi-arid high-plateau environments (**Vila1980**).

1.6 Research Rationale and Objectives

Water demand in the High Plateaus of eastern Algeria is rising rapidly, yet the mechanisms controlling groundwater recharge remain poorly quantified. The northern Upper Boussellam catchment—home to the Ain Zada Dam and vital agricultural plains—exemplifies this challenge: its complex geology, variable climate, and diverse land use drive highly heterogeneous recharge dynamics. This thesis therefore aims to develop an integrated, GIS-based framework for mapping groundwater recharge potential in the study area.

The specific objectives are:

1. To delineate geomorphic controls on infiltration using DEM-derived metrics (slope and drainage density) and to analyse the morphometric characteristics of the study area.
2. To characterize climatic drivers of recharge via long-term rainfall, temperature.
3. To assess hydrochemical signatures and piezometric gradients.
4. To explore the use of satellite imagery to map the various factors influencing groundwater recharge.
5. To integrate all factors in a weighted-overlay model and validate recharge potential zones.

1.6.1 Literature Review and Knowledge Gaps

Groundwater recharge—the process by which precipitation infiltrates the unsaturated zone and percolates to the water table—is fundamental to aquifer sustainability but notoriously difficult to quantify in semi-arid high-plateau settings. Challenges arise from spatial heterogeneity in soils and subsurface properties, temporal variability of climate inputs, and limited field observations. Erroneous assumptions and scarce monitoring infrastructure often lead to high uncertainty in recharge estimates. Geographic Information Systems (GIS) and Remote Sensing (RS) enable spatially explicit recharge mapping by integrating topography, lithology, land use, lineaments, and climate Coupled with Multi-Criteria Decision-Making (MCDM) techniques, GIS can weight these factors to delineate recharge-potential zones. A critical driver of recharge is precipitation intensity, yet station-based rainfall data often lack spatial distribution. The NASA LaRC POWER dataset fills this gap by providing gridded, global climatic variables that have been successfully used in hydrological and ecological research. Integrating POWER rainfall data into MCDM models enhances the representation of the primary recharge control.

Validation of recharge-potential maps typically employs Receiver Operating Characteristic (ROC) curves in combination with well-yield or spring discharge data. As a novel proxy, total dissolved solids (TDS) in shallow wells—sampled post-winter recharge—offer a low-cost, readily available indicator: higher recharge mobilizes solutes and elevates TDS concentrations.

Despite the maturity of individual methods, few studies have unified process-based insights, GIS–MCDM weighting, and field validation into a single framework. In particular, the Northern Upper Boussellam contribution to regional recharge remains under-examined. This thesis addresses these gaps by integrating DEM-derived morphometric controls, high-resolution climatic data, hydrochemical validation, and weighted-overlay modeling to produce and test a robust recharge-potential map for the northern Upper Boussellam catchment.

Chapter 2

DEM-Based Drainage Network Delineation and Morphometric Analysis.

2.1 Abstract

Quantitative morphometry offers a powerful means to describe drainage-basin form —measuring channel networks, basin shape, and relief—and underpins effective watershed management, sediment control, and groundwater-recharge estimation. In this study, we employ a 30 m ASTER DEM and QGIS to derive a comprehensive set of morphometric parameters for the northern Upper Boussellam catchment, which sustains the Ain Zada Dam via the Boussellam spring. Alongside classic indices (stream order, total channel length, bifurcation ratio, basin area, form and circularity ratios, elongation ratio, relief ratio, and channel maintenance constant), we calculate drainage density, drainage texture, ruggedness index, and infiltration number. We also generate a high-resolution slope map and a drainage-density map to highlight spatial gradients in surface inclination and drainage network development—two critical factors controlling runoff concentration versus diffuse infiltration. The overall Soummam Basin ranks as seventh order; its Sahel and Boussellam sub-basins are sixth order. Within our focus area, stream orders vary from three to five, reflecting diverse hydrological responses. Results indicate an infiltration-dominated regime, characterized by moderate slopes, low channel densities, and structurally guided subsurface flow paths. These insights serve as a foundation for zoning groundwater-recharge potential and formulating sustainable water-management strategies in this semi-arid plateau setting.

2.2 Introduction

Morphometric analysis—the quantitative examination of landforms and drainage networks—has long been a cornerstone in the study of hydrological and geomorphic processes (Clarck, 1966; Shekar & Mathew, 2022). Seminal work by Horton (1932, 1945), Strahler (1952, 1957, 1958), Leopold and Miller (1956), and Chorley (1969) established a framework linking indices such as drainage density, stream frequency, bifurcation ratio, and relief ratio to watershed behavior. These measures provide vital insights into flood potential, soil erosion, runoff patterns, and sediment transport, and—being expressed as ratios or dimensionless indices—allow objective comparisons across diverse landscapes.

Advances in Geographic Information Systems (GIS) and remote sensing have greatly improved the precision and efficiency of morphometric studies. High-resolution

Digital Elevation Models (DEMs), when coupled with modern analytical tools, enable automated extraction of drainage networks, computation of slope and curvature, and rapid calculation of complex indices. Such workflows replace labor-intensive field surveys and are especially valuable in semi-arid, structurally complex terrains where surface and subsurface flow interact.

This research focuses on the northern upper sector of the Upper Boussellam catchment, comprising four sub-catchments drained by the Boussellam Ouedi emerging from the Djebel Mégriss massif and feeding the Ain Zada Dam. With water resources under growing pressure from agricultural demand and climate variability, a detailed morphometric characterization is essential for identifying zones of preferential infiltration and runoff concentration.

Our methodology begins by hydro-conditioning a 30 m ASTER DEM in QGIS to enforce drainage continuity. From this, we extract the stream network and calculate drainage density—a metric quantifying total channel length per unit area and serving as a proxy for the balance between runoff concentration and diffuse infiltration. In a parallel workflow, we derive a high-resolution slope map to capture spatial gradients in surface inclination, which govern runoff velocity and recharge potential. Separating these workflows ensures each dataset is optimized for its analytical role.

We compute a comprehensive suite of parameters—stream order and count, bifurcation ratio, basin area, form factor, circularity and elongation ratios, relief ratio, channel maintenance constant, drainage texture, ruggedness index, infiltration number, and basin relief—that collectively reflect tectonic, lithological, and climatic controls on water movement. For example, low drainage density combined with moderate slopes typically indicates dominant subsurface flow, a key indicator of groundwater recharge potential.

By revealing spatial patterns in these morphometric indices, this chapter establishes a robust geomorphic framework for subsequent analyses—linking terrain attributes to hydro-climatological dynamics, hydrochemical signatures, and land-use impacts. The insights gained here will directly inform the weighted-overlay model for groundwater-recharge potential mapping, ultimately guiding sustainable water-management strategies in this semi-arid high-plateau region.

2.3 Method

2.3.1 Data Sources

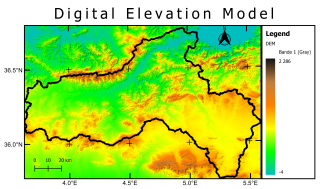
The Terra Advanced Spaceborne Thermal Emission and Reflection Radiometer (ASTER) Global Digital Elevation Model (GDEM) Version 3 (ASTGTM) provides a global digital elevation model (DEM) of land areas on Earth at a spatial resolution of 1 arc second (approximately 30-meter horizontal posting at the equator). Downloaded from United State Geological Survey (USGS) website: https://earthexplorer.usgs.gov/

2.3.2 Analytical Approach

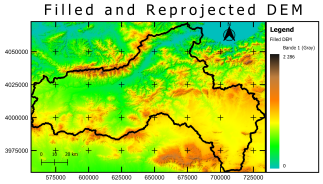
Our GIS workflow consists of three parallel branches, all beginning with the conditioned ASTER GDEM v3 mosaic (30 m):

- **Stream network extraction**
- **Drainage density mapping**
- **Slope map derivation**

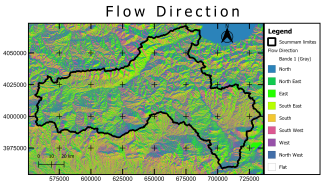
Stream network extraction Six ASTER GDEM v3 scenes were mosaicked and reprojected to UTM 31 N. We applied (Wang & Liu, 2006) fill sinks tool to remove spurious pits and enforce continuous flow. From the conditioned DEM we computed flow direction and flow-accumulation rasters, then used Strahler ordering to extract a six order vector stream network. Pour points at the Soummam outlet into the Mediterranean, the Sahel and Boussellam sub-basin confluences, and the Ain Zada dam inflow were used to delineate catchments. Whereas the outlets of the Upper Boussellam sub-catchments were defined as the junctions' points with the 6th Strahler order. We choose this method because it allows us to derive the catchment from any points which belong to the stream network. The mainstream of the Upper Boussellam catchment receives a discharge from multiple drainage basin orders. It has 9 sub-catchments with different orders. The flow direction map and the DEM are used together to extract the distance of the flow path and the maximum distance. Stream segments of identical order were merged to calculate total channel length and maximum flow-path distance. The flow direction map and the DEM are used together to extract the distance of the flow path and the maximum distance. Areal morphometric characteristics, such as the area and perimeter of the drainage basin, are calculated in QGIS using the raster calculator. This tool uses map units to derive catchments and compute their respective morphometric properties.



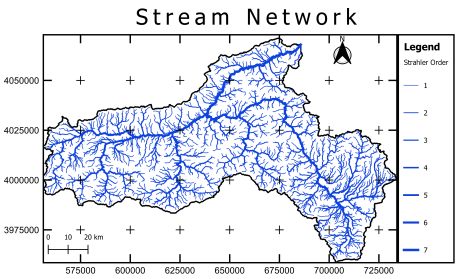
(A) Raw ASTER DEM



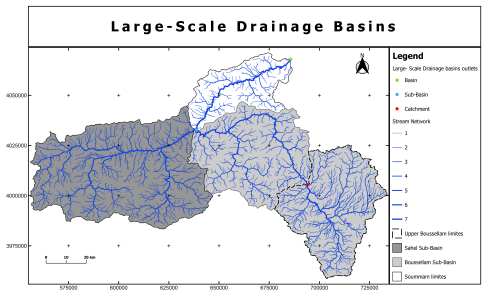
(B) Filled & reprojected DEM



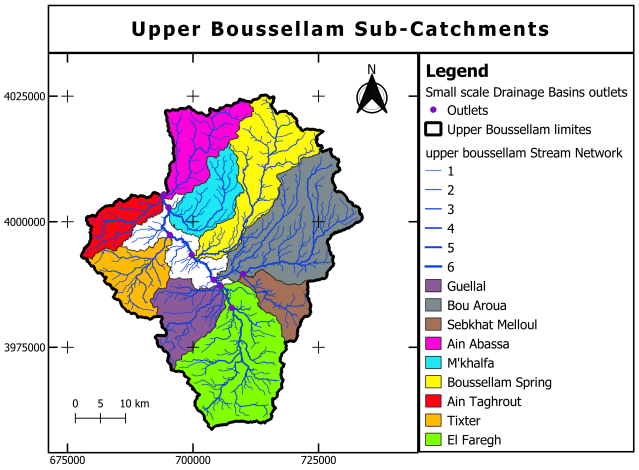
(C) Flow direction



(D) Stream network



(E) Drainage basins



(F) Upper Boussellam sub-catchments

FIGURE 2.1: Workflow for ASTER DEM conditioning, flow-direction/accumulation, stream-network extraction, and catchment delineation.

Drainage density mapping Drainage density was derived after extracting the stream network and calculating total channel length per unit area (km $\times$ km^{-2}). We overlaid a 1 km $\times$ 1 km fishnet on the network, summed channel length per cell, and interpolated fishnet-centroids via ordinary kriging to produce a continuous surface.

Slope map derivation Raster slope (%) were computed directly from the DEM using GIS after extracting aspect and determining slope angles. By isolating these three workflows—stream extraction, drainage-density mapping, and slope-map derivation—we optimized each process for accuracy. These layers underpin subsequent morphometric index calculations and groundwater-recharge potential mapping.

2.4 Results and discussion

2.5 Linear morphometric parameters

In morphometric analysis, the linear aspect refers to the one-dimensional characteristics of a drainage basin that describe the structure of its stream network. As shown in Table 2.1, these parameters—including the number of streams at each order, stream lengths, length ratios, and bifurcation ratios—provide critical insights into the hydrological behavior of the basin

TABLE 2.1: Linear Characteristics of Drainage Basins.

Linear Parameters					
Name of the Basin	**Upper Boussellam**	**Kharoua)**	**M'khalfa**	**Boussellam Spring**	**Bou Aroua**
Basin Order					
Basin Order	6	3	4	4	4
Number of Streams					
1st	433	35	26	58	76
2nd	94	4	7	15	16
3rd	26	1	2	3	6
4th	7	—	1	1	1
5th	2	—	—	—	—
6th	1	—	—	—	—
Total	563	40	36	77	99
Length of Streams (m)					
1st	840,91	60,69	67,69	111,70	159,74
2nd	412,95	34,73	22,04	49,84	89,46
3rd	234,39	23,19	21,24	34,61	61,42
4th	76,42	—	4,89	22,34	27,50
5th	6,35	—	—	—	—
6th	28,16	—	—	—	—
Total	1599,18	118,61	115,87	218,49	338,11
Mean Stream Length (m)					
1st	1,94	1,73	2,60	1,93	2,10
2nd	4,39	8,68	3,15	3,32	5,59
3rd	9,02	23,19	10,62	11,54	10,24
4th	10,92	—	4,89	22,34	27,50
5th	3,17	—	—	—	—
6th	28,16	—	—	—	—
Stream Length Ratio (Lr)					
L2/L1	0,49	0,57	0,33	0,45	0,56
L3/L2	0,57	0,67	0,96	0,69	0,69
L4/L3	0,33	—	0,23	0,65	0,45
L5/L4	0,08	—	—	—	—
L6/L5	4,44	—	—	—	—
Bifurcation Ratio (Rb)					
Ns1/Ns2	4,61	8,75	3,71	3,87	4,75
Ns2/Ns3	3,62	4,00	3,50	5,00	2,67
Ns3/Ns4	3,71	—	2,00	3,00	6,00
Ns4/Ns5	3,50	—	—	—	—
Ns5/Ns6	2,00	—	—	—	—
Average Bifurcation Ratio					
Average	3,49	6,38	3,07	3,96	4,47

Stream Order

Most current studies (Bogale, 2021; Sankriti et al., 2021) adopt the Strahler stream-order model, which assigns order 1 to the smallest channels and increments by one

when two streams of the same order join (Strahler, 1964).

Table 2.1 shows that the Upper Boussellam main catchment reaches 6th order, reflecting its position at the Boussellam (6th order) river. Among the Northern Upper Boussellam subcatchments, Kharoua is only 3rd order, whereas M'khalfa, Boussellam Spring and Bou Aroua all attain 4th order. These differences confirm that Kharoua occupies a headwater position with fewer tributary junctions, while the other three subcatchments are more hydrologically developed.

Stream Number

Stream Number (N_u) = Number of streams by Strahler order parenciteStrahler1957

The counts in Table 2.1 reveal a clear decline in segment number with increasing order in every basin. First-order streams dominate: they amount to 433 (77 %) of 563 segments in Upper Boussellam, 35 (87.5 %) of 40 in Kharoua, 26 (72.2 %) of 36 in M'khalfa, 58 (75.3 %) of 77 in Boussellam Spring and 76 (76.8 %) of 99 in Bou Aroua. The particularly high share of 1st-order channels in Kharoua indicates a finely dissected headwater network, whereas M'khalfa's lower proportion suggests a somewhat more balanced distribution among orders.

Bifurcation Ratio

$$\text{Bifurcation Ratio } (R_b) = \frac{N_u}{N_{u-1}} \quad \text{(Horton, 1945)}$$

The bifurcation ratio (Rb) for successive stream-order transitions was calculated for five sub-basins— Upper Boussellam, Kharoua, Mkhalfa, Boussellam Spring, and Bou Aroua—revealing distinct branching characteristics across the network Table 2.1. Upper Boussellam exhibits a systematic decrease from 4.61 (Ns1/Ns2) to 2.00 (Ns5/Ns6). Kharoua records an exceptionally high headwater value (8.75 at Ns1/Ns2) followed by a moderate drop to 4.00 (Ns2/Ns3). Mkhalfa shows relatively uniform ratios between 3.71 and 2.00 across the first three transitions. Boussellam Spring has elevated Rb at Ns2/Ns3 (5.00) but moderate values elsewhere. Bou Aroua presents Rb values of 4.75, 2.67, and 6.00 for the first three transitions, indicating localized variability in mid-order channel development.

The average bifurcation ratio (bottom row of Table 2.1) ranges from 3.07 in M'khalfa to 6.38 in Kharoua, with Boussellam Spring at 3.96 and Bou Aroua at 4.47. M'khalfa's low R_b indicates a mature, structurally unconfined network, while Kharoua's high $R_b > 5$ signals strong lithologic or tectonic control on tributary junctions. The intermediate values for Boussellam Spring and Bou Aroua suggest moderate geological influence on their drainage patterns.

Stream Length

The length of a stream, defined as the distance measured along the stream channel from its source to a given outlet, is a crucial parameter in hydrological studies. Stream lengths were computed using the QGIS raster calculator and provide insight into catchment slope and infiltration potential (Morisawa, 1962; Withanage et al., 2014).

Results. The total stream length in the Boussellam basin is 2880.96 km. The Upper Boussellam sub-basin—55 % of the total area—accounts for 1599.18 km of that length. Among the four Northern Upper Boussellam subcatchments (Table 2.1):

- Bou Aroua: 338.11 km
- Boussellam Spring: 218.49 km
- Kharoua: 118.61 km
- M'khalfa: 115.87 km

Mean Stream Length

$$\text{Mean Stream Length } (L_m) = \frac{L_u}{N_u} \quad \text{(Horton, 1945)}$$

Mean stream length (L_m) quantifies the average channel segment size at each Strahler order (Horton, 1945; Strahler, 1964).

In Upper Boussellam, L_m rises from 1.94 m (1st order) to 28.16 m (6th order). Subcatchment trends are:

- Bou Aroua: 2.10 m $\rightarrow$ 27.50 m (Orders 1 $\rightarrow$ 4)
- Boussellam Spring: 1.93 m $\rightarrow$ 22.34 m (Orders 1 $\rightarrow$ 4)
- M'khalfa: 2.60 m $\rightarrow$ 3.15 m $\rightarrow$ 10.62 m $\rightarrow$ 4.89 m (Orders 1 $\rightarrow$ 4), with an anomalous drop at Order 4.
- Kharoua: 1.73 m $\rightarrow$ 23.19 m (Orders 1 $\rightarrow$ 3)

Stream Length Ratio

$$\text{Stream Length Ratio } (L_r) = \frac{L_u}{L_{u-1}} \quad \text{(Horton, 1945)}$$

The stream-length ratio (L_r) measures the scaling of mean segment lengths between successive orders.

All subcatchments exhibit $L_2/L_1 < 1$, indicating shorter 2nd-order reaches compared to abundant 1st-order tributaries. Specific values (Table 2.1):

- L_2/L_1: M'khalfa (0.33) < Boussellam Spring (0.45) < Bou Aroua (0.56) < Kharoua (0.57)
- L_3/L_2: M'khalfa (0.96) > Bou Aroua (0.69) = Boussellam Spring (0.69) > Kharoua (0.67).

2.5.1 Discussion of Linear Morphometric Parameters

Table 2.1 summarizes key Strahler-based metrics—stream order, number, length and branching—that reflect underlying geomorphic controls and inform hydrological behavior (Horton, 1945; Strahler, 1957, 1964).

Spatial Variability in Linear Parameters

The computed linear parameters—mean stream length (L_m), stream-length ratio (L_r) and bifurcation ratio (R_b)—reveal clear spatial heterogeneity across the four Northern Upper Boussellam subcatchments (Table 2.1). These variations reflect underlying lithologic contrasts, relief differences and structural controls on drainage development.

Mean Stream Length and Flood Risk Mean stream length generally increases with order, indicating elongation of higher-order channels. However, in the M'khalfa subcatchment, we observe an anomalous decrease of L_m in higher orders (Order 2 to Order 3). Such a pattern suggests that short, steep segments concentrate flow into a confined channel, elevating local water pressure and flash-flood potential (Chopra et al., 2005; Prabhakaran & Raj, 2018).

Bifurcation Ratios and Structural Controls The pronounced Rb of 8.75 in Kharoua at the first-order transition suggests intense channel initiation, likely driven by steep local relief or structurally controlled fault lines that enhance overland flow concentration and flash-flood susceptibility in headwater zones.

Upper Boussellam's gradual decline in Rb from 4.61 to 2.00 reflects a classic maturity gradient: densely branched upland headwaters evolve into more streamlined lower-order channels, indicative of balanced runoff and subsurface exchange within mixed lithologies.

Mkhalfa's consistent ratios around 3.0–3.7 imply a relatively homogeneous physiographic setting where moderate slope gradients and uniform bedrock permeability yield stable branching patterns without extreme flood potential.

Boussellam Spring displays an anomalously high second-order ratio (5.00), pointing to localized recharge influx or concentrated flow converging into fewer, dominant channels.

Bou Aroua's mid-order spike (6.00 at Ns3/Ns4) signals an area of intensified upstream catchment integration, possibly reflecting abrupt lithological changes or structural controls that segment the drainage network and elevate runoff efficiency.

Overall, higher bifurcation ratios correspond to steeper slopes and greater runoff production, whereas lower values denote gentler gradients and reduced flood potential, underscoring the combined influence of physiography, lithology, and tectonics on drainage architecture.

The average bifurcation ratio ranges from 3.07 (M'khalfa) to 6.38 (Kharoua). M'khalfa's low R_b is characteristic of a mature, structurally unconfined drainage, whereas Kharoua's high $R_b > 5$ points to strong geologic or tectonic guidance of tributary junctions (Schumm, 1954; Strahler, 1957). Boussellam Spring (3.96) and Bou Aroua (4.47) occupy intermediate positions, suggesting moderate lithologic control.

Hydrological Implications

- **Runoff Response.** Kharoua's dense first-order network and elevated R_b imply rapid concentration of runoff and heightened flash-flood risk.
- **Infiltration Potential.** Bou Aroua's long total stream length (338.1 m) and moderate branching suggest a broader catchment footprint with gentler slopes—conditions conducive to higher infiltration and baseflow.
- **Water Resource Management.** The distinct linear signatures of each subcatchment can inform targeted flood mitigation and recharge enhancement measures.

Headwater Dissection in Kharoua Kharoua's limitation to 3rd order and its dominance of first-order streams (87.5 %) signal a classic headwater network with steep slopes (Strahler, 1957). Its exceptionally high bifurcation ratio (R_b = 6.38) exceeds the typical 2–5 range for structure-free basins (Schumm, 1954), confirming strong lithologic or tectonic guidance of tributary junctions.

Network Uniformity in M'khalfa Despite reaching 4th order, M'khalfa exhibits a low average R_b = 3.07—well within the expected range for mature drainage (Strahler, 1957)—and a compact stream-length ratio (L_2/L_1 = 0.33). The anomalous drop in mean stream length at Order 4 further points to subtle structural controls that concentrate flow and elevate local flood risk (Chopra et al., 2005; Prabhakaran & Raj, 2018).

Extent and Infiltration Potential in Boussellam Spring and Bou Aroua Both subcatchments attain 4th order but differ in network elongation and branching. Bou Aroua's extensive total length and moderate R_b = 4.47, alongside Boussellam Spring's intermediate values (R_b = 3.96), imply gentler average gradients and larger contributing areas—conditions that favor infiltration and sustained baseflow (Morisawa, 1962; Withanage et al., 2014).

Integrating Stream Number and Morphometric Theory Across all basins, the steep decline in stream number with increasing order aligns with Strahler's original observations (Strahler, 1957), and the proportion of first-order channels serves as a proxy for slope intensity and runoff velocity.

Integrated Hydrological Implications – Rapid runoff and high flood peaks are most likely in Kharoua and, to a lesser extent, in those reaches of M'khalfa where mean-length anomalies concentrate flows. – Enhanced infiltration and recharge potential characterize Bou Aroua and Boussellam Spring, suggesting these subcatchments as prime sites for managed aquifer recharge. – M'khalfa's uniform network, despite its compactness, may benefit from targeted retention structures at Order 3→4 junctions to buffer sudden flow surges.

Hydrological and Management Implications – *Flood hotspots*: Kharoua and M'khalfa's compact, highly branched networks demand upstream retention or check-dam interventions. – *Recharge zones*: Bou Aroua and Boussellam Spring, with elongated channels and moderate branching, are ideal candidates for managed aquifer recharge projects. – *Standardized morphometry*: Employing Strahler's hierarchy ensures comparability across subcatchments and underpins reliable hydrological modeling (**Bogale2021**; Sankriti et al., 2021).

These integrated morphometric insights offer a robust basis for subcatchment-specific flood mitigation, recharge enhancement and sediment-transport assessments.

2.6 Areal morphometric parameters

The form and dimensions of a drainage basin can be deduced through the analysis of its areal characteristics. In this study, several parameters were considered to characterize the areal aspect of the drainage basin, including basin area, form factor, elongation ratio, circularity ratio, drainage density, drainage texture, infiltration number, stream frequency, and length of overland flow. These parameters provide valuable information for understanding the shape and size of the drainage basin and its hydrological characteristics. Table 2.2 summarizes the areal morphometric characteristics of the drainage basins in our study area. A close examination of the results reveals distinct differences in the shape, size, and structural complexity of these basins.

TABLE 2.2: Areal Morphometric Characteristics of Drainage Basins.

Areal Morphometric Characteristics					
Parameter	**Upper Boussellam**	**Kharoua**	**Mkhalfa**	**Boussellam Spring**	**Bou Aroua**
Basin Area (km^2)	2073,59	181,23	141,53	301,16	397,45
Basin Perimeter (km)	340,17	105,68	87,63	163,89	156,49
Perimeter Squared (km^2)	115712,23	11167,80	7679,80	26858,90	24487,56
Maximum Flow Distance (km)	78,10	37,91	32,79	53,57	51,99
Maximum Distance Squared (km^2)	6100,23	1437,17	1075,32	2869,53	2703,38
Form Factor	0,34	0,13	0,13	0,10	0,15
Circularity Ratio	0,23	0,20	0,23	0,14	0,20
Elongation Ratio	0,66	0,40	0,41	0,37	0,43
Drainage Density (km^{-1})	0,77	0,65	0,82	0,73	0,85
Drainage Texture	1,66	0,38	0,41	0,47	0,63
Stream Frequency	0,27	0,22	0,25	0,26	0,25
Channel Maintenance Constant	1,30	1,53	1,22	1,38	1,18
Infiltration Number	0,21	0,14	0,21	0,19	0,21
Drainage Intensity	0,35	0,34	0,31	0,35	0,29
Average Overland Flow Length	0,39	0,33	0,41	0,36	0,43

Basin Area and Perimeter

The Upper Boussellam catchment covers 2 073.6 km^2 — 51.8 % of the Boussellam sub-basin. Among its four principal subcatchments, Bou Aroua (397.5 km^2) and Boussellam Spring (301.2 km^2) are markedly larger than Kharoua (181.2 km^2) and M'khalfa (141.5 km^2). Perimeter lengths follow the same hierarchy: Upper Boussellam (340.2 km), Boussellam Spring (163.9 km), Bou Aroua (156.5 km), Kharoua (105.7 km), M'khalfa (87.6 km).

Form Factor and Elongation Ratio

$$\text{Form Factor} = \frac{A}{Fd^2} \quad \text{(Horton, 1945)}$$

$$\text{Elongation Ratio} = \frac{2\sqrt{\frac{A}{\pi}}}{Fd} \quad \text{(Schumm, 1956)}$$

Form factors (0.10–0.34) all lie below the 0.45 threshold for circular basins, confirming elongation. Upper Boussellam (0.34) is the least elongated, while Boussellam Spring (0.10) is the most ribbon-shaped. Elongation ratios (0.37–0.66) corroborate this: Upper Boussellam (0.66) and Bou Aroua (0.43) approach more equidimensional outlines, whereas Kharoua (0.40), M'khalfa (0.41) and Boussellam Spring (0.37) are markedly stretched.

Circularity Ratio

$$\text{Circularity Ratio} = \frac{4\pi A}{P^2} \quad \text{(Miller, 1953)}$$

Values range from 0.14 (Boussellam Spring) to 0.23 (Upper Boussellam, M'khalfa), reinforcing highly elongated basin geometries. Such low ratios are typical of mature, plateau–plain systems where channels adjust to gentle regional gradients (Schumm, 1954).

Drainage Density and Texture

$$\text{Drainage Density } (D_d) = \frac{L_t}{A} \quad \text{(Horton, 1945)}$$

$$\text{Drainage Texture } (D_t) = \frac{S_t}{P} \quad \text{(Horton, 1945)}$$

Drainage density spans 0.65 km^{-1} (Kharoua) to 0.85 km^{-1} (Bou Aroua), indicating tighter channel networks in larger, flatter basins. Upper Boussellam's 0.77 km^{-1} sits mid-range. Texture values (0.38–1.66) show Upper Boussellam's main basin (1.66) is most erosion-prone, while subcatchments (<0.9) exhibit coarser, less erosion-susceptible networks.

Drainage Intensity

$$\text{Drainage Intensity } (D_i) = \frac{S_f}{D_d} \quad \text{(Faniran, 1968)}$$

Drainage intensity, combining stream frequency and density, remains low across all basins (0.29–0.35). These low D_i values confirm coarse textures and high infiltration potential, indicating generally limited surface denudation.

Stream Frequency

$$\text{Stream Frequency } (S_f) = \frac{S_t}{A} \quad \text{(Horton, 1945)}$$

Stream frequency quantifies the number of stream segments per unit area, linking network density to infiltration and relief (Imran et al., 2013; Thomas et al., 2010).

Results. All basins exhibit low S_f (0.22–0.27 km^{-1}), indicating high bedrock permeability and substantial rainfall infiltration across the catchments.

Average Overland Flow Length

$$\text{Average Length of Overland Flow } (L_{of}) = \frac{1}{2 \times D_d} \quad \text{(Horton, 1945)}$$

This metric estimates the travel distance of sheet flow before channel initiation; values <0.4 km suggest pronounced channel erosion and flash-flood risk (Olszevski et al., 2011).

Results. Mkhalfa (0.41 km) and Bou Aroua (0.43 km) exceed the 0.4 km threshold, indicating longer sheet-flow travel distances, greater opportunity for infiltration, and a slower concentration of runoff — conditions generally associated with reduced flash-flood susceptibility and lower channelized erosion risk.

In contrast, Boussellam Spring (0.36 km) and Kharoua (0.32 km) fall below the threshold, reflecting shorter overland flow paths, rapid runoff concentration into channels, and a higher potential for channel erosion and flash-flood occurrence.

Constant of Channel Maintenance

$$\text{Constant of Channel Maintenance } (C_c) = \frac{1}{D_d} \quad \text{(Schumm, 1956)}$$

Channel maintenance constant represents the area required to sustain one kilometer of channel, inversely tied to drainage density (Sakthivel et al., 2019). High C_c values imply permeable substrates and minimal structural constraints.

Results. Values range from 1.18 km²/km (Bou Aroua) to 1.53 km²/km (Kharoua), suggesting all subcatchments possess highly permeable lithologies. Kharoua's peak C_c underscores its exceptional permeability and lithologic control.

Infiltration Number

$$\text{Infiltration Number } (I_n) = S_f \times D_d \quad \text{(Faniran, 1968)}$$

Infiltration number combines stream frequency and density to gauge runoff vs. infiltration potential (Elewa et al., 2016).

Results. Kharoua (0.14) and Boussellam Spring (0.19) show higher infiltration numbers—indicating stronger infiltration capacity—while Mkhalfa (0.21) and Bou Aroua (0.21) register lower values associated with higher runoff potential.

2.6.1 Discussion of Areal Morphometric Parameters

The areal morphometric metrics (Table 2.2) collectively paint a picture of elongated, plateau–plain basins with variable runoff, infiltration and erosion traits. All subcatchments exhibit low form factors (0.10–0.34) and circularity ratios (0.14–0.23), reflecting the ribbon-shaped geometries that promote lower peak flows sustained over longer durations (Chopra et al., 2005; Nautiyal, 1994).

Larger subcatchments—Bou Aroua (397.5 km²) and Boussellam Spring (301.2 km²) —enjoy an inherent advantage in mean annual runoff, consistent with the positive area–runoff relationship described by Leopold and Maddock (Leopold & Miller, 1956) and Morisawa (Morisawa, 1962). Their moderate drainage densities (0.73–0.85 km^{-1}) and coarse textures ($D_t < 0.9$) further suggest that a significant portion of precipitation contributes to sustained baseflow rather than immediate surface runoff (Horton, 1945; Smith, 1950).

Stream frequency ($S_f = 0.22$–$0.27\ \text{km}^{-1}$) and infiltration number ($I_n = S_f\, D_d = 0.14$–0.21) are uniformly low, confirming high bedrock permeability and rainfall infiltration across the study area (Faniran, 1968; Thomas et al., 2010). Among

the subcatchments, Kharoua's combination of low S_f and high channel - maintenance constant ($C_c = 1/D_d = 1.53\,\text{km}^2/\text{km}$) underscores exceptional substrate permeability and lithologic control, making it a prime candidate for managed recharge initiatives (Sakthivel et al., 2019; Schumm, 1956).

Average overland-flow lengths ($L_{of} = 1/2D_d$) range from 0.32 km (Kharoua) to 0.43 km (Bou Aroua). Mkhalfa (0.41 km) and Bou Aroua (0.43 km) exceed the 0.4 km threshold, indicating stronger sheet-flow regimes and lower flash-flood susceptibility, whereas Kharoua and Boussellam Spring fall below and thus concentrate flow rapidly into channels (Horton, 1945; Olszevski et al., 2011).

Upper Boussellam's high drainage texture ($D_t = 1.66$) flags zones of elevated erosion risk, contrasting with its subcatchments' coarse networks. In combination with their elongated plans, these metrics inform a tiered management strategy:

- Implement check-dams and vegetative buffers in high-texture corridors of Upper Boussellam.
- Target infiltration-enhancement structures (e.g., recharge basins) in Kharoua and Boussellam Spring, where permeability and low surface runoff converge.
- Leverage Mkhalfa and Bou Aroua's sheet-flow dominance for optimized runoff retention and delayed peak discharge.

By integrating these areal characteristics with linear morphometry, we establish a robust, subcatchment-specific framework for flood mitigation, soil-erosion control and groundwater recharge planning.

2.7 Relief aspect

Relief is an important attribute of a drainage basin. It measures the potential energy of the drainage system and can provide insight into the potential for soil erosion within the basin. Several relief aspects can be considered when studying a drainage basin, including total basin relief, relief ratio, and ruggedness number. These aspects can help to determine the intensity of soil erosion in a given basin. Table 2.3 summarizes the relief morphometric characteristics for the drainage basins, including key parameters such as maximum and minimum elevation, relief ratios, and ruggedness number.

TABLE 2.3: Relief Morphometric Characteristics of Drainage Basins.

Relief Morphometric Characteristics					
Parameter	**Upper Boussellam**	**Kharoua**	**M'khalfa**	**Boussellam Spring**	**Bou Aroua**
Maximum H (m)	1758,00	1741,00	1341,00	1739,00	1438,00
Minimum H (m)	851,04	851,05	851,59	877,04	887,04
Mean H (m)	1024,34	1117,76	977,29	1094,45	1003,71
Total Basin Relief (m)	906,96	889,95	489,41	861,96	550,96
Basin Relief (km)	0,91	0,89	0,49	0,86	0,55
Relief Ratio	0,01	0,03	0,03	0,02	0,02
Relative Relief Ratio	266,62	842,13	558,47	525,95	352,09
Ruggedness Number	0,70	0,58	0,40	0,63	0,47
Horizontal Distance (km)	—	26,90	16,00	35,50	33,00

Total Basin Relief

Basin relief (R) is defined as the difference between maximum and minimum elevations and represents the potential energy driving erosion and sediment transport (Strahler, 1964). **Results (Table 2.3):**

- Upper Boussellam: $R = 1758.00 - 851.04 = 906.96\,\text{m}$
- Kharoua: $1741.00 - 851.05 = 889.95\,\text{m}$
- M'khalfa: $1341.00 - 851.59 = 489.41\,\text{m}$
- Boussellam Spring: $1739.00 - 877.04 = 861.96\,\text{m}$
- Bou Aroua: $1438.00 - 887.04 = 550.96\,\text{m}$

Relief Ratio

$$\text{Relief Ratio} = \frac{R}{L_h} \quad \text{(Schumm, 1956)}$$

Relief ratio expresses watershed steepness by normalizing relief (R) by the maximum basin length (L_h). **Results:**

- Upper Boussellam: 0.018
- Kharoua: 0.033
- M'khalfa: 0.031
- Boussellam Spring: 0.024
- Bou Aroua: 0.017

Ruggedness Number

$$\text{Ruggedness Number} = R \times D_d \quad \text{(Strahler, 1958)}$$

The ruggedness number combines relief (R) with drainage density (D_d) to gauge terrain instability and erosion susceptibility. **Results:**

- Upper Boussellam: $906.96 \times 0.77 = 0.70$
- Kharoua: $889.95 \times 0.65 = 0.58$
- M'khalfa: $489.41 \times 0.82 = 0.40$
- Boussellam Spring: $861.96 \times 0.73 = 0.63$
- Bou Aroua: $550.96 \times 0.85 = 0.47$

2.7.1 Discussion of Relief Morphometric Parameters

High basin relief in Upper Boussellam (907 m), Kharoua (890 m) and Boussellam Spring (862 m) indicates substantial potential energy for erosion, consistent with observed high denudation rates in steep basins (Anhurt, 1970; Gregory & Walling, 1973). M'khalfa's low relief (489 m) suggests gentler slopes and reduced erosive force, while Bou Aroua's moderate relief (551 m) positions it between these extremes.

Relief ratios peak in Kharoua (0.033) and M'khalfa (0.031), highlighting these subcatchments as the steepest and most erosion-intense (Schumm, 1956). Bou Aroua's low relief ratio (0.017) confirms its comparatively mild gradient and slower erosion rates.

Ruggedness numbers reinforce this pattern: Boussellam Spring (0.63) and Kharoua (0.58) exhibit the greatest terrain instability, while M'khalfa (0.40) and Bou Aroua (0.47) are more stable (Strahler, 1958). The highest ruggedness in Upper Boussellam (0.70) reflects the combined effect of its large relief and moderate drainage density, flagging it as a priority zone for erosion control.

Collectively, relief morphometry underscores the need for targeted management: steep, high-relief basins (Kharoua, Boussellam Spring) demand rigorous soil-conservation measures, whereas gentler basins (M'khalfa, Bou Aroua) will benefit more from infiltration enhancement and graded slope stabilization.

2.8 Mapping Drainage density and Slope

Drainage Density Map Extracted from the Strahler-ordered network and computed on a 100 m grid, the drainage density map (Fig. 2.2) ranges from 0 to 2.2 km km^{-2}. Unlike the catchment-wide D_d values—which collapse spatial variability into a single average—this high-resolution map reveals intra-basin heterogeneity in channel concentration. Zones of elevated D_d (dark shading) pinpoint areas of efficient surface runoff and potentially reduced infiltration, while low-density pockets (light shading) mark sectors where subsurface recharge is more likely.

Scientific Advantages of Fine-Scale Mapping Capturing Heterogeneity: Small-scale D_d mapping resolves local controls (e.g. micro-topography, soil permeability, land-use changes) that an aggregated basin value cannot. Targeted Management: By identifying runoff hotspots and recharge zones at 100 m resolution, planners can site check-dams, infiltration basins or erosion-control measures with greater precision.

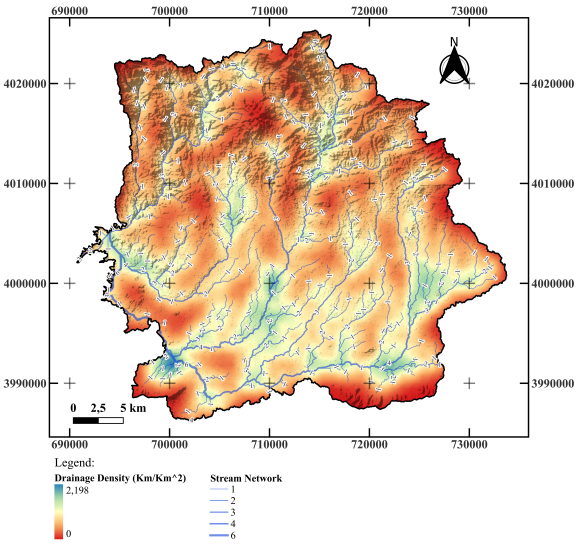


FIGURE 2.2: Drainage density map of the northern Upper Boussellam catchment, computed on a 1 km^{-2} grid using a conditioned ASTER DEM.

Slope map Derived separately from the conditioned ASTER DEM using QGIS's slope tool, the gradient ranges from 0 % to 41.94 % as shown in Figure 2.3. The map helps to capture variations in terrain steepness and its control on infiltration versus runoff. Terrain steepness is a primary control on surface runoff versus infiltration, making the slope layer a key input for recharge-potential zoning. This layer feeds directly into our recharge-potential model as a key topographic factor.

The steepest slopes (>30 %) occur in the northern sector—particularly in the Kharoua subcatchment—providing a clear topographic basis for its headwater network (3rd order, first-order streams 87.5 %, $R_b = 6.38$) and rapid runoff concentration. Across all basins, the steep decline in stream number with increasing order aligns with Strahler's original observations and underscores how the proportion of first-order channels serves as a proxy for slope intensity and runoff velocity.

This spatial coherence between slope heterogeneity and linear morphometry confirms slope as a dominant control on surface runoff versus infiltration and justifies its integration as a primary input in our recharge-potential zonation model.

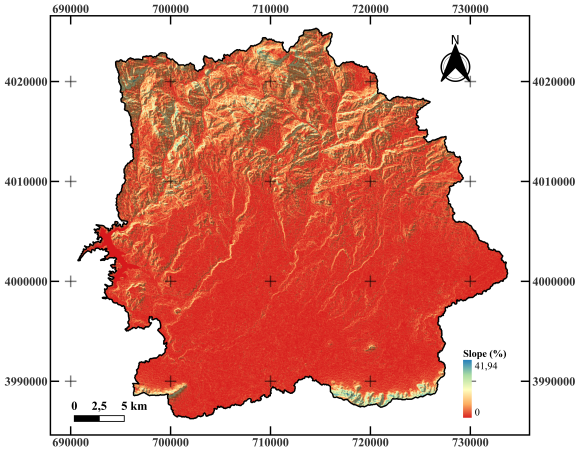


FIGURE 2.3: Slope gradient map of the northern Upper Boussellam catchment, derived from ASTER GDEM v3 (30 m resolution).

Mapping drainage density and the slope gradient at a fine scale complements subcatchment averages by exposing the spatial signatures of hydrologic processes, thereby enabling more nuanced scientific analysis and resource management. In Chapter 6 these slope and drainage-density layers will be integrated with LULC, lineament density, hydrochemical and climatological datasets in a GIS-based multi-criteria framework to delineate zones of high, moderate and low groundwater-recharge potential.

2.9 Conclusion

The morphometric analysis of the Northern Upper Boussellam catchment—based on a 30 m ASTER DEM and QGIS—has provided a comprehensive picture of watershed form and function. Linear indices (bifurcation ratio, stream length ratio, average length of overland flow) elucidated structural, lithological, and topographical controls on drainage behavior, pinpointing areas susceptible to flow concentration and flash flooding. Areal parameters (infiltration number, channel maintenance constant, basin shape) confirmed the dominance of permeable materials and subsurface flow. The drainage-density map, with values ranging from 0 to 2.2 km km^{-2} further distinguished zones of efficient runoff from high recharge potential areas.

In a parallel workflow, the slope map—deriving per-pixel gradients (0 %–41.94 %) from the same DEM—quantified terrain steepness across five classes. This topographic layer reinforced our understanding of infiltration versus runoff controls, identifying gentle slopes as key recharge zones.

Relief based metrics (relief ratio, ruggedness index) highlighted basins under active denudation and gully erosion, especially within the Upper Boussellam sub-catchments. Overall, the catchment exhibits low peak, long duration flows dominated by infiltration and subsurface pathways, underscoring significant groundwater potential in northern sub-basins.

The use of a high resolution ASTER DEM was crucial: it enabled seamless extraction of the stream network, drainage basins, slope, and other morphometric layers within a unified digital framework. This reproducible GIS approach can be readily applied to other small-scale basins, providing critical input for soil and water-resource management.

Together, these results furnish a robust basis for prioritizing watershed interventions, zoning recharge potential, and designing sustainable land-and-water management strategies in semi-arid high-plateau environments.

The results of this study are essential for developing a better soil and water resources management plan in the study area. By focusing on small-scale basins and analyzing these parameters ze could deduce information about runoff potential and identified areas threatened by flash flooding and exposed to water pressure.

Overall, this study has helped in understanding the form, geomorphic, erosional, and hydrologic processes of the watersheds of the Northern Upper Boussellam. This informations can serve as essential input towards prioritizing watersheds for formulating effective strategies for land and water management of this important resource. The approaches used in this study can be applied to any drainage system elsewhere.

Building on the DEM based morphometric framework—stream network extraction, drainage density mapping, and slope map derivation. Chapter Three will examine the climate setting of the Northern Upper Boussellam catchment. We will integrate rainfall patterns and temperature regimes, laying the groundwork for hydrochemical analyses and recharge potential modeling.

Chapter 3

Climatology

3.1 Abstract

This chapter presents an intensive climatic evaluation of the northern part of the upper Boussellam catchment, with a focused investigation on the prevailing climate type, recharge periods, and the spatial-temporal distribution of rainfall and temperature. Utilizing long-term datasets from NASA LARC POWER integrated via QGIS, the study maps both the overall climatic trends and the localized variations in each of the four sub-catchments. A key objective was to classify the regional climate at a sub-catchment scale, thereby establishing a critical framework for understanding individual hydrological responses and groundwater recharge processes. The detailed analysis has enabled the identification of distinct recharge periods, effectively bridging important data gaps related to the temporal and spatial dynamics of precipitation and temperature. The refined climate classification, together with the spatially distributed evaluation, offers significant insights for the sustainable management of water resources under increasing climatic pressures.

3.2 Introduction

The impacts of climate change are manifesting worldwide through shifts in hydrological processes, notably affecting soil infiltration, surface runoff, and groundwater recharge. Rises in global temperatures alter evaporation rates and precipitation patterns, thereby challenging traditional water resource management practices. In regions where water scarcity is acute, such as semi-arid basins, a robust understanding of these dynamics is essential for sustainable management and adaptive planning.

This thesis focuses on the northern part of the upper Boussellam catchment, an area of considerable hydrological importance that is divided into four distinct sub-catchments. The study area presents unique challenges—primarily due to the scarcity of local meteorological data. With only one meteorological station available over an expansive area of more than 1100 km^2, conventional data sources are insufficient for characterizing the spatial variability of climate. To overcome this limitation, freely available satellite-based datasets, such as those from NASA's LARC POWER project, have been employed. These data provide long-term records of temperature and rainfall at a spatial resolution that is capable of resolving local variations, thereby allowing for a detailed climate analysis at the sub-catchment scale.

A central objective of this research is to classify the regional climate type. By analyzing long-term spatial and temporal patterns in precipitation and temperature, this study distinguishes localized climatic conditions across the sub-catchments. Such classification is essential not only as a descriptive exercise but also because it lays the foundation for understanding the hydrological behavior of the region. Previous studies have demonstrated that established climate classification methods—including the Emberger diagram, the De Martonne index, and the Bagnouls-Gaussen approach—can effectively delineate climatic regimes in areas with Mediterranean or semi-arid climates. Drawing on these methodologies, the present work refines the climatic characterization of each sub-catchment, thereby enabling a more nuanced interpretation of how climate influences water availability.

In tandem with climate classification, the identification of groundwater recharge periods holds critical importance. Groundwater recharge is directly influenced by the timing and intensity of precipitation relative to evapotranspiration dynamics. By examining the spatial and temporal distribution of the primary climatic variables, this research identifies distinct periods during which optimal conditions for recharge occur. This dual focus—on both climate type and recharge dynamics—addresses significant data gaps and contributes to the broader understanding of the water cycle in water-scarce regions.

Ultimately, the insights derived from this study are expected to enhance predictive hydrological modeling and foster the development of effective water management strategies. By linking detailed climate analysis with groundwater recharge processes, this research advances our understanding of the interplay between climate variability and hydrological responses at the local scale—information that is vital for adapting to future climatic challenges.

3.3 Methodology

3.3.1 Data Sources

Climate information for this study was obtained from the NASA Langley Research Center (LaRC) POWER project, which offers comprehensive and freely accessible climate datasets. This dataset provided monthly data on precipitation and temperature over a 37-year period (1980–2018) for the study region. The available layers include:

- Monthly precipitation sum
- Monthly mean minimum temperature
- Monthly mean maximum temperature

3.3.2 Data Processing

For each month within the study period, a total of 38 data layers (for precipitation, maximum temperature, and minimum temperature) were downloaded. A raster calculator was used to compute the average of these layers to determine the monthly values. Once computed, the resulting rasters were clipped to the study area and reprojected using a warp tool to ensure compatibility with our spatial analysis requirements.

3.3.3 Resolution Enhancement

To improve the spatial resolution of the data, the Kriging interpolation method was applied. Originally, the dataset possessed a resolution corresponding to approximately 21 km^2 per pixel. By plotting a data point for each pixel and then applying Kriging, the resolution was downscaled to 100 m $\times$ 100 m. This enhancement produced detailed maps representing the monthly average precipitation as well as the maximum and minimum temperature distributions across the study area.

3.3.4 Geospatial Analysis

Advanced geospatial tools were employed to extract statistical summaries (e.g., mean, maximum, minimum, and frequency distributions) of the key climatic parameters from the interpolated datasets. These summaries were generated using zonal statistics separately for each sub-catchment within the northern upper Boussellam catchment. This analysis provided a robust basis for subsequent evaluations of:

- Climate type determination
- Evapotranspiration estimates
- Runoff and water balance calculations

3.3.5 Climate Classification

To characterize the climate of the study area, three established methods were applied:

1. **Bagnouls-Gaussen Diagram**
   This method, originally proposed by Gaussen and Bagnouls (1952), illustrates the relationship between monthly precipitation and temperature. In this diagram, a period is classified as arid if the monthly precipitation (P) is less than twice the temperature (T), i.e.,

$$P < 2T.$$

2. **De Martonne Aridity Index**
   The De Martonne aridity index is computed using the ratio of the annual precipitation (P) to the annual mean temperature (T) plus 10 °C. Mathematically, the index is expressed as:

$$I_{DM} = \frac{P}{T + 10}.$$

   This index is widely used due to its simplicity and minimal data requirements.

3. **Emberger Classification**
   The Emberger Index (or Quotient) is particularly useful for classifying climates in Mediterranean and semi-arid regions. It is defined by the formula:

$$Q = \frac{2000 \times P}{M^2 - m^2},$$

   where:

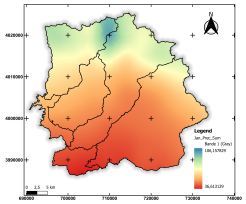
   - P is the annual precipitation,
   - M is the maximum temperature of the warmest month, and
   - m is the minimum temperature of the coldest month.

This comprehensive methodology, combining robust data sources with advanced spatial analysis and climate classification techniques, allows for a detailed evaluation of the climatic patterns and groundwater recharge processes within the study area.

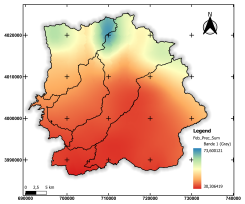
3.4 Results

3.4.1 Precipitation analyses

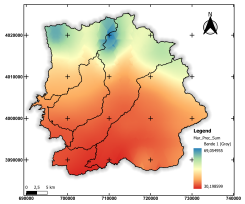
As illustrated in Figures 3.1 and 3.2 and detailed in Table3.1, the analysis of annual precipitation over the period 1980–2018 in the northern segment of the upper Boussellam catchment reveals a distinct spatial gradient.



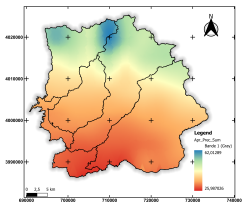
(A) January



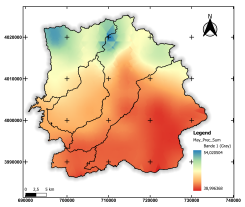
(B) February



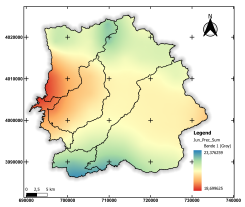
(C) March



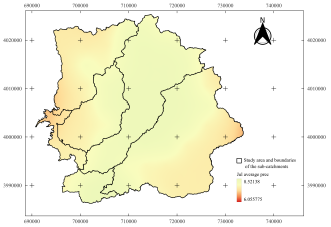
(D) April



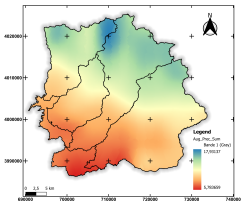
(E) May



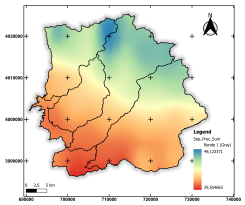
(F) June



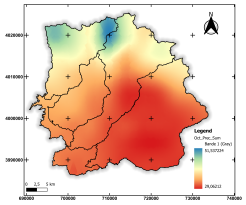
(G) July



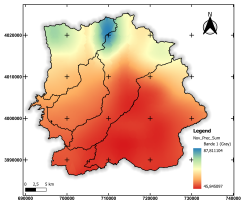
(H) August



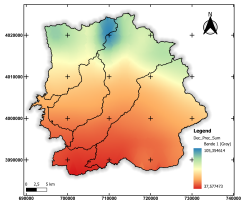
(I) September



(J) October



(K) November



(L) December

FIGURE 3.1: Average monthly precipitation (in mm) for the period 1980–2018. Each subfigure shows the mean precipitation for the corresponding month.

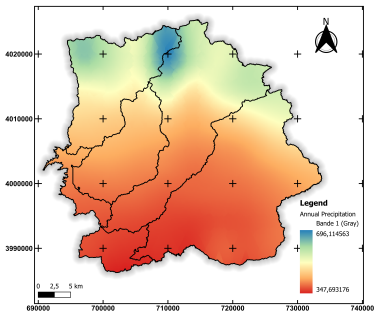


FIGURE 3.2: Annual precipitation (in mm), computed as the sum of the monthly averages over the period 1980–2018.

TABLE 3.1: Precipitation analysis in the study area. Drainage basin precipitation (mm) – monthly averages (Jan–Dec) and annual totals.

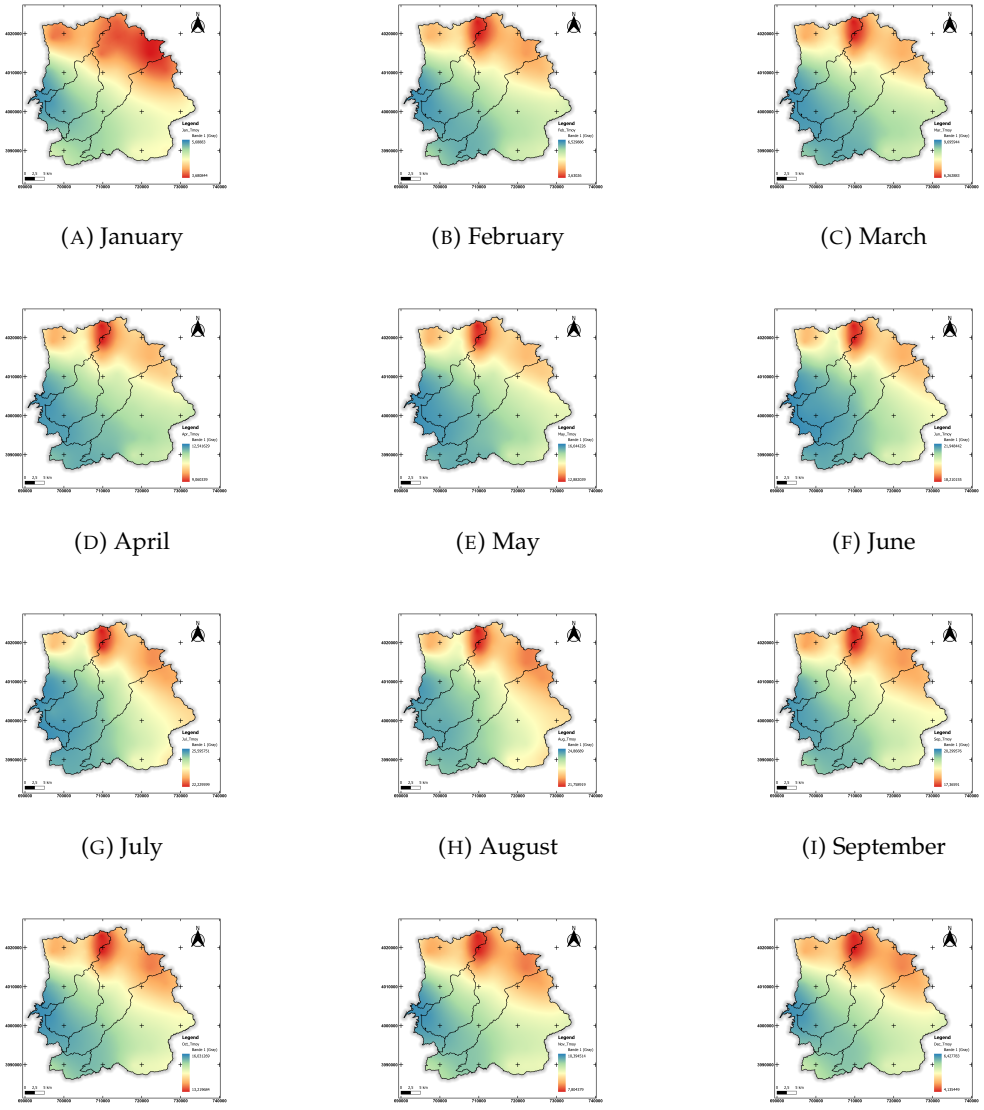
Drainage Basin	Precipitation (mm)	Jan	Feb	Mar	Apr	May	Jun	Jul	Aug	Sep	Oct	Nov	Dec	Annual
Boussellam	Mean	64,3	44,5	45,7	43,7	44,8	21,3	8,3	13,3	41,7	36,4	58,8	68,1	490,8
	Min	42,6	32,8	32,6	29,7	40,6	20,8	7,7	7,5	32,1	29,5	46,8	42,8	372,2
	Max	98,8	70,9	69,0	62,0	54,0	22,5	8,5	17,9	49,1	51,5	87,6	104,1	695,5
	Minority	42,6	32,8	32,6	29,7	40,6	20,8	7,7	7,5	32,1	29,5	46,8	42,8	372,2
	Majority	46,4	33,1	32,9	30,7	41,7	20,9	8,4	7,7	45,5	29,7	47,3	88,9	376,8
Kharoua	Moy	75,4	51,1	52,1	48,5	48,4	20,9	7,7	13,5	41,5	41,9	67,9	77,8	546,5
	Min	58,4	39,4	39,2	35,6	44,2	19,0	7,2	9,2	33,9	35,6	56,0	56,6	434,9
	Max	98,9	71,0	69,1	62,0	54,0	22,5	8,3	17,9	49,1	51,5	87,8	104,2	696,1
	Minority	58,4	39,4	39,2	35,6	44,2	19,0	7,2	9,2	33,9	35,6	56,0	56,6	434,9
	Majority	59,8	40,2	39,5	37,4	45,1	19,3	7,7	11,0	34,8	35,9	66,5	59,4	467,3
Mkhalfa	Moy	55,7	38,2	39,3	37,4	43,9	20,5	8,0	10,6	36,6	34,7	54,9	57,0	436,7
	Min	47,7	34,5	34,4	32,3	42,1	19,5	7,3	7,6	32,4	32,2	50,4	46,8	391,9
	Max	75,5	51,1	54,5	49,6	48,1	21,4	8,4	14,8	44,2	41,2	67,3	79,0	554,5
	Minority	47,7	34,5	34,4	32,3	42,1	19,5	7,3	7,6	32,4	32,2	50,4	46,8	391,9
	Majority	49,6	34,9	35,2	33,6	43,1	20,6	7,5	8,5	32,7	32,7	51,8	49,4	403,1
ouled saber	Moy	51,0	36,9	38,0	35,9	41,3	21,2	8,0	10,8	37,2	31,4	50,3	54,2	416,3
	Min	38,3	31,8	31,2	27,8	39,0	20,3	7,0	6,4	30,9	29,1	45,9	39,7	359,4
	Max	79,9	56,5	56,1	51,4	47,9	23,0	8,5	15,9	46,1	40,1	67,8	84,9	574,7
	Minority	38,3	31,8	31,2	27,8	39,0	20,3	7,0	6,4	30,9	29,1	45,9	39,7	359,4
	Majority	48,0	32,3	36,1	28,2	40,8	20,9	7,6	9,4	33,9	29,9	47,3	40,5	386,1
Northern	Moy	58,8	41,2	42,3	39,9	43,8	21,1	8,0	11,6	38,7	35,0	56,1	61,5	458,0
	Min	37,1	30,6	31,1	27,3	39,0	18,9	7,0	5,9	30,2	29,1	45,9	37,6	351,2
	Max	98,9	71,0	69,1	62,0	54,0	23,2	8,5	17,9	49,1	51,5	87,8	104,2	696,1
	Minority	37,1	30,6	31,1	27,3	39,0	18,9	7,0	5,9	30,2	29,1	45,9	37,6	351,2
	Majority	48,0	32,5	33,3	33,1	40,8	20,9	8,4	9,4	32,7	29,9	48,3	49,6	384,3

The Ain Abassa and Boussellam sub-catchments receive the highest levels of rainfall, with interannual averages of approximately 546 mm and 490 mm, respectively, and peak values reaching around 696 mm and 695 mm. Moving toward the south, precipitation declines; the minimum observed values in these sub-catchments are around 434 mm in Ain Abassa and 372 mm in Boussellam. Further west, the Mkhalfa and Ouled Saber catchments exhibit even lower average annual precipitation, recorded at roughly 436 mm/year and 416 mm/year, respectively. In these areas, the maximum annual values are approximately 554 mm in Mkhalfa and 574 mm in Ouled Saber, with minimum values of about 391 mm and 359 mm correspondingly.

Temporally, December emerges as the wettest month in the northern portion of the catchment, with peak monthly precipitation reaching up to 104 mm in both the Boussellam and Ain Abassa sub-catchments. In stark contrast, July is the driest month across the entire study area, with maximum values as low as 8 mm observed in Boussellam.

3.4.2 Temperature analysis

Figure 3.3 shows the mean monthly temperature (°C) for the period 1980–2018, where each subfigure represents the average temperature for a specific month (January through December).



(A) January (B) February (C) March

(D) April (E) May (F) June

(G) July (H) August (I) September

(J) October (K) November (L) December

FIGURE 3.3: Average monthly temperature (°C) for the period 1980–2018. Each subfigure represents the average temperature for the corresponding month.

Table 3.2 summarizes the mean temperature analysis in the study area, providing monthly and annual averages for each drainage basin.

As depicted in Figure 3 and detailed in Table 3.2, the analysis of the mean temperature data for the period 1980–2018 in the northern sector of the upper Boussellam catchment shows an overall average of approximately 13.5 °C. However, this average conceals notable spatial differences, with temperatures

TABLE 3.2: Mean temperature analysis in the study area. Drainage basin temperature (°C)—monthly averages (Jan–Dec) and annual averages.

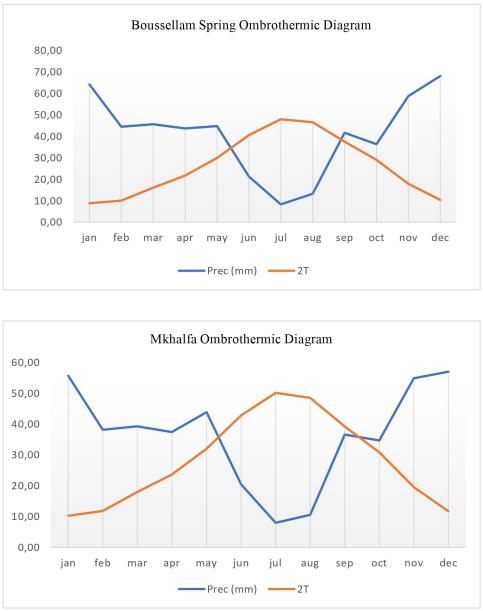
Drainage Basin	T (°C)	Jan	Feb	Mar	Apr	May	Jun	Jul	Aug	Sep	Oct	Nov	Dec	Annual
Boussellam	Mean	4,4	5,0	8,0	10,9	14,9	20,3	24,0	23,3	18,8	14,5	9,0	5,2	13,2
	Min	3,7	3,6	6,3	9,1	12,9	18,2	22,2	21,8	17,4	13,2	7,8	4,1	11,7
	Max	5,4	6,2	9,4	12,3	16,4	21,7	25,4	24,5	20,0	15,7	10,1	6,1	14,4
	Minority	3,7	3,6	6,3	9,1	12,9	18,2	22,2	21,8	17,4	13,2	7,8	4,1	11,7
	Majority	3,7	4,1	7,3	9,6	14,0	19,4	23,1	22,8	18,0	14,1	8,3	4,2	14,3
Kharoua	Mean	4,6	5,1	8,0	10,9	15,0	20,4	24,2	23,5	18,8	14,6	9,0	5,2	13,3
	Min	3,9	3,6	6,3	9,1	12,9	18,2	22,2	21,8	17,4	13,2	7,8	4,2	11,7
	Max	5,6	6,4	9,5	12,4	16,5	21,8	25,5	24,7	20,1	15,9	10,3	6,3	14,6
	Minority	3,9	3,6	6,3	9,1	12,9	18,2	22,2	21,8	17,4	13,2	7,8	4,2	11,7
	Majority	4,0	3,7	6,4	9,6	14,0	18,4	22,4	21,9	18,1	13,3	8,1	4,2	11,8
Mkhalfa	Mean	5,1	5,9	9,0	11,8	16,0	21,4	25,1	24,3	19,6	15,4	9,8	5,9	14,1
	Min	4,2	4,6	7,5	10,4	14,5	19,9	23,8	23,1	18,5	14,2	8,6	4,8	12,9
	Max	5,6	6,4	9,5	12,4	16,5	21,8	25,4	24,6	20,1	15,9	10,3	6,3	14,6
	Minority	4,2	4,6	7,5	10,4	14,5	19,9	23,8	23,1	18,5	14,2	8,6	4,8	12,9
	Majority	4,4	5,4	8,1	11,1	15,4	21,6	25,3	24,1	19,8	14,5	8,8	5,9	13,9
ouled saber	Mean	4,7	5,5	8,5	11,4	15,3	20,6	24,1	23,4	19,1	14,8	9,3	5,5	13,5
	Min	3,8	4,4	7,3	10,2	14,1	19,3	23,0	22,4	18,1	13,8	8,3	4,6	12,5
	Max	5,3	6,2	9,3	12,1	16,2	21,5	25,2	24,4	19,9	15,6	9,9	6,0	14,3
	Minority	3,8	4,4	7,3	10,2	14,1	19,3	23,0	22,4	18,1	13,8	8,3	4,6	12,5
	Majority	4,7	5,4	8,6	11,7	15,2	20,1	23,6	22,5	18,2	14,9	9,3	5,5	13,5
Northern	Mean	4,7	5,4	8,4	11,3	15,3	20,6	24,3	23,6	19,1	14,9	9,3	5,4	13,5
	Min	3,7	3,6	6,3	9,1	12,9	18,2	22,2	21,8	17,4	13,2	7,8	4,1	11,7
	Max	5,6	6,4	9,6	12,4	16,6	21,9	25,5	24,7	20,2	16,0	10,3	6,4	14,6
	Minority	3,7	3,6	6,3	9,1	12,9	18,2	22,2	21,8	17,4	13,2	7,8	4,1	11,7
	Majority	5,2	4,5	8,7	11,6	16,2	21,5	23,9	24,0	18,2	15,6	8,5	5,0	14,3

ranging between 11.7 °C and 14.6 °C. The lowest annual mean of 11.7 °C is observed in the northern sections of the Boussellam Spring and Ain Abassa sub-catchments, while the highest value, 14.6 °C, occurs in the southern area of Ain Abassa, near the Ain Zada dam, as well as in the southern part of the Ouled Saber sub-catchment. Additionally, the average interannual temperatures within the various sub-catchments fluctuate between 13.2 °C and 14.1 °C. In terms of seasonal patterns, January consistently represents the coldest month, whereas July is identified as the warmest across all sub-catchments.

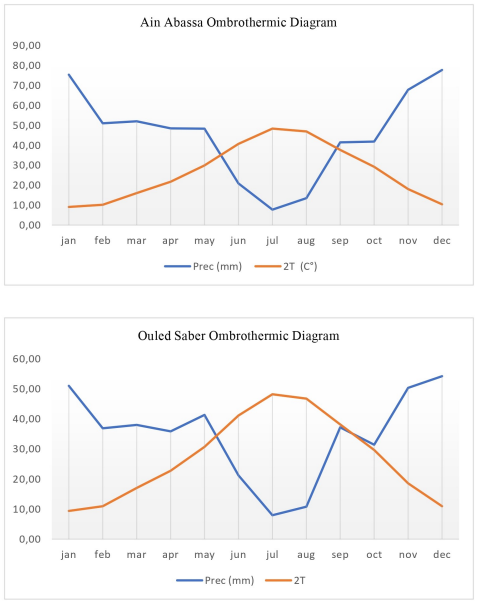
3.4.3 Climate determination

The Bagnouls-Gaussen diagram

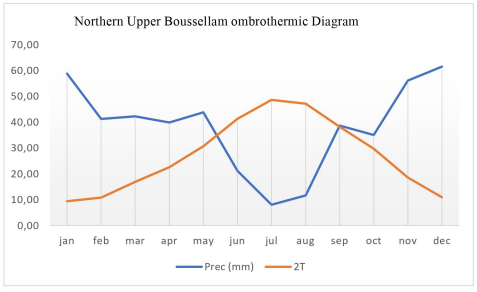
Figure 3.4 displays the Bagnouls–Gaussen diagrams for the northern portion of the Upper Boussellam catchment, clearly delineating periods of relative dryness and wetness. The diagram indicates that the dry season, characterized by notably low precipitation, starts around mid-May and continues until early September. This seasonal pattern is evident across all sub-catchments analyzed in the study, namely Boussellam, Ain Abassa, Ouled Saber, and Mkhalfa. However, there are discernible differences among these sub-regions. In particular, the Ouled Saber and Mkhalfa sub-catchments experience a more prolonged dry period, which could adversely influence water availability, whereas the Boussellam and Ain Abassa sub-catchments register higher rainfall amounts during the wet periods. According to these diagrams, the onset of the rainy season occurs after septembre, guiding our choice of November LULC layers as the starting point for recharge modeling.



(A) Ombrothermic diagrams for Boussellam Spring and Mkhalfa



(B) Ombrothermic diagrams for Ain Abassa (Kharoua) and Ouled Saber



(C) Ombrothermic diagram for the northern Upper Boussellam catchment

FIGURE 3.4: Bagnouls–Gaussen ombrothermic diagrams for the Northern Upper Boussellam Drainage Basins catchments: (a) Boussellam Spring & Mkhalfa, (b) Ain Abassa (Kharoua) & Ouled Saber, (c) overall northern Upper Boussellam.

De Martonne Aridity Index Analysis

Based on the De Martonne aridity index—which categorizes climates into seven distinct classes—the northern section of the upper Boussellam catchment is predominantly semi-arid, with an overall index value of approximately 19.49. In this classification, index values falling within $10 \leq IDM < 20$ denote a semi-arid climate, whereas those in the range $20 \leq IDM < 24$ correspond to a sub-humid climate. Notably, there is variability among the sub-catchments: the Ouled Saber and Mkhalfa sub-catchments exhibit semi-arid conditions with index values of about 17.7 and 18.1 respectively, while the Boussellam Spring and Ain Abassa sub-catchments display sub-humid characteristics, with index values of roughly arround 21 and 23.

Emberger Classification Analysis

To assess the bioclimatic characteristics of the study area, the Emberger classification was employed as shown in Figure 3.5. For each sub-catchment, the maximum temperature of the warmest month was obtained from the July maximum temperature map using a zonal statistics tool. Similarly, the minimum temperature of the coldest month was derived from the June minimum temperature map. These temperature values were then used to calculate the Emberger quotient, Q, which combines thermal extremes and precipitation to aid in climate classification.

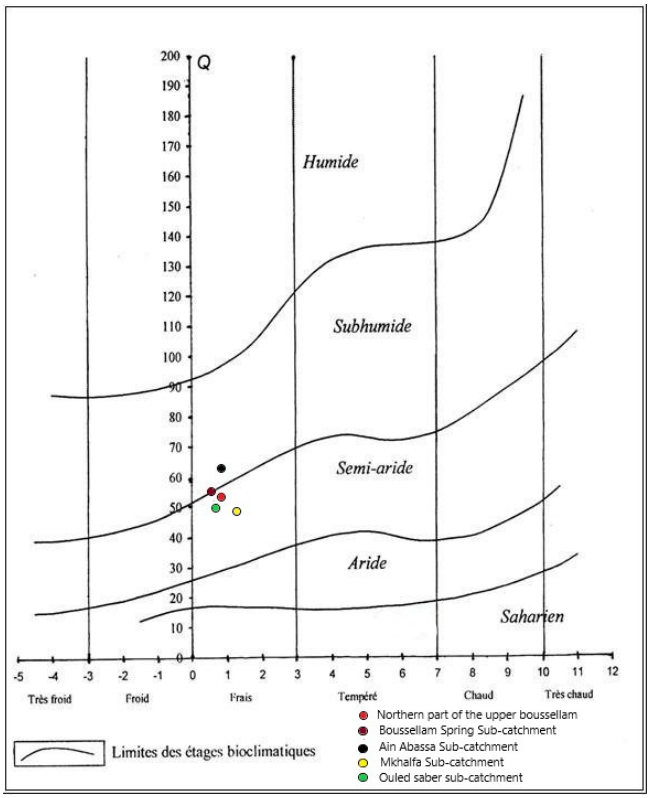


FIGURE 3.5: Position of the Upper Boussellam region on the Emberger (1955) climagram, highlighting its placement within the Mediterranean–semiarid climate zone.

The computed parameters—T_{min} (in Kelvin), T_{max} (in Kelvin), and the corresponding Q values—are presented in Table 3.3 and are also illustrated in Figure 5.

Drainage Basin	Northern	Boussellam Spring	Ain Abassa	Mkhalfa	Ouled Saber
T_{min} (K)	273.8	273.6	273.8	274.2	273.7
T_{max} (K)	304.3	304.0	304.1	305.1	304.2
Q	51.9	55.9	62.5	48.8	47.2

TABLE 3.3: Emberger Classification Results

3.5 Discussion

Over the period 1980–2018, our analysis of precipitation and temperature data in the northern part of the upper Boussellam catchment reveals a distinct spatial gradient and seasonal pattern. The mean annual precipitation is approximately 458 mm/year, while the mean temperature averages around 13.5 °C, with values varying across the catchment. These patterns indicate that, on the whole, the region exhibits a semi-arid climate; however, two of the subcatchments display sub-humid characteristics. This differentiated climate classification was achieved through the combined use of the Bagnouls-Gaussen diagram, De Martonne aridity index, and Emberger classification.

A key outcome of our study is the delineation of distinct dry and wet periods across the sub-catchments. For instance, the analyses of the Bagnouls-Gaussen diagram clearly show that the dry season extends from mid-May to early September, while the wet period—peaking around December—dominates the annual cycle. Such seasonal trends are critical because they directly influence groundwater recharge dynamics. Specifically, recharge is expected to be maximized during the wet period when high precipitation and moderated temperatures favor infiltration.

These insights are instrumental in guiding the timing of field investigations. By establishing that the recharge period occurs during the wet season, this chapter provides a solid basis for scheduling piezometric surveys and hydrochemical sampling. Conducting these analyses during or immediately following the recharge period will ensure that the most representative conditions of groundwater influx are captured.

In summary, the climate classification and seasonality analysis presented here not only enhance our understanding of regional hydrological behavior but also serve as a practical guide for future water resource assessments. The strategic identification of the recharge period is a critical precursor to effective piezometric and hydrochemical analyses in the upper Boussellam catchment.

3.6 Precipitation intensity Mapping

We generated an annual rainfall surface from NASA-POWER data (2.5′ resolution, nearly 21 km^2) by averaging monthly precipitation for 1980–2021, summing to an annual total, and then interpolating via ordinary kriging on a 1 km

$\times$ 1 km grid. As a result, the annual rainfall map (Figure 3.6) exhibits a minimum class threshold of 347 mm yr^{-1} and peaks at 703 mm yr^{-1} in the northern massifs.

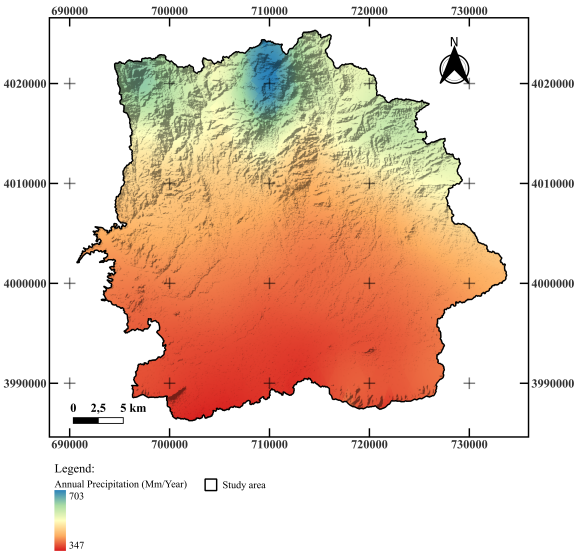


FIGURE 3.6: Annual precipitation intensity in the Northern Upper Boussellam, interpolated via kriging from NASA-POWER data (1980–2021). Values range from <418.20 mm/year (42.54% area coverage) to a maximum of 703 mm/year (2.84% area coverage).

In Chapter 6 this rainfall layer will serve as the principal water-input parameter in our groundwater-recharge potential model, where higher-intensity zones receive greater recharge weighting alongside DEM-derived slope, LULC, lineament density and hydrochemical inputs.

3.7 Conclusion

This study has demonstrated that the northern part of the upper Boussellam catchment exhibits a distinct spatial and temporal variability in key climatic parameters over the period 1980–2018. The detailed analysis of precipitation and temperature data revealed that, although the catchment is predominantly semi-arid, certain sub-catchments display sub-humid conditions. The seasonal patterns identified, particularly the extended dry and pronounced wet periods, have proven essential in determining the period of groundwater recharge.

These findings not only enhance our understanding of the regional climate's impact on hydrological processes but also provide a robust basis for water resource management strategies in a water-scarce environment. Importantly, the clear identification of the optimal recharge period informs the scheduling of field investigations.

In the next chapter, we will leverage these insights by presenting comprehensive hydrochemical analyses and piezometric surveys. This subsequent work will further elucidate the groundwater recharge dynamics and contribute to

an integrated sustainable water management framework for the upper Boussellam catchment.

Chapter 4

Remote Sensing across Landsat 8 OLI/TIRS

4.1 Abstract

The Sétif region, a critical agricultural zone in Algeria, faces increasing water scarcity due to recurrent droughts and evolving land use patterns. In this study, Landsat 8 OLI/TIRS imagery acquired in **November 2022-selected on the basis of a prior climate analysis-**was processed to generate a robust land use/land cover (LULC) map and to support lineament extraction for groundwater recharge potential mapping in the Upper Boussellam basin. Radiometric and atmospheric corrections, combined with spectral indices (NDVI, NDWI) and Principal Component Analysis (PCA), enhanced the discrimination of land cover classes and structural features. A supervised classification of the November scene produced a detailed LULC map, which was integrated with lineament analysis to delineate recharge potential zones. To validate the classification, results were compared with agricultural statistics and seasonal imagery of Landsat 8 imagery acquired in April and July 2019. These seasonal datasets highlighted wheat cultivation—the dominant agricultural practice in the northern basin—and confirmed the reliability of the classification. The integrated approach demonstrates the value of combining LULC mapping, lineament analysis, and ancillary agricultural data to identify groundwater recharge potential zones and to support sustainable water resource management in semi-arid environments.

4.2 Introduction

Groundwater resources are a vital component of water supply in semi-arid regions, where surface water is scarce and highly variable. Effective management of these resources requires accurate identification of recharge potential zones, which depend on both geological structures and land use/land cover (LULC) conditions. Remote sensing and Geographic Information Systems (GIS) provide powerful tools for this purpose, offering synoptic, repeatable, and cost-effective means of monitoring surface characteristics relevant to recharge processes.

In this chapter, we focus on the application of Landsat 8 OLI/TIRS imagery to generate detailed LULC maps and to extract structural lineaments for the

delineation of groundwater recharge potential zones in the Upper Boussellam basin. **Based on the climate analysis presented in the previous chapter, November 2022 imagery was selected as the primary dataset**, as it represents stable post-harvest conditions, minimizing seasonal variability and providing an optimal baseline for recharge modeling. The November scene was subjected to radiometric and atmospheric corrections, and spectral indices such as the Normalized Difference Vegetation Index (NDVI) and Normalized Difference Water Index (NDWI) were derived to enhance land cover discrimination. Principal Component Analysis (PCA) was also applied to improve the detection of geological lineaments. These datasets supported a supervised classification that generated a detailed LULC map, which was subsequently integrated with lineament analysis to delineate recharge potential zones.

To validate the classification and assess its consistency with agricultural practices, the results were compared with statistical data from the Direction des Services Agricoles (DSA, 2019) and with additional Landsat 8 imagery acquired in April and July 2019. These seasonal datasets allowed the detection of wheat cultivation, the dominant agricultural activity in the northern part of the basin, and provided evidence of the capacity of multi-temporal imagery to capture seasonal land use dynamics. While this seasonal analysis is complementary, the primary focus of the study remains the integration of LULC and lineament mapping for groundwater recharge assessment.

Ultimately, the integration of remote sensing, GIS, and ancillary agricultural data underscores the potential of this approach to provide actionable insights for sustainable groundwater management in semi-arid regions facing increasing pressure from irrigation demand and recurrent droughts.

4.3 Methodological Overview and Landsat 8 Data Processing

4.4 Materials and Methods

4.4.1 Selection and Preprocessing of Landsat Imagery

Based on the climatological analysis presented in the previous chapter, November marks the onset of the principal groundwater recharge period in the Upper Boussellam basin. Accordingly, a Landsat 8 OLI/TIRS scene acquired in November 2022 was selected as the primary dataset to characterize land cover conditions at the beginning of infiltration. The imagery was reprojected to the study coordinate reference system (CRS) and subjected to radiometric and atmospheric corrections using the Semi-Automatic Classification Plugin (SCP) (Congedo, 2021). The resulting true-color composite (Figure 4.1) provided a baseline visual reference of the study area prior to spectral transformations and index calculations.

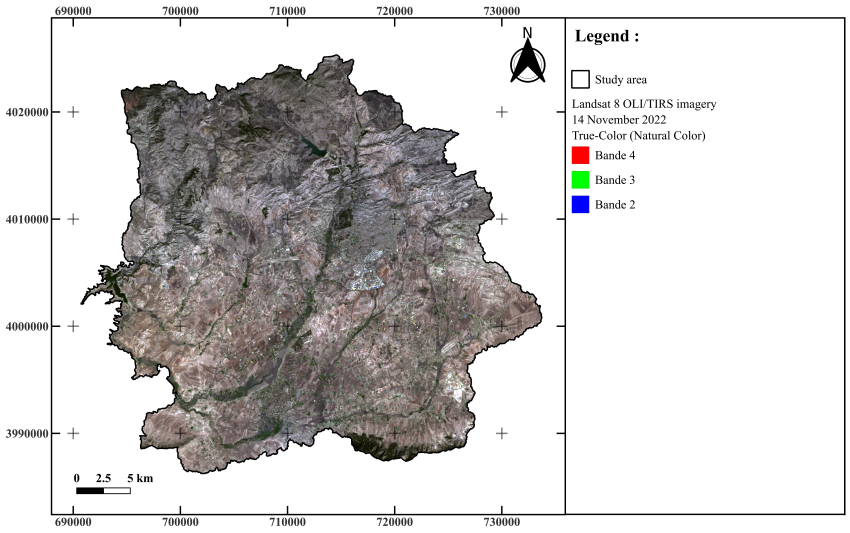


FIGURE 4.1: True color composite of the Northern Upper Boussellam from November 2022 Landsat 8 OLI/TIRS imagery.

4.4.2 Derivation of Spectral Indices and Training Data

Representative training sites were delineated through a combination of visual interpretation and spectral indices. Two indices were particularly useful:

- **Normalized Difference Water Index (NDWI):** applied to isolate open water bodies (Figure 4.2). Bright values correspond to water, providing a complementary layer to vegetation and built-up indices.

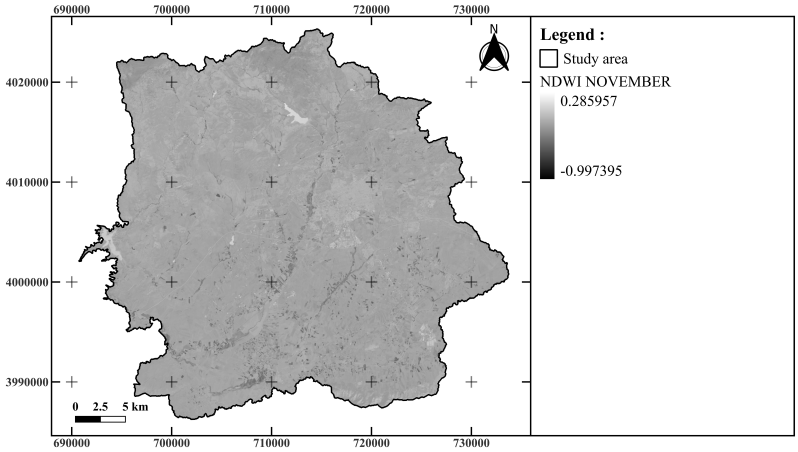


FIGURE 4.2: Normalized Difference Water Index (NDWI) of the Northern Upper Boussellam from November 2022 Landsat 8 OLI/TIRS imagery, where water bodies are represented in white.

– **Normalized Difference Vegetation Index (NDVI):** used to distinguish vegetated from non-vegetated surfaces (Figure 4.3).

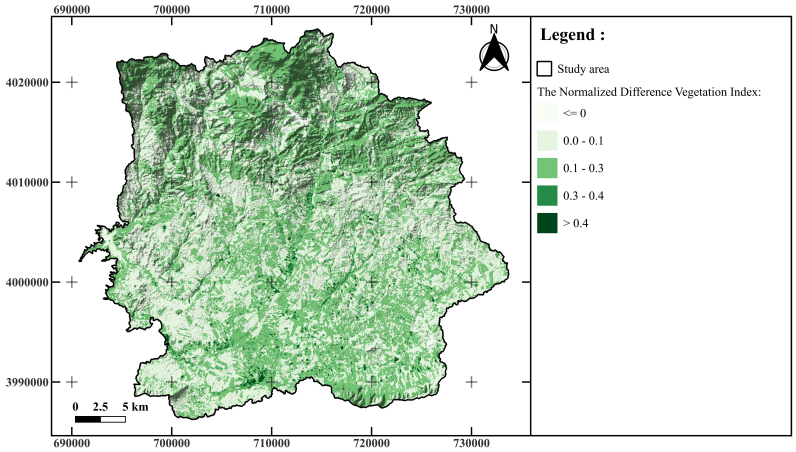


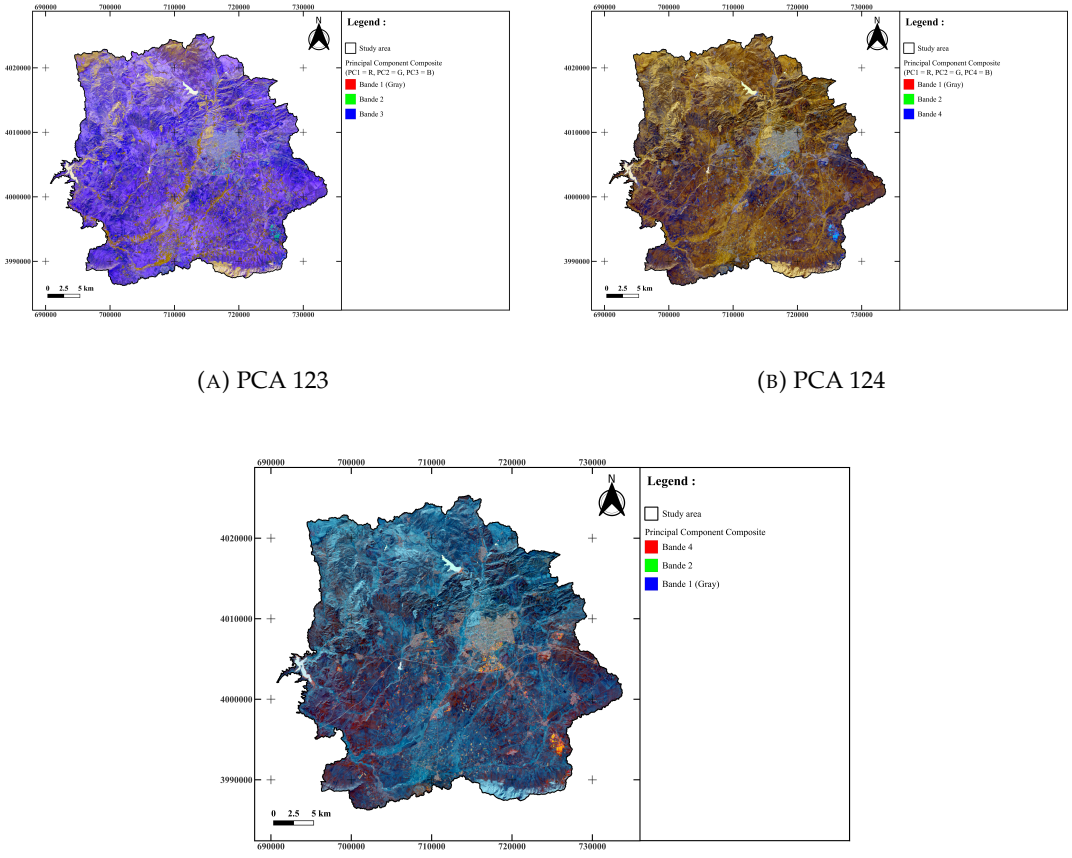
FIGURE 4.3: Normalized Difference Vegetation Index (NDVI) of the Northern Upper Boussellam from November 2022 Landsat 8 OLI/TIRS imagery, classified into five classes.

The NDVI and NDWI layers guided the delineation of training polygons and the definition of spectral classes. These inputs were then used to train a supervised maximum likelihood classifier within SCP.

4.4.3 Extraction of Lineaments via PCA and Manual Digitization

Groundwater occurrence in hard rock terrains is strongly influenced by lineaments, which represent fractures, joints, and faults that enhance secondary porosity and permeability (Prabu & Rajagopalan, 2013; Sander, 2007). To extract these features, a two-step approach was adopted:

1. **Principal Component Analysis (PCA):** PCA was applied to the multispectral dataset to reduce dimensionality and enhance the contrast of linear features. This transformation improved the visibility of geological discontinuities such as faults and fractures (Figure 4.4).



(A) PCA 123

(B) PCA 124

(C) PCA 421

FIGURE 4.4: Principal Component Analysis outputs from Landsat 8 OLI imagery highlighting linear geological features.

2. **Manual Digitization and Integration:** Linear features enhanced by PCA were manually digitized in QGIS to produce a vector layer of lineaments. To ensure completeness, the digitized features were supplemented with structural elements (faults, thrusts) from the regional geological map (see Chapter 1).

4.4.4 Seasonal LULC Mapping with April and July 2019 Imagery

Landsat's long time series and consistent coverage make it particularly valuable for monitoring land surface dynamics. Landsat 8, equipped with the Operational Land Imager (OLI) and the Thermal Infrared Sensor (TIRS), provides high-quality multispectral data that are well suited for advanced remote sensing analyses.

In this study, the April and July 2019 Landsat 8 OLI/TIRS scenes were processed to investigate seasonal variations in land use/land cover (LULC), with a particular focus on wheat cultivation in the northern Upper Boussellam basin. Two composite images were generated to enhance land cover discrimination:

1. **False-Color Composite:** Band 7 (SWIR-2; 2.11–2.29 μm) mapped to red, Band 5 (NIR; 0.85–0.88 μm) to green, and Band 3 (green; 0.53–0.59 μm) to blue.

2. **Color Infrared Composite:** Band 5 (NIR; 0.85–0.88 μm) mapped to red, Band 6 (SWIR-1; 1.57–1.65 μm) to green, and Band 2 (blue; 0.45–0.51 μm) to blue.

These composites accentuate vegetation, soil, and built-up features, thereby improving the delineation of training sites. A supervised maximum likelihood classifier was applied, with training polygons defined from homogeneous regions of known land use. The April image was selected to capture the development phase of winter wheat, which covers more than 85% of cultivated land, under minimal snow and cloud interference in high-altitude areas such as Djebal Megress. The July image complemented this by capturing the senescence and harvest stages, thus reflecting seasonal variability.

To enhance spatial detail, the 15-m panchromatic band was used to pan-sharpen the 30-m multispectral data prior to classification. The two classified rasters were then merged to produce a comprehensive LULC map for 2019. This merging process involved overlaying the April and July classifications and assigning unique codes to each class combination. The resulting attribute table preserved both the original class values and their provenance, enabling detailed comparison with agricultural statistics provided by the Direction des Services Agricoles (DSA). Notably, the DSA data are organized by administrative town boundaries rather than hydrological catchments, reflecting local reporting practices.

This seasonal analysis was not used directly in the groundwater recharge modeling but served as a validation exercise. The comparison with DSA statistics confirmed the reliability of the supervised classification and demonstrated the capacity of multi-temporal Landsat imagery to capture seasonal agricultural dynamics, particularly wheat cultivation. This validation step reinforces the robustness of the November 2022 classification, which forms the basis for groundwater recharge potential mapping in subsequent chapters.

4.5 Results

4.5.1 Land Use/Land Cover (LULC) Classification

The supervised maximum likelihood classification of the November 2022 Landsat 8 OLI/TIRS scene produced six distinct land use/land cover (LULC) classes: Surface Water, Bare Land, Grassland/Meadow, Forest, Healthy Vegetation, and Built-up/Road (Figure 4.5). This classification represents surface conditions at the onset of the recharge season, as identified in the climatological analysis of Chapter 3.

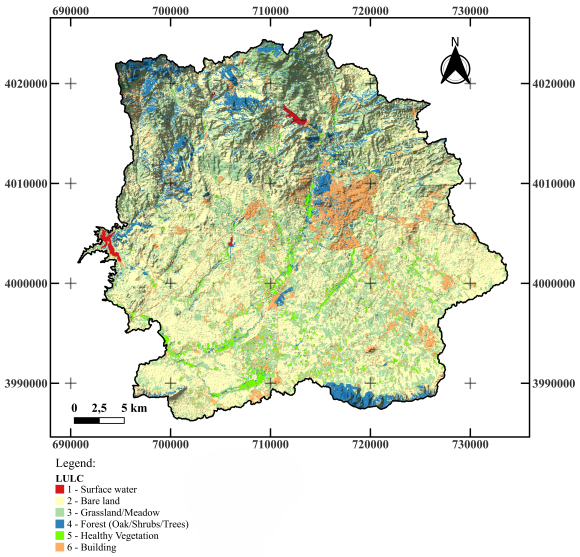


FIGURE 4.5: LULC classification of the Northern Upper Boussellam from November 2022 Landsat 8 OLI/TIRS imagery.

Accuracy of the Classification

Accuracy assessment quantifies the degree of agreement between the classified map and independent reference data. Figure 4.6 shows the false-color composite (bands 7–5–3) of the study area, overlaid with the validation points used to compute the accuracy metrics.

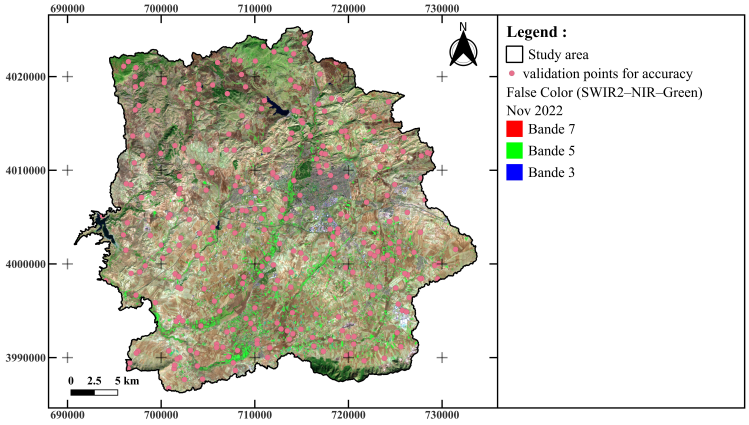


FIGURE 4.6: False color composite (bands 7–5–3) with validation points used for accuracy assessment of the November 2022 classification.

The resulting confusion matrix for the November classification is presented in Table 4.1. From this matrix, the overall accuracy, Kappa coefficient, and class-specific accuracies were derived.

TABLE 4.1: Confusion matrix for November classification

True \ Pred	1	2	3	4	5	6	Total
1	28	1	1	11	0	0	41
2	0	47	2	4	0	3	56
3	0	1	36	4	2	5	48
4	3	2	3	86	0	3	97
5	0	0	1	0	20	0	21
6	1	1	1	3	0	47	53
Total	32	52	44	108	22	58	316

Overall Accuracy (OA) = 83.5%
Kappa coefficient (κ) = 0.796

Producer's Accuracy (PA): 1 = 68.3%, 2 = 83.9%, 3 = 75.0%, 4 = 88.7%, 5 = 95.2%, 6 = 88.7%

User's Accuracy (UA): 1 = 87.5%, 2 = 90.4%, 3 = 81.8%, 4 = 79.6%, 5 = 90.9%, 6 = 81.0%

The November 2022 Landsat 8 classification achieved an overall accuracy of 83.5% with a Kappa coefficient of 0.796.

4.5.2 Lineament Extraction and Density Mapping

Principal Component Analysis (PCA) enhanced the visibility of structural features, allowing the manual digitization of lineaments. As a result High-density zones are concentrated in the central and northeastern sectors (Figure 4.7).

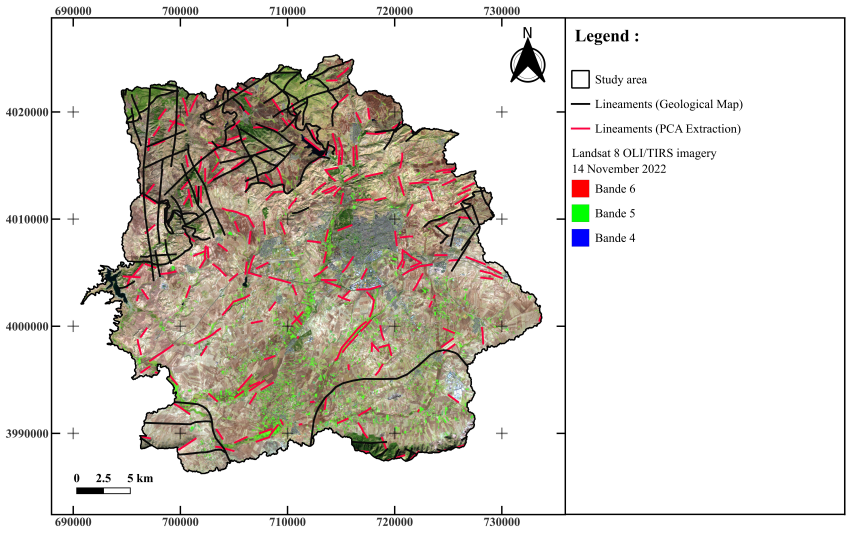


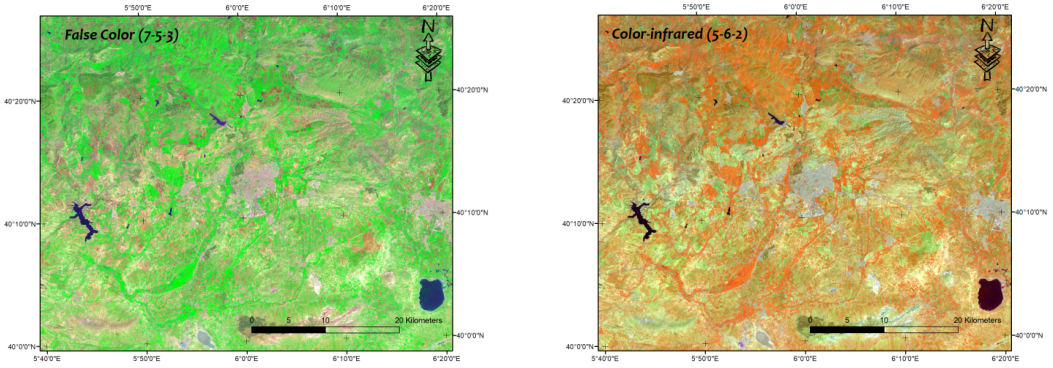
FIGURE 4.7: Lineament density map of the Upper Boussellam basin derived from PCA-enhanced Landsat 8 imagery and geological data.

4.5.3 Validation with Seasonal Imagery and DSA Data

Two additional Landsat 8 OLI/TIRS datasets acquired in April and July 2019 were processed independently to generate high-resolution land use/land cover (LULC) maps. These seasonal classifications were subsequently combined, and the final composite map was compared with empirical data provided by the Direction des Services Agricoles (DSA).

April 2019 Land-Cover Classification

To visualize the Setifian High Hills in April 2019, two pansharpened OLI composites were generated using the 15 m panchromatic band (0.500–0.680 μm). Figure 4.8a presents a false-color composite (bands 7–5–3), while Figure 4.8b shows a color-infrared composite (bands 5–6–2). In Figure 4.8a, crops and healthy vegetation appear in vivid red against soils and built-up areas, whereas Figure 4.8b highlights bare soils in green and vegetation in bright red. Despite the enhanced spectral contrast, herbaceous cover and cultivated crops remained spectrally similar in April, necessitating a supervised classification.



(A) Pansharpened false-color composite (bands 7–5–3)

(B) Pansharpened color-infrared composite (bands 5–6–2)

FIGURE 4.8: Landsat 8 OLI imagery of the Setifian High Hills, April 2019.

Using the pansharpened false-color composite, a maximum-likelihood classifier trained on homogeneous reference sites generated the April land-use map (Figure 4.9), which delineates five classes: surface water, soil, dense forest, vegetation, and healthy vegetation (crops).

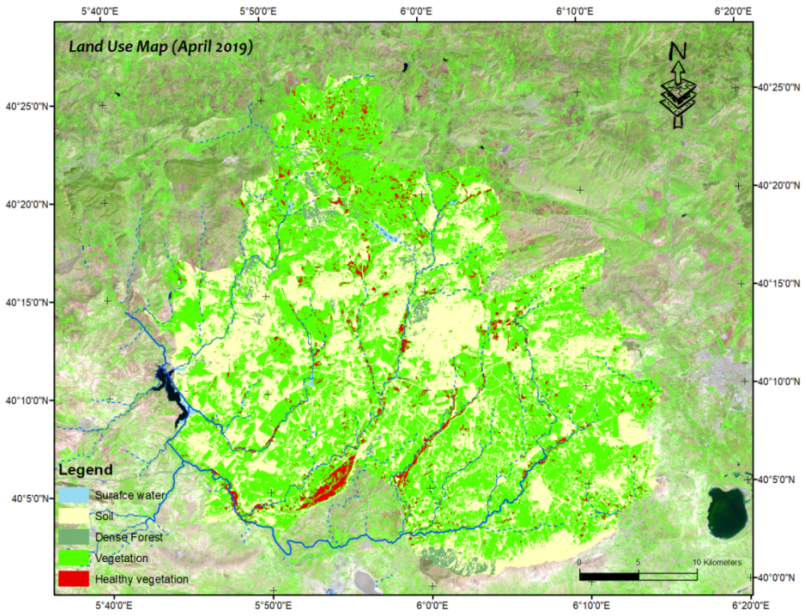
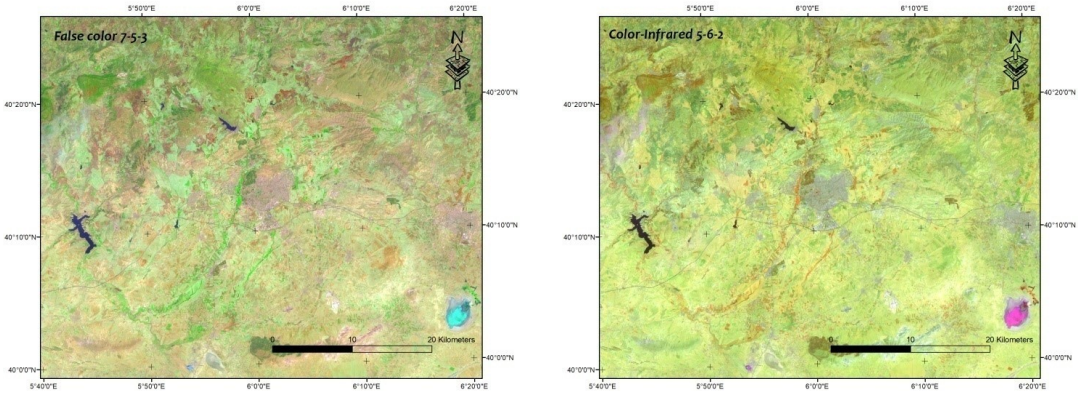


FIGURE 4.9: Supervised land-cover map for April 2019 from the pansharpened false-color composite.

July 2019 Land-Cover Classification

To monitor seasonal change in the Setifian High Hills, two pansharpened OLI composites were generated from the July 2019 Landsat 8 acquisition: a false-color

composite (bands 7–5–3) and a color-infrared composite (bands 5–6–2). Figure 4.10a renders harvested winter wheat in pale green and unharvested crops in yellow, with healthy vegetation in vivid green and soils in brown. In Figure 4.10b, healthy vegetation appears bright red, aiding in the delineation of vegetated patches.



(A) Pansharpened false-color (7–5–3) (B) Pansharpened color-infrared (5–6–2)

FIGURE 4.10: Landsat 8 OLI imagery of the Setifian High Hills, July 2019.

Based on the false-color image, a sixth class—*annual crops*—was introduced to capture post-harvest fields. A maximum-likelihood classifier was trained on homogeneous reference polygons and applied to produce the July land-use map (Figure 4.11).

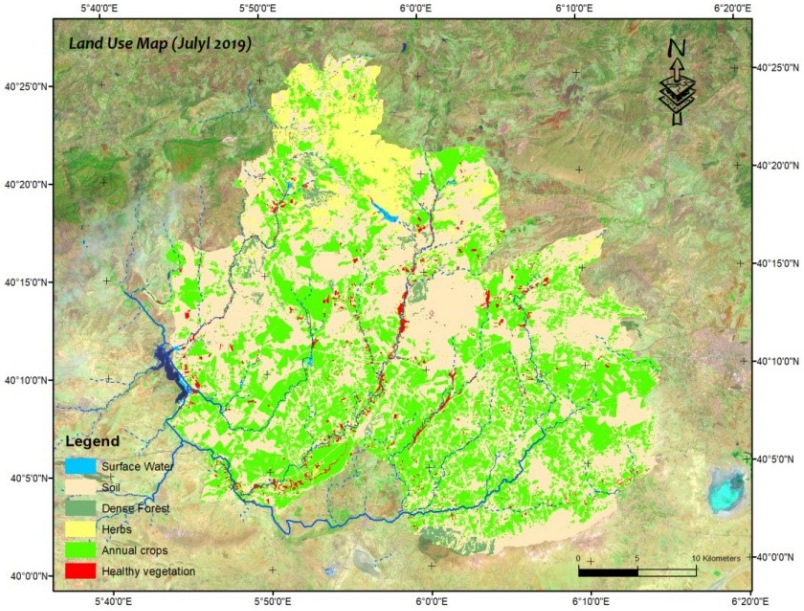


FIGURE 4.11: Supervised land-cover map for July 2019, from maximum-likelihood classification of the pansharpened false-color composite.

The resulting map delineates six classes: surface water, soil, dense forest, herbs, annual crops, and perennial crops.

Combined Land-Use Classification

To capture spatio-temporal dynamics across April and July 2019, the two seasonal maps were merged into a single composite land-use classification (Figure 4.12). This combined map overlays the April classes (surface water, soil, dense forest, vegetation, healthy vegetation) with the July classes (herbs, annual crops, perennial crops) to highlight land-cover transitions before and after harvest.

The merging logic was as follows:

- **Annual crops:** Areas classified as vegetation or trees in April that transitioned into the *annual crops* class in July.
- **Crops:** Includes fodder, legume, and vegetable crops, inferred from cross-date patterns:
  - April soil → July vegetation/annual/healthy vegetation = fodder crops
  - April healthy vegetation → July soil/vegetation = legume crops
  - Persistent healthy vegetation across both dates = vegetable crops
- **Trees:** Dark green tones on the July composite refine the April *dense forest* class into a distinct *trees* category.
- **Soil:** Retained where both April and July classify bare ground, though some April surface water bodies appear as soil in July due to irrigation cycles or seasonal drying.
- **Herbs:** Includes April vegetation that persists in July, plus zones where April surface water converts to July vegetation, healthy vegetation, or annual crops.

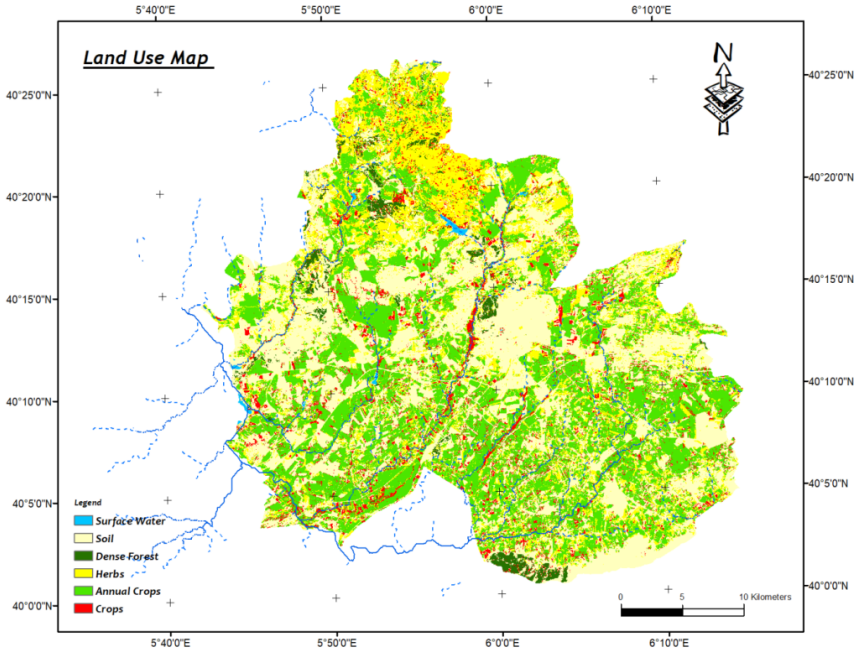


FIGURE 4.12: Combined land-use classification map for April and July 2019. April-derived classes are shown with lighter tints, while July-derived classes (herbs and annual crops) are overlaid in more saturated hues to emphasize seasonal change.

Table 4.2 summarizes the area (in hectares) of each class in the final combined map.

TABLE 4.2: Surface area for each class in the combined land use map.

Class	Value	Count	Ha
Surface water	1	10,909	245.4525
Soil	2	1,819,893	40,947.5925
Dense Forest	3	122,428	2,754.63
Herbs	4	978,326	22,012.335
Annual	5	1,738,491	39,116.0475
Crops	6	264,878	5,959.755

4.5.4 Comparison with DSA Statistics

Table 4.3 compares the area estimates for crop categories derived from Landsat 8 OLI/TIRS imagery with statistics provided by the Direction des Services Agricoles (DSA). For annual crops, the Landsat-derived estimate is 39,116 Ha (86.77% of the total area), while the DSA data subdivides this category into wheat (33,623 Ha, 73.36%), an additional wheat subclass (1,820 Ha, 3.97%), and barley and oat (4,228 Ha, 9.23%). For fodder, vegetable, and legume crops, Landsat data record 5,960 Ha (13.33%), which aligns with the aggregated DSA values for this group.

TABLE 4.3: Comparison between results obtained from Landsat 8 OLI/TIRS and DSA statistics.

Landsat 8 OLI/TIRS			**DSA**		
Category	Ha	% crops	Category	Ha	% crops
Annual crops	39116	86.77	Wheat	33623	73.36
			Wheat	1820	3.97
			Barley and Oat (Annual)	4228	9.23
Fodder, vegetable and legume crops	5960	13.33	Barley and Oat (Fodder)	4997	10.90
			Mais	45	0.10
			Luzerne	106	0.23
			Sorgho	39	0.09
			Soybean	261	0.57
			Vegetable	267	0.58
			Other fodder crops	445	0.97
Total	45076	100	Total	45831	100

4.6 Discussion

4.6.1 LULC Mapping at the Onset of the Recharge Period

Assessing land use and land cover (LULC) at the beginning of the recharge season is essential for understanding how surface conditions influence infiltration dynamics. The November 2022 classification achieved an overall accuracy of 83.5% with a Kappa coefficient of 0.796, indicating substantial agreement beyond chance. Class-specific accuracies revealed that Forest, Built-up/Road, Healthy Vegetation, and Bare Land were mapped with high reliability (PA and UA generally above 80%), while Surface Water showed lower producer's accuracy (68.3%) due to confusion with Forest. Grassland/Meadow also exhibited moderate confusion with adjacent classes, consistent with spectral overlap during November. Notably, Healthy Vegetation achieved the highest accuracies (PA = 95.2%, UA = 90.9%), reflecting strong spectral separability. These results are comparable to accuracy benchmarks reported in similar semi-arid LULC studies, confirming the robustness of the classification.

From a hydrogeological perspective, vegetated areas (forests, crops) enhance infiltration through root penetration and improved soil permeability, while built-up zones and bare land restrict infiltration and favor runoff. Grasslands and meadows occupy an intermediate position, offering moderate infiltration potential. The spatial distribution of these classes therefore exerts a direct control on recharge variability across the basin.

4.6.2 Lineament Density and Hydrogeological Implications

Lineament density analysis highlights the structural controls on groundwater infiltration. High-density zones, concentrated in the central and northeastern sectors, align with known fault and fracture systems and correspond to areas of enhanced secondary permeability. These structural corridors act as preferential pathways for subsurface flow, particularly when intersecting permeable land-cover classes. Conversely, regions of low lineament density, often

associated with massive bedrock or thick soil cover, are characterized by reduced recharge potential. This interpretation is consistent with previous findings that groundwater occurrence in hard-rock terrains is largely controlled by secondary porosity associated with fractures, joints, and faults (Prabu & Rajagopalan, 2013; Sander, 2007).

4.6.3 Seasonal Dynamics and Crop Phenology

The use of multi-temporal Landsat 8 imagery proved essential for resolving ambiguities inherent in single-date classifications. April imagery captured early vegetative growth, while July imagery highlighted senescence and harvest stages. By comparing spectral responses across these dates, the merged LULC product effectively distinguished annual crops from persistent rangeland vegetation and forested patches. Wheat dominated the annual-crops class in July, accounting for more than 65% of its area. This estimate closely matched the Directorate of Statistical Agriculture's regional reports (±3% discrepancy), underscoring both the agronomic importance of wheat and the spectral consistency of its growth stages. Minor differences in area and percentage are attributable to sensor resolution constraints and the temporal offset between satellite overpasses and ground surveys.

4.6.4 Validation with DSA Statistics

The comparison between Landsat-derived estimates and DSA statistics demonstrated strong correspondence. Annual crops accounted for 39,116 Ha (86.77%) in the Landsat classification, compared with 33,623 Ha of wheat, 1,820 Ha of additional wheat subclasses, and 4,228 Ha of barley and oat reported by the DSA. Similarly, fodder, vegetable, and legume crops covered 5,960 Ha (13.33%) in the Landsat data, aligning closely with aggregated DSA values. Minor discrepancies can be explained by differences in classification criteria, sensor resolution, and the mismatch between administrative reporting units and hydrological catchments. Overall, this agreement validates the supervised classification approach and supports the efficacy of remote sensing as a reliable tool for agricultural monitoring.

4.6.5 Integrated Framework for Recharge Assessment

Beyond crop mapping, the integration of Landsat-derived LULC maps with geological lineament density, slope maps from DEMs, and hydrological datasets establishes a multi-criteria framework for delineating groundwater recharge potential zones. Recharge processes are jointly controlled by surface land use and subsurface geological structures, and their combined analysis enhances interpretive accuracy. This integrated methodology not only improves the precision of groundwater resource assessments but also provides critical insights for sustainable water management in semi-arid regions.

4.7 Conclusion

This chapter demonstrated the effectiveness of integrating Landsat 8 OLI/TIRS multispectral imagery with GIS-based analysis to generate detailed land use/land cover (LULC) maps and extract structural lineaments in the Upper Boussellam basin. The November 2022 scene, selected on the basis of climatological analysis, provided a reliable representation of surface conditions at the onset of the recharge season. Through radiometric and atmospheric corrections, spectral index derivation (NDVI, NDWI), and supervised maximum likelihood classification, a high-fidelity LULC map was produced and combined with PCA-derived lineament density mapping. Together, these datasets form the foundation for delineating groundwater recharge potential zones.

Validation using April and July 2019 imagery, supported by Direction des Services Agricoles (DSA) statistics, confirmed the robustness of the classification and its ability to capture wheat cultivation dynamics—the dominant agricultural practice in the northern basin. While not directly applied in recharge modeling, this seasonal analysis reinforced the reliability of the November classification and highlighted the value of multi-temporal imagery for agricultural monitoring in semi-arid regions.

When integrated with ancillary datasets such as DEM-derived slope and hydrological layers, the LULC and lineament maps provide a powerful spatial input for a multi-criteria framework to delineate recharge potential zones. High-density structural corridors intersecting permeable land-cover classes mark preferential recharge pathways, whereas low-density, massive-rock areas exhibit limited infiltration.

Overall, the integrated remote-sensing workflow developed in this chapter offers a scientifically rigorous and scalable approach for both land-cover characterization and groundwater recharge assessment. It establishes a robust basis for the recharge potential modeling presented in the following chapter and contributes to the broader goal of sustainable groundwater management in semi-arid regions. Future refinements—such as incorporating higher-resolution sensors, additional phenological dates, and dynamic hydrological modeling—could further enhance the precision of recharge-zone delineation.

Chapter 5

Hydrochemistry

5.1 Abstract

This study undertook an extensive hydrogeological investigation to elucidate the complexities of the groundwater system in the northern part of the Upper Boussellam Catchment. In the initial phase, piezometric measurements were acquired from 120 boreholes distributed throughout the region. These measurements, obtained following the wet period in March 2023, provided critical data on hydraulic head—a key determinant of groundwater flow direction and velocity. The piezometric data were subsequently plotted using the Quantum Geographic Information System (QGIS) and interpolated with the Thin Plate Spline (TPS) method to generate a continuous surface representing the hydraulic head across the study area. This piezometric map serves as an essential tool for visualizing groundwater flow patterns and identifying potential recharge and discharge zones.

In addition to piezometric data, water samples were collected from 44 boreholes for hydrochemical analysis. This analysis aimed to assess groundwater quality by examining its chemical constituents, thereby revealing important insights into geochemical processes occurring within the aquifer and identifying potential sources of contamination.

Furthermore, geological data were incorporated to evaluate the influence of different rock types on water chemistry. Geological maps provided crucial information on the spatial distribution and nature of rocks and sediments in the area, which significantly affect water–rock interactions and, consequently, the chemical composition of groundwater.

In summary, this study integrates piezometric measurements, hydrochemical analyses, and geological information to provide a comprehensive understanding of both the quantity and quality aspects of the groundwater system. Each component contributes critically to a holistic interpretation, thereby enabling informed decision-making for sustainable groundwater resource management.

5.2 Introduction

Groundwater, an indispensable resource for sustaining life and supporting socio-economic development, is increasingly under pressure due to human activities and climate change. A thorough understanding of the subsurface

hydrogeological characteristics of groundwater systems is essential for effective water resource management. This chapter focuses on the northern part of the upper Boussellam catchment, employing a comprehensive piezometric survey alongside extensive hydrochemical analyses to elucidate its subsurface hydrogeological dynamics.

The piezometric survey involved measurements across 120 strategically located boreholes, yielding valuable insights into the maximum extent and hydraulic head of the groundwater body. Additionally, hydrochemical analyses were performed on samples from 39 distinct locations to quantify the concentrations of seven key ions. The data obtained from these investigations were subsequently utilized to construct geospatial maps using the Inverse Distance Weighting (IDW) method in QGIS. This integrated approach highlights the methodology employed, the results obtained, and their significant implications for water resource management, environmental stewardship, and public health.

Understanding the hydrochemistry of groundwater is critical for assessing its suitability for various applications, such as domestic use and irrigation. Regular monitoring and detailed analysis of groundwater hydrochemistry are essential for maintaining its quality (Kumar et al., 2014). In regions with intensive industrial activities, such as the eastern Chinese Loess Plateau, anthropogenic inputs can significantly exacerbate the pollution of certain elements, thereby compromising water security and intensifying water shortages (Zhang et al., 2021).

The hydrogeochemical conditions of groundwater—including the types and distribution of freshwater—are fundamental for maintaining water quality and security. These conditions are influenced by factors such as weathering processes, anthropogenic inputs, and seawater intrusion. Comprehensive studies conducted arround the world underscore the importance of regular hydrochemical monitoring for effective water resource management (**Zhang2021**; Davraz & Batur, 2021; Yao et al., 2021).

Investigating the chemical composition and quality of groundwater, as well as the controlling factors, is pivotal for understanding the underlying processes governing groundwater dynamics. This is crucial for the scientific utilization and sustainable management of groundwater resources (Yuan et al., 2022). Examining groundwater's hydrochemical characteristics directly reflects its environmental quality and underpins the evaluation of its overall suitability.

By studying the interactions between water, rocks, and other constituents in the environment, we can identify potential pollution sources and guide the development of sustainable groundwater management strategies. This knowledge is fundamental for establishing effective measures to prevent or mitigate groundwater contamination and to ensure its availability for future generations.

5.3 Methodology

The primary objective of this chapter was to comprehensively characterize the subsurface hydrogeological properties of the northern part of the upper Boussellam catchment. To achieve this, we employed a dual approach consisting of

a piezometric survey and a hydrochemical analysis.

5.3.1 Piezometric Survey

A piezometric survey was conducted across 120 strategically located boreholes throughout the region. Measurements were taken in March 2023, immediately following the wet period, when the groundwater system is expected to be at its maximum extent. Precise geographical coordinates were recorded using Global Positioning System (GPS) technology, and the water table depth in each borehole was measured with a water level logger. The collected data were plotted using the Quantum Geographic Information System (QGIS) and interpolated via the Thin Plate Spline (TPS) method to create a continuous surface representing the piezometric head across the study area.

5.3.2 Total Dissolved Solids (TDS) Distribution

As shown in Figure 5.1, the spatial distribution of Total Dissolved Solids (TDS) exhibits a clear north–south gradient that mirrors the piezometric surface and inferred groundwater flow from upstream (north) to downstream (south). Out of more than 120 inventoried boreholes, 44 were sampled to ensure spatial representativeness across the basin and to capture the principal hydrogeological units.

TDS values are generally low in the northern upstream sector, coinciding with higher hydraulic heads and recharge zones. In these areas, shorter groundwater residence times and limited water–rock interaction constrain solute accumulation. Progressing southward, TDS increases systematically toward the downgradient sectors, where lower hydraulic heads, longer flow paths, and increased residence times favor solute enrichment. This pattern is consistent with advective transport along the regional gradient, cumulative dissolution of lithologies encountered along the flow path, and possible concentration effects associated with evapotranspiration in discharge areas.

Local departures from this overall trend are present and will be examined in the hydrochemistry analysis. Potential causes include heterogeneity in aquifer lithology, mixing with deeper or perched units, and anthropogenic inputs (point-source contamination). These anomalies are valuable diagnostic points for interpreting hydrochemical processes beyond purely physical flow control.

In summary, the TDS distribution corroborates the piezometric interpretation: low TDS in northern recharge zones and progressively higher TDS toward southern discharge areas. This alignment between chemistry and hydraulics strengthens the conceptual model of basin-scale flow from north (upstream) to south (downstream) and provides targeted locations for detailed geochemical investigation.

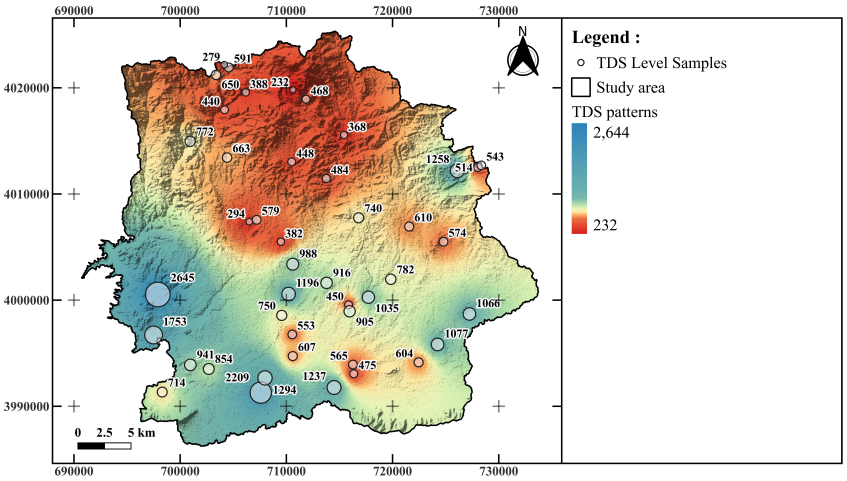


FIGURE 5.1: Spatial distribution of Total Dissolved Solids (TDS) across the basin based on 44 sampled boreholes, showing low TDS in northern recharge zones and higher TDS in southern downgradient sectors.

5.3.3 Hydrochemical Analysis

Water samples were collected from 39 boreholes for detailed hydrochemical analysis. These samples were analyzed in the laboratory to quantify the concentrations of seven key ions: calcium (Ca^{2+}), magnesium (Mg^{2+}), sodium (Na^{+}), potassium (K^{+}), sulfate (SO_4^{2-}), bicarbonate (HCO_3^{-}), and chloride (Cl^{-}). Geospatial maps for each ion were generated using the Inverse Distance Weighting (IDW) method in QGIS, thereby visualizing their spatial distribution and variation across the catchment.

5.3.4 Data Integration and Statistical Analysis

To elucidate the geochemical processes within the groundwater system, we applied statistical analyses such as correlation matrices and linear regression to examine relationships between ion concentrations. Furthermore, water chemistry was visualized using the Piper, Stabler, and Schoeller-Berkaloff diagrams, which facilitated the classification of water types and provided insights into geochemical interactions. Additionally, ionic ratios were calculated to quantify the relative abundance of various ions, and the Riverside and Wilcox diagrams were used to assess water quality for irrigation purposes.

5.3.5 Implications

This integrated methodological framework, combining piezometric measurements, geospatial mapping, and detailed hydrochemical analyses, provides

a comprehensive understanding of both groundwater dynamics and quality. The resulting insights form the basis for informed water resource management, environmental stewardship, and public health initiatives.

5.4 Results and Discussion

5.4.1 Piezometric Survey Results

We have collected and analyzed data from various sources to understand the groundwater system in our area of interest. In this chapter, we present four key images that illustrate the main aspects of our investigation.

Figure Descriptions

As shown in Figure 5.2, the spatial distribution of sampling points ensures full coverage of the aquifer domain for both piezometric and hydrochemical datasets. **Figure** 5.2 is a Google Hybrid map displaying the 120 sampling points used for constructing the piezometric map along with the 39 sampling points used for hydrochemical analysis. These points were carefully selected to cover the entire study area and provide a comprehensive view of the groundwater system.

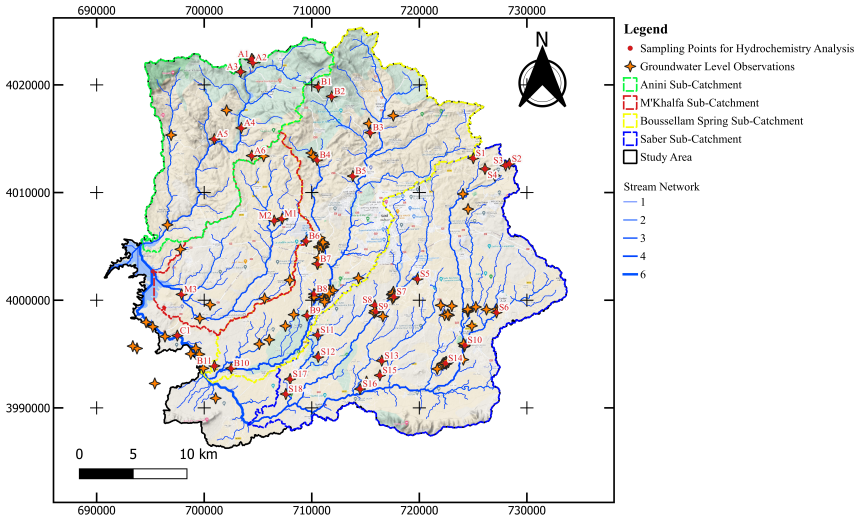


FIGURE 5.2: Google Hybrid map displaying the 120 sampling points used for constructing the piezometric map along with the 39 sampling points used for hydrochemical analysis.

Figure 5.3, overlaying the 39 hydrochemical sampling points on the geological map highlights how different geological units may influence groundwater chemistry.

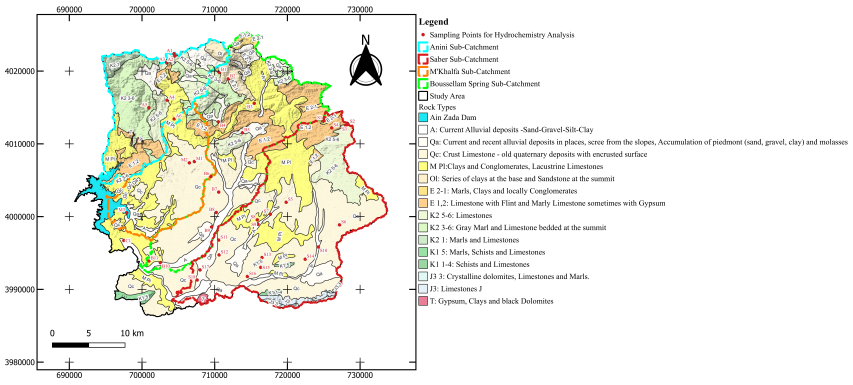


FIGURE 5.3: Geological map showing the 39 sampling points used for hydrochemical analysis.

As shown in Figure 5.4, the piezometric contours on the Google Hybrid basemap delineate lines of equal hydraulic head, critical for understanding aquifer pressure distribution and flow direction.

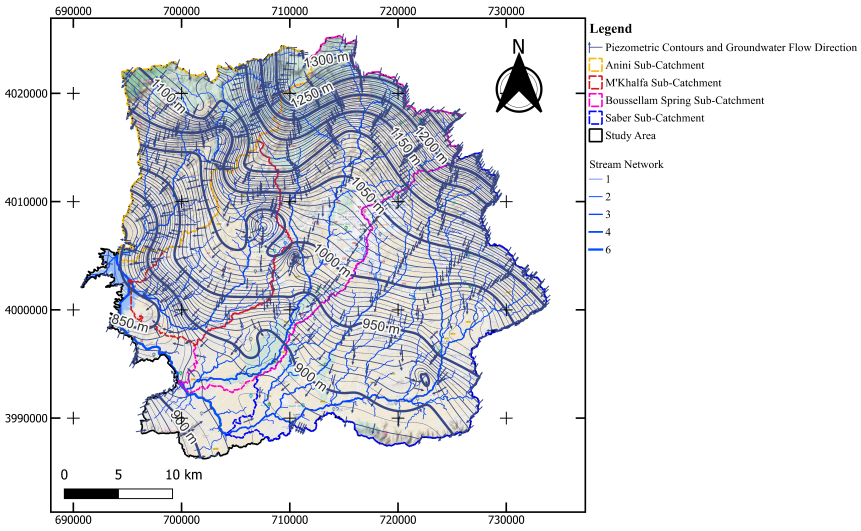


FIGURE 5.4: Google Hybrid map illustrating the piezometric contours.

As shown in Figure 5.5, overlaying piezometric contours on the geological map highlights how surface features and lithologies control groundwater flow.

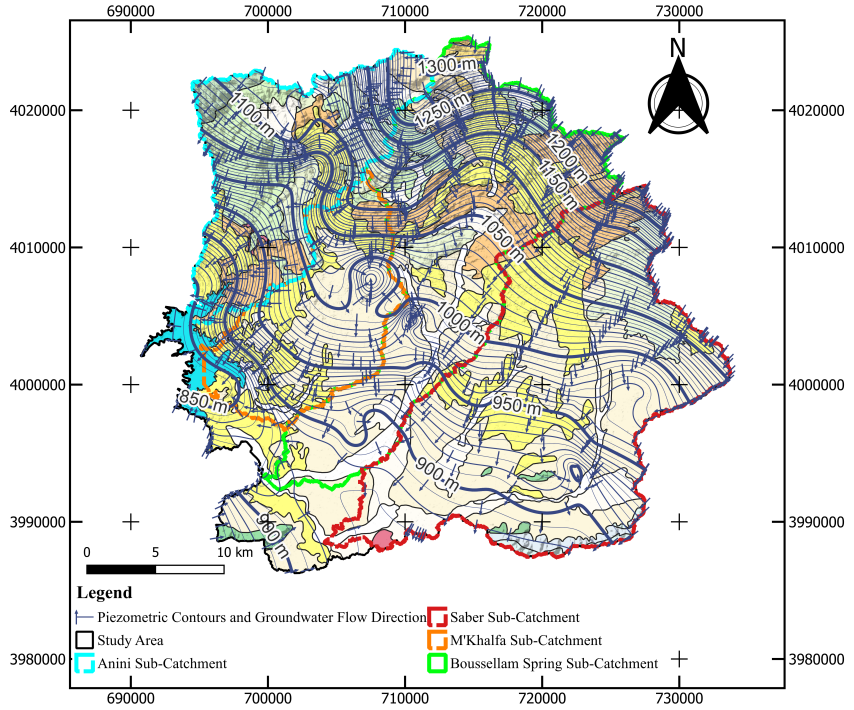


FIGURE 5.5: Geological map displaying piezometric contours.

5.4.2 Piezometric Map Analysis

The piezometric map, constructed from measurements taken from 120 boreholes following the wet period in February 2023, provides a visual representation of the hydraulic head distribution across the study area. It features piezometric contours—lines of equal hydraulic head—which are instrumental for assessing the aquifer's pressure distribution and predicting groundwater flow directions. Arrows on the map indicate the actual direction of flow, offering a comprehensive view of groundwater dynamics.

Overlaying the piezometric contours on both topographic and geological maps further enhances our understanding of how surface features and geological units influence groundwater movement and storage. The topographic context, including hills, valleys, and slopes, is critical for visualizing the relationship between surface morphology and subsurface flow, while the geological maps reveal how different lithologies may control the hydraulic properties of the aquifer.

The maps also highlight catchment boundaries that delineate areas where all precipitation and surface water converge to a common outlet. These boundaries are essential for identifying potential recharge zones where surface water is likely to infiltrate into the groundwater system.

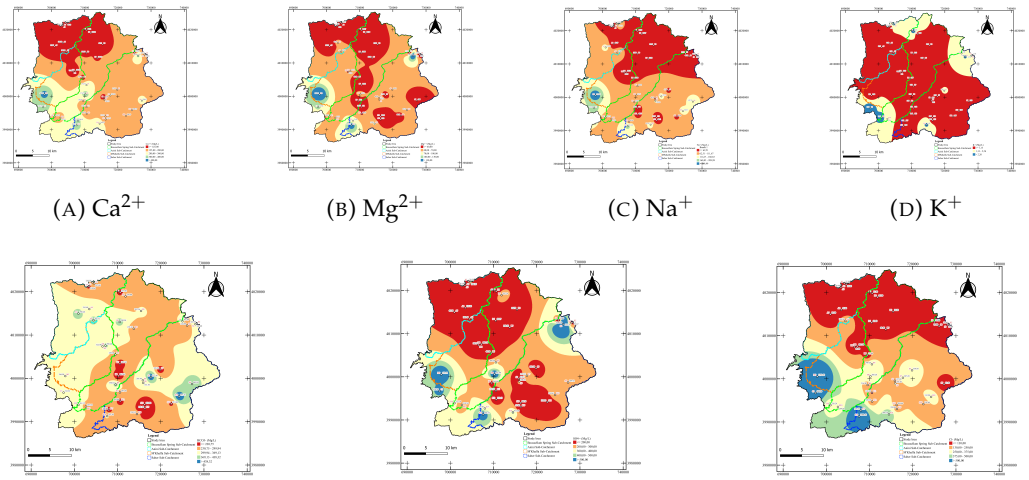
Furthermore, areas where the piezometric contours converge indicate a steeper hydraulic gradient, suggesting a higher velocity of groundwater flow. Such regions, often recognized as groundwater divides or ridges, are prominently

observed in the northern part of the study area and within the Anini sub-catchment. In contrast, regions where the contours diverge—indicating a flatter hydraulic gradient—are associated with slower groundwater movement. These groundwater troughs, where water from adjacent basins converges, are evident in the Boussellam and Saber sub-catchments, with divergence becoming more pronounced in the Mkhalfa area near the 1000 m contour, likely under the influence of high pumping rates and the proximity of a main stream with a Strahler order 6.

Overall, the integration of these maps provides a robust framework for assessing groundwater dynamics and the interplay between geologic, topographic, and hydrological factors in the study area.

5.4.3 Hydrochemical Analysis Results

In Figure 5.6, we present seven IDW-interpolated concentration maps—one for each major ion (Ca^{2+}, Mg^{2+}, Na^{+}, K^{+}, HCO_3^{-}, SO_4^{2-}, Cl^{-})—generated in QGIS from 39 hydrochemical sampling points. Each panel (a–g) illustrates the spatial distribution and concentration gradients of the corresponding ion across the catchment, providing a clear visual framework for subsequent hydrochemical analysis.



(A) Ca^{2+} (B) Mg^{2+} (C) Na^{+} (D) K^{+}

(E) HCO_3^{-} (F) SO_4^{2-} (G) Cl^{-}

FIGURE 5.6: Spatial distribution of major ions (mg/L) interpolated via IDW in QGIS: (a) Ca^{2+}, (b) Mg^{2+}, (c) Na^{+}, (d) K^{+}, (e) HCO_3^{-}, (f) SO_4^{2-}, (g) Cl^{-}.

Calcium (Ca^{2+}) Distribution

Calcium (Ca^{2+}) is a prevalent cation in groundwater and plays a crucial role in maintaining its chemical balance. As depicted in Figure 5.6a, the Ca^{2+} concentration map reveals a distinct spatial pattern across the study area. In the higher-altitude regions—particularly around the mountainous terrains of Djebel Megress and Djebal Anini, as well as the elevated zones of the Mkhalfa sub-catchment—the concentrations of Ca^{2+} are relatively lower. This is likely

attributable to the unique geochemical characteristics of these areas, which are influenced by lithology, weathering processes, and the chemistry of local precipitation.

As groundwater flows from these high-altitude zones toward the main stream (characterized by a Strahler order of 6), there is a noticeable increase in Ca^{2+} concentrations. The highest values are observed in the vicinity of the main stream, suggesting a significant influence of fluvial processes and groundwater-surface water interactions on the geochemical composition. This trend aligns with recharge potential as indicated by the recharge map.

Magnesium (Mg^{2+}) Distribution

The spatial distribution of magnesium ions (Mg^{2+}) exhibits a pattern similar to that of calcium. As shown in Figure 5.6b, the elevated regions around Djbel Megress and Djebal Anini demonstrate relatively lower concentrations of Mg^{2+}. Moving from these high-altitude areas toward the main stream (again, with a Strahler order of 6) along the direction of groundwater flow, there is a discernible increase in Mg^{2+} concentrations. The peak Mg^{2+} values occur near the main stream, further indicating the impact of fluvial processes and interactions between groundwater and surface water on the hydrochemical characteristics of the aquifer.

Sodium (Na^{+}) Distribution

The spatial distribution of sodium ions (Na^{+}) in our study area exhibits a distinct pattern. As shown in Figure 5.6c the higher regions of the fourth sub-catchment, Na^{+} concentrations are relatively low. As groundwater flows towards lower elevations, there is a noticeable increase in Na^{+} concentrations until the vicinity of the main stream is reached, where peak values are observed. The influence of the Quaternary formation—characterized by recent alluvial deposits around perennial rivers—is evident, with sampling points within this formation showcasing elevated Na^{+} levels. In addition, sampling point A2, located in the northern region, displays higher Na^{+} concentrations, which may be attributed to local agricultural practices and the use of road salt in areas subject to snow and low temperatures.

Potassium (K^{+}) Distribution

The spatial distribution of potassium ions (K^{+}) in the study area follows a unique pattern that does not necessarily parallel the groundwater flow direction as shown in Figure 5.6d. Overall, K^{+} concentrations are low (not exceeding 3.24 mg/L) across the study area. However, elevated values are observed in localized areas near mountainous regions—notably around Djebal Anini, Djebal Megress, and Djbel Mnaguer in the north, as well as near Djebal Youssef and Djebal Ardim in the south. Elsewhere, K^{+} is present only in trace amounts (generally below 1 mg/L), with the exception of sampling point S5 in the upper Saber sub-catchment, where a concentration of 1.36 mg/L was recorded.

Bicarbonate (HCO_3^-) Distribution

The bicarbonate ion (HCO_3^-) concentration map Figure 5.6e reveals a dynamic hydrogeochemical pattern with concentrations ranging from 161.04 mg/L to 512.40 mg/L. In the higher areas of Boussellam Spring, Anini, Mkhalfa, and the Saber sub-catchment, HCO_3^- concentrations typically range between 200 and 341.60 mg/L. As groundwater flows toward lower elevations, HCO_3^- levels generally increase, although certain sampling points in the central portion of the study area exhibit a mid-course decrease before rising again. In contrast, the majority of the southern parts of the study area display lower HCO_3^- values, with minima observed at sampling points S13 and S15.

Sulfate (SO_4^{2-}) Distribution

The sulfate ion (SO_4^{2-}) distribution as shown in Figure 5.6f demonstrates a complex hydrogeochemical pattern. In the upper regions—particularly near the mountainous terrains of Djebal Megress and Djebal Anini, as well as in the elevated parts of the Mkhalfa sub-catchment—SO_4^{2-} concentrations are relatively low. However, moving downstream towards the main stream (with a Strahler order of 6), there is a progressive increase in SO_4^{2-} concentrations, reaching a peak near the main stream. Notably, despite its high-altitude setting, sampling point A2 shows elevated SO_4^{2-} levels compared to other locations in the mountainous area.

Chloride (Cl^-) Distribution

The chloride ion (Cl^-) concentration map Figure 5.6g reveals a clear hydrogeochemical trend. In higher regions across all four sub-catchments, Cl^- concentrations remain relatively low. As one moves toward the southern boundaries of urban areas, Cl^- concentrations begin to increase, reaching a maximum near the main stream (Strahler order 6). The southern part of the study area consistently exhibits higher Cl^- concentrations, which likely reflect the combined influences of anthropogenic activities and specific geological settings.

5.4.4 Hydrogeochemical Discussion

Calcium (Ca^{2+})

The K1,2 geological formation is characterized by the presence of limestones with flint and marly limestone containing gypsum. These lithological units are rich in calcium carbonate ($CaCO_3$) and gypsum ($CaSO_4 \cdot 2H_2O$), which, through dissolution, serve as primary sources of Ca^{2+} in groundwater. Additionally, other carbonate-rich formations present in the northern part of the study area further contribute to elevated Ca^{2+} concentrations. In particular, the Saber sub-catchment and the northeastern portion of Boussellam Spring—especially around Djebel Mnaguer where the K1,2 formation is prominent—exhibit higher Ca^{2+} levels. This suggests that the dissolution of calcium-rich minerals is a key process controlling groundwater Ca^{2+} content.

Magnesium (Mg^{2+})

Formation types such as marly limestone and marls, which are abundant in the study area, play a crucial role in contributing Mg^{2+} to the groundwater. In addition, higher Mg^{2+} concentrations are observed in regions where schists and dolomites are present. For example, formations such as K1 5 and K1 1-4 (which contain schists), the J3 3 formation (hosting crystalline dolomites and marls), and the T formation (characterized by black dolomite) all exhibit elevated Mg^{2+} levels. These observations underscore the significant influence of carbonate and dolomitic weathering on magnesium concentrations.

Sodium (Na^{+})

The spatial distribution of sodium is shaped by both natural and anthropogenic processes. Natural inputs include the mobilization of Na^{+} from weathering of sodium-bearing minerals, while anthropogenic sources—such as the discharge of wastewater and industrial effluents—contribute significantly to the Na^{+} load. In addition, sebkhas commonly found in the southern part of the study area act as additional natural sources. The cumulative effect of these processes increases the Na^{+} concentration downstream as river-borne inputs infiltrate into the groundwater or are incorporated into alluvial sediments.

Potassium (K^{+})

Groundwater potassium primarily originates from the weathering of certain silicate minerals (e.g., orthoclase, microcline, hornblende, muscovite, and biotite) commonly found in igneous and metamorphic rocks. Evaporite deposits, such as gypsum, may also contribute to K^{+} levels. In our study area, overall K^{+} concentrations are low, suggesting that both natural and anthropogenic sources are minimal. However, areas adjacent to mountainous regions occasionally exhibit slightly higher K^{+} values, indicating localized geological or human influences that occasionally enhance potassium levels.

Bicarbonate (HCO_3^{-})

The concentrations of bicarbonate in groundwater are strongly influenced by the prevalent limestone lithology. The dissolution of carbonate minerals significantly contributes to the HCO_3^{-} content. Variability in bicarbonate levels can also result from differences in lithology, where regions dominated by limestone yield higher HCO_3^{-}, while areas underlain by non-carbonate rocks in the southern part display lower values. Moreover, factors such as exposure to slightly acidic rainwater and anthropogenic activities (e.g., agriculture and industrial processes) may further modulate the bicarbonate concentrations by altering the chemical equilibrium in the aquifer system.

Sulfate (SO_4^{2-})

Sulfate concentrations in the groundwater reflect the combined effects of lithology, weathering processes, and precipitation chemistry. Geological formations

such as the K1,2 and T units—rich in gypsum and marls—are important natural sources of sulfate through gypsum dissolution. Elevated SO_4^{2-} levels are evident in the Saber sub-catchment and the northeastern portion of Bousselam Spring (notably around Djebel Mnaguer), as well as in areas underlain by Trias (T formation) and marls (e.g., around sampling points S12, S13, and S16). In addition, the influence of agricultural practices (such as the application of sulfate-rich fertilizers) in the karstic aquifer further enhances sulfate inputs, leading to locally higher concentrations.

Chloride (Cl^-)

Chloride in groundwater is influenced by both natural geochemical processes and anthropogenic activities. The low Cl^- concentrations observed in high-altitude and less-populated areas likely reflect natural background levels. In contrast, higher Cl^- concentrations in the lower-elevation and more urbanized regions—and particularly near the main stream—indicate significant anthropogenic loading, possibly from wastewater discharge or other industrial activities. Additionally, the presence of sebkhas, which release both Na^+ and Cl^-, contributes to elevated chloride levels, while unusually high Cl^- at specific sampling points (e.g., A4) may be linked to localized mining activities.

Overall Implications

Collectively, these observations emphasize the importance of integrating hydrogeological and geochemical data to understand the factors that control groundwater quality. The interplay between lithology, natural weathering processes, and anthropogenic influences is critical in shaping the spatial distribution of major ions in the groundwater system. Such an integrated approach is essential for developing effective water resource management and protection strategies, as well as for identifying areas that may require further investigation.

5.5 Data Analysis Results

5.5.1 Correlation Matrix Analysis

TABLE 5.1: Correlation Matrix of Ion Concentrations and Conductivity

	Ca^{2+}	Mg^{2+}	Na^+	K^+	HCO_3^-	SO_4^{2-}	Cl^-	pH	Cond
Ca^{2+}	1	0.697	0.652	0.163	-0.077	0.752	0.817	-0.191	0.921
Mg^{2+}	0.697	1	0.523	0.205	0.067	0.821	0.692	-0.064	0.785
Na^+	0.652	0.523	1	0.136	0.337	0.406	0.789	-0.193	0.821
K^+	0.163	0.205	0.136	1	-0.171	0.323	0.085	0.233	0.124
HCO_3^-	-0.077	0.067	0.337	-0.171	1	-0.080	0.008	-0.623	0.119
SO_4^{2-}	0.752	0.821	0.406	0.323	-0.080	1	0.452	-0.105	0.687
Cl^-	0.817	0.692	0.789	0.085	0.008	0.452	1	-0.073	0.917
pH	-0.191	-0.064	-0.193	0.233	-0.623	-0.105	-0.073	1	-0.233
Cond	0.921	0.785	0.821	0.124	0.119	0.687	0.917	-0.233	1

The relationships identified in our data analysis provide valuable insights into the geochemical processes occurring within the groundwater system. As shown in Table 5.1, the correlation matrix reveals several significant associations between ion concentrations and conductivity in the samples. In our comprehensive hydrogeochemical analysis, we examined the relationships between various ions and conductivity, as well as the associations among different ions themselves.

We found that conductivity exhibits strong correlations with Na^+, Ca^{2+}, Mg^{2+}, and Cl^-. This is expected since conductivity is directly related to the overall concentration of dissolved ions in water. In addition, there is a moderate correlation between conductivity and sulfate (SO_4^{2-}), and weak correlations with potassium (K^+) and bicarbonate (HCO_3^-).

Regarding inter-ionic relationships, the matrix shows:

- **Strong correlations** between Ca^{2+} and both SO_4^{2-} and Cl^-, between Mg^{2+} and SO_4^{2-}, and between Na^+ and Cl^-. These strong associations suggest that these ions likely originate from common geological sources or are influenced by similar geochemical processes.
- **Moderate correlations** between Ca^{2+} and Mg^{2+}; among Ca^{2+}, Mg^{2+}, and Na^+; between Mg^{2+} and Cl^-; and between HCO_3^- and pH, indicating that while these ions often vary together, additional factors also influence their concentrations.
- **Weak correlations** among other variables, indicating little to no linear relationship and highlighting the complexity of the groundwater geochemistry.

These findings are instrumental in understanding the intricate dynamics of our studied system.

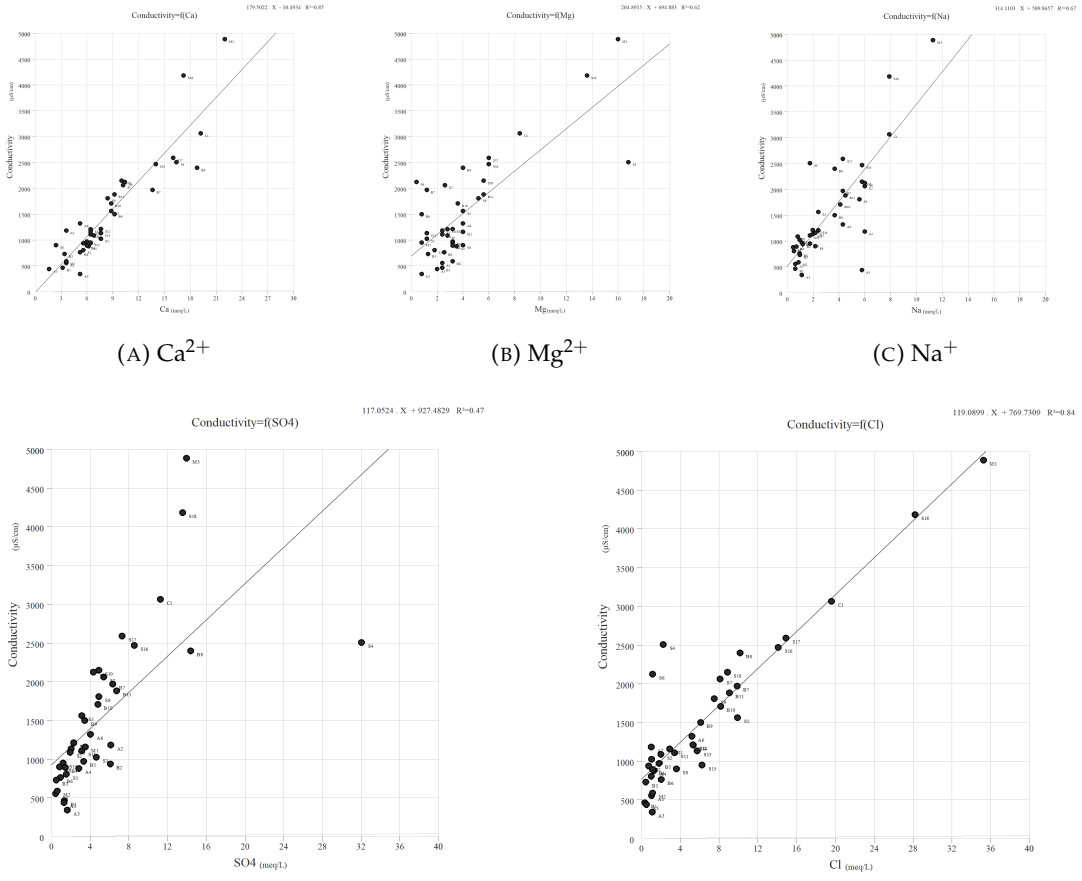
5.5.2 Linear Regression Analysis

In order to substantiate the correlations observed in our study, we undertook a linear regression analysis. Whereas the correlation matrix measures the strength of the linear relationship between two variables, linear regression enables us to predict one variable from another. The R^2 value indicates the proportion of the variation in the dependent variable that can be explained by the independent variable.

This analysis was performed for each strong and moderate relationship identified in our correlation matrix, both between conductivity and the ions, and among the ions themselves.

Conductivity:

Figure 5.7 presents the linear regression analysis between electrical conductivity and key ions. Panels (a–c) correspond to the cations Ca^{2+}, Mg^{2+}, and Na^+ (Figures 5.7a–5.7c), while panels (d–e) show the anions SO_4^{2-} and Cl^- (Figures 5.7d, 5.7e). The R^2 values indicate the proportion of conductivity variability explained by each ion.



(A) Ca^{2+} (B) Mg^{2+} (C) Na^{+}

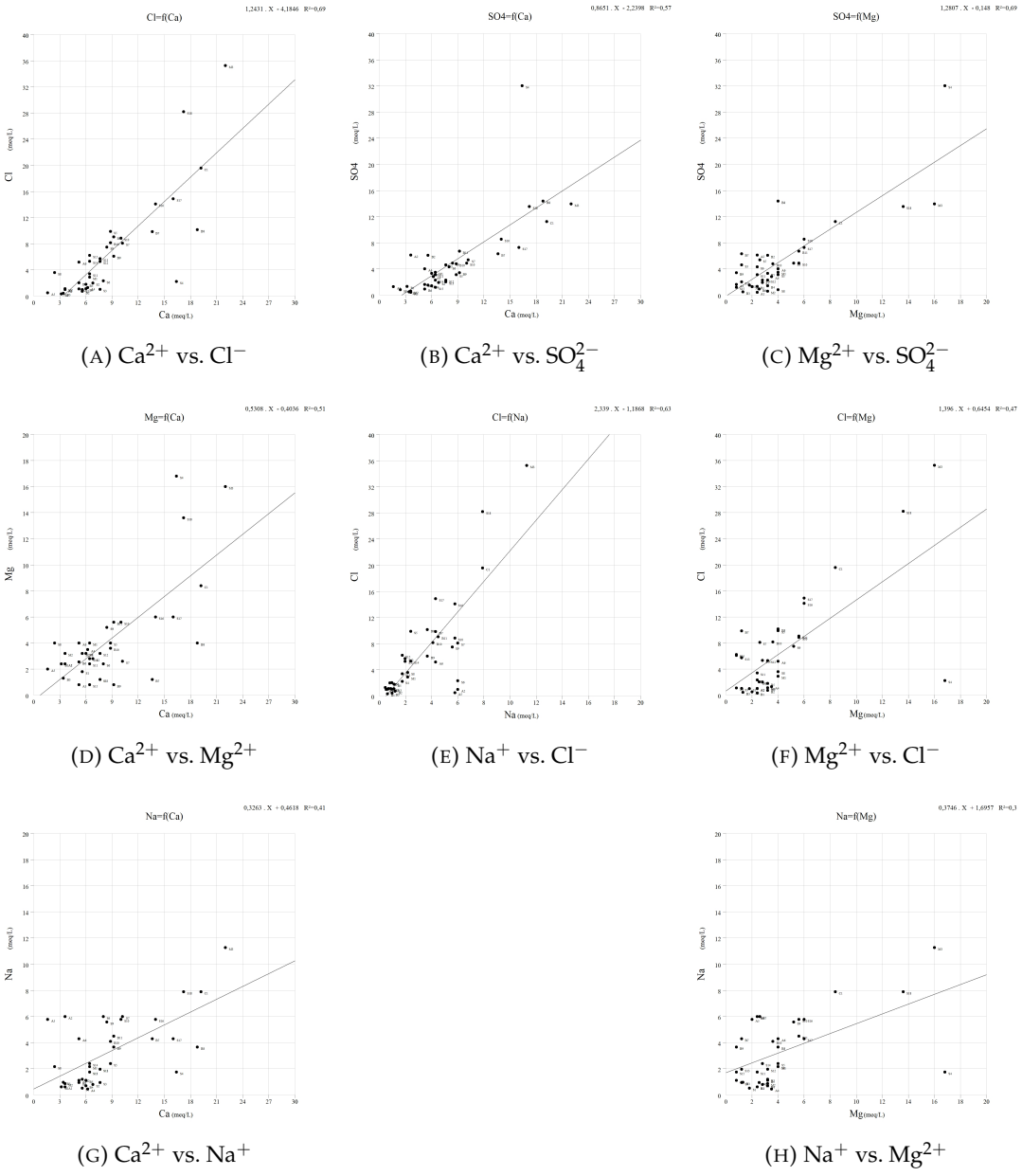
(D) SO_4^{2-} (E) Cl^{-}

FIGURE 5.7: Linear regression plots of electrical conductivity against major cations and anions. Panels (a–c) show cations (Ca^{2+}, Mg^{2+}, Na^{+}) and (d–e) show anions (SO_4^{2-}, Cl^{-}).

- *Calcium (Ca^{2+}) and Conductivity:* As shown in Figure 5.7a, a strong positive relationship with an R^2 value of 0.84 reinforces the correlation observed earlier, indicating that Ca^{2+} significantly contributes to conductivity.
- *Chloride (Cl^{-}) and Conductivity:* As shown in Figure 5.7e, a strong positive relationship with an R^2 value of 0.85 confirms that Cl^{-} plays an important role in influencing conductivity.
- *Magnesium (Mg^{2+}) and Conductivity:* As shown in Figure 5.7b, an R^2 value of 0.64 suggests a moderately strong relationship, showing that variations in Mg^{2+} account for a significant portion of the conductivity variability.
- *Sodium (Na^{+}) and Conductivity:* As shown in Figure 5.7c An R^2 value of 0.67 indicates a moderately strong relationship, demonstrating that Na^{+} also substantially influences conductivity.
- *Sulfate (SO_4^{2-}) and Conductivity:* As shown in Figure 5.7d, an R^2 value of 0.47 confirms a moderate relationship, suggesting that SO_4^{2-} impacts conductivity to a lesser extent compared to the other ions.

Inter-Ionic Relationships:

Figure 5.8 presents the inter-ionic linear regression plots between major cations and anions. Panels (a–b) show Ca^{2+} vs. Cl^{-} and SO_4^{2-}, (c–d) Mg^{2+} vs. SO_4^{2-} and Ca^{2+}, (e–f) Na^{+} and Mg^{2+} vs. Cl^{-}, and (g–h) Ca^{2+} vs. Na^{+} and Na^{+} vs. Mg^{2+}. The R^2 values quantify the strength of each pairwise relationship



(A) Ca^{2+} vs. Cl^{-} (B) Ca^{2+} vs. SO_4^{2-} (C) Mg^{2+} vs. SO_4^{2-}

(D) Ca^{2+} vs. Mg^{2+} (E) Na^{+} vs. Cl^{-} (F) Mg^{2+} vs. Cl^{-}

(G) Ca^{2+} vs. Na^{+} (H) Na^{+} vs. Mg^{2+}

FIGURE 5.8: Inter-ionic linear regression plots among major solutes. Panels (a–h)quantify the strength of each pairwise relationship, showing best-fit lines and R^2 values.

- *Calcium (Ca^{2+}) and Chloride (Cl^{-}):* The R^2 value of 0.69 suggests a strong relationship, reinforcing the idea of a common geochemical process or source affecting both ions.
- *Calcium (Ca^{2+}) and Sulfate (SO_4^{2-}):* Although the correlation matrix indicated a strong association, the regression reveals a moderate relationship

with an R^2 value of 0.57. This implies that while Ca^{2+} influences SO_4^{2-}, other factors also play a role.

- *Magnesium (Mg^{2+}) and Sulfate (SO_4^{2-}):* With an R^2 value of 0.69, the relationship is moderately strong, implying that increases in Mg^{2+} are closely associated with increases in SO_4^{2-}.
- *Calcium (Ca^{2+}) and Magnesium (Mg^{2+}):* An R^2 value of 0.51 indicates a moderate relationship, suggesting that while these ions often vary together, additional geochemical processes may also influence Mg^{2+}.
- *Sodium (Na^+) and Chloride (Cl^-):* The R^2 value of 0.63 indicates a moderately strong relationship, which suggests that a common source or process affects both Na^+ and Cl^-.
- *Magnesium (Mg^{2+}) and Chloride (Cl^-):* An R^2 value of 0.47 confirms a moderate association, implying that changes in Mg^{2+} do not always correspond directly with changes in Cl^-.
- *Calcium (Ca^{2+}) and Sodium (Na^+):* The regression shows a weak relationship with an R^2 value of 0.41, indicating that Ca^{2+} alone is not a reliable predictor of Na^+ concentrations.
- *Magnesium (Mg^{2+}) and Sodium (Na^+):* An R^2 value of 0.30 suggests a weak relationship, confirming that Mg^{2+} is not a strong predictor of variations in Na^+ concentrations.

5.6 Data Analysis Discussion

A correlation matrix quantifies the linear relationship between two variables, with coefficients ranging from –1 to 1. A coefficient near 1 indicates a strong positive linear relationship, whereas a value near –1 signifies a strong negative linear relationship. In contrast, the R^2 value from linear regression quantifies the proportion of variance in the dependent variable that is explained by the independent variable(s); a value closer to 1 implies that the model explains a large portion of the variability, whereas a value near 0 indicates the model has little explanatory power.

Relationships with Conductivity:

Our analysis reveals that conductivity is strongly correlated with the major ions Ca^{2+}, Mg^{2+}, Na^+, and Cl^-. High R^2 values from the linear regression for Ca^{2+} (0.84) and Cl^- (0.85) provide quantitative evidence that these ions significantly enhance the electrical conductivity of groundwater by increasing the total ionic concentration. In the cases of Mg^{2+} (with an R^2 of 0.64) and Na^+ (with an R^2 of 0.67), the relationships are moderately strong, indicating that variability in these ions also contributes notably to conductivity, albeit to a slightly lesser extent. Conversely, conductivity exhibits a moderate relationship with sulfate (SO_4^{2-}; $R^2 = 0.47$), suggesting that while sulfate does influence conductivity, its effect is less pronounced—possibly reflecting more variable sources or additional controlling factors.

Inter-Ionic Relationships:

The correlation matrix and subsequent regression results further reveal that certain pairs of ions tend to vary together. For example, the strong association found between Ca^{2+} and Cl^{-} (with an R^2 of 0.69) indicates that these ions likely originate from a common geochemical source or are released via similar weathering processes. Similarly, the relationship between Mg^{2+} and SO_4^{2-} (with an R^2 of 0.69) suggests that the dissolution of sulfated minerals or similar geochemical mechanisms may be controlling their concentrations.

In contrast, moderate relationships—such as the one observed between Ca^{2+} and Mg^{2+} (with an R^2 of 0.51)—imply that, although these ions often increase or decrease together, additional geochemical processes (such as differential solubility or selective ion exchange) also influence their variability. Moreover, the regression analysis reveals weak associations in some cases, for example between Ca^{2+} and Na^{+} ($R^2 = 0.41$) and between Mg^{2+} and Na^{+} ($R^2 = 0.30$), underscoring that these ions are governed by more complex or independent processes.

Overall Implications:

The combination of high R^2 values and strong correlations for conductivity with Ca^{2+}, Cl^{-}, Mg^{2+}, and Na^{+} corroborates the key role of these ions in controlling groundwater electrical properties. Likewise, the observed interionic relationships—strong, moderate, or weak—provide insights into potential common sources (such as mineral dissolution from carbonate or evaporite rocks) and geochemical processes (including evaporation, ion exchange, and buffering reactions). These findings highlight the complex interplay of natural and anthropogenic factors affecting groundwater quality and underscore the necessity of integrating multiple lines of geochemical evidence for effective water resource management.

5.7 Ionic Ratio Analysis

Ionic ratios, a key concept in hydrochemistry, were employed to gain a deeper understanding of the geochemical processes influencing our water samples. By comparing the proportions of different ions, these ratios help decipher various aspects of groundwater chemistry, including the sources of salinity, the dominant geochemical processes, and the movement of saline water through the system.

To further elucidate these processes, we categorized the ionic ratios into three distinct ranges based on established scientific literature and our understanding of the region's geochemistry. These ranges are defined as follows:

- **Less than 0.9**: Conditions where one ion is significantly more prevalent than the other, suggesting a dominant influence from a particular geochemical process or source.
- **Between 0.9 and 1.1**: Conditions where the compared ions are approximately equal in concentration, indicating a balanced influence of various processes or sources.
- **Greater than 1.1**: Conditions where the ratio exceeds unity, implying that one ion becomes increasingly dominant, which may signal a shift in the prevailing geochemical regime or source.

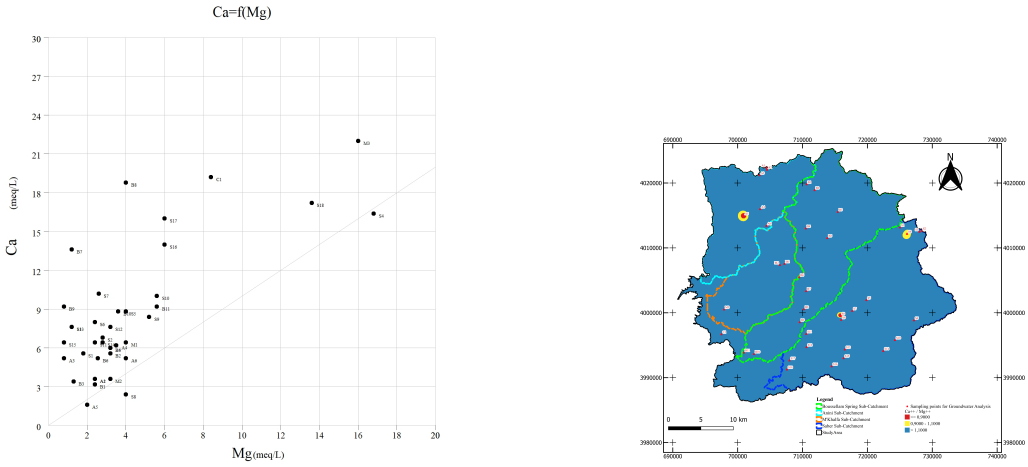
Furthermore, to provide a spatial context to our findings, we created maps that visually represent these ionic ratio categories across the study area. Such maps facilitate the identification of patterns and anomalies—features that might not be readily apparent from numerical data alone. Through this approach, we can better delineate areas influenced by particular geochemical processes and ultimately develop a more comprehensive understanding of the groundwater system.

In summary, the use of ionic ratios, combined with spatial mapping, underscores our commitment to employing comprehensive methods to characterize the complex hydrogeochemical framework of our study area. This integrative technique not only enhances the interpretation of water chemistry data but also informs water resource management strategies by highlighting key areas of geochemical variability.

5.7.1 Ionic Ratio Results

The computed ionic-ratio outcomes—together with their regression plots and spatial IDW maps—are presented below.

- *Ca^{2+}/Mg^{2+}:* As shown in Figure 5.9, only two sampling points (A5 and S8) exhibited a ratio less than 1.1, suggesting a dominance of Mg^{2+} over Ca^{2+} at these locations. Conversely, sampling point S4 displayed a ratio between 0.9 and 1.1, indicating that Ca^{2+} and Mg^{2+} are released into the water at similar concentration levels. Notably, the remaining 36 sampling points showed a Ca^{2+}/Mg^{2+} ratio greater than 1.1, suggesting a dominance of Ca^{2+} ions.

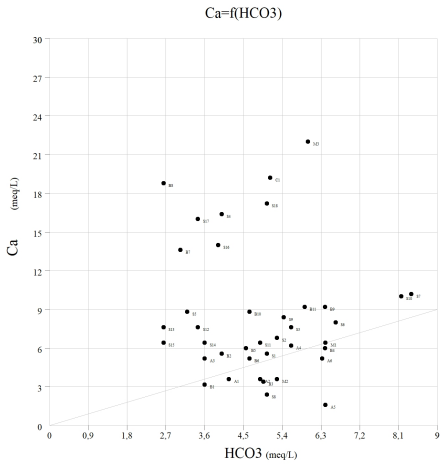


(a) Binary diagram (b) Spatial IDW map

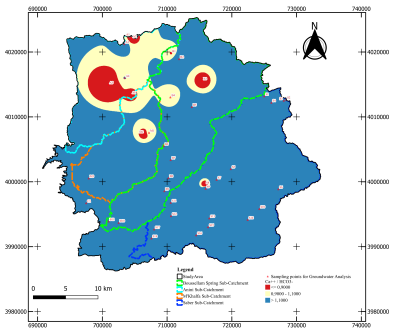
FIGURE 5.9: Ca^{2+}/Mg^{2+} ratio: (a) sample-by-sample binary diagram; (b) IDW-interpolated spatial distribution.

- *Ca^{2+}/HCO_3^-:* Figure 5.10 shows that sampling points A1, A2, B1, B3, A5, A6, M2, and S8 have a Ca^{2+}/HCO_3^- ratio less than 0.9, which suggests that carbonate weathering is the dominant process at these locations. In contrast, sampling points B4 and M1 exhibit ratios between 0.9 and

1.1, indicating a balanced interaction between carbonate weathering and other geochemical processes. The remaining sampling points display a ratio greater than 1.1, implying a dominance of calcium ions relative to bicarbonate.



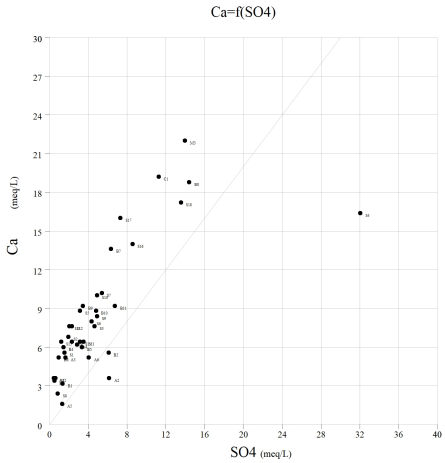
(a) Binary diagram



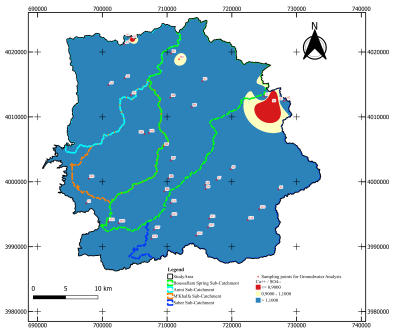
(b) Spatial IDW map

FIGURE 5.10: Ca^{2+}/HCO_3^- ratio: (a) sample-by-sample binary diagram; (b) IDW-interpolated spatial distribution.

– *Ca^{2+}/SO_4^{2-}:* In Figure 5.11, distinct patterns are evident in the Ca^{2+}/SO_4^{2-} ratio. Sampling points S4 and A2 appear to be affected by gypsum dissolution, as indicated by their ratios. Sampling point B2 shows a ratio between 0.9 and 1.1, suggesting a balanced contribution from gypsum dissolution and other geochemical processes, while the remaining sampling points have ratios greater than 1.1, indicating a dominance of calcium ions.



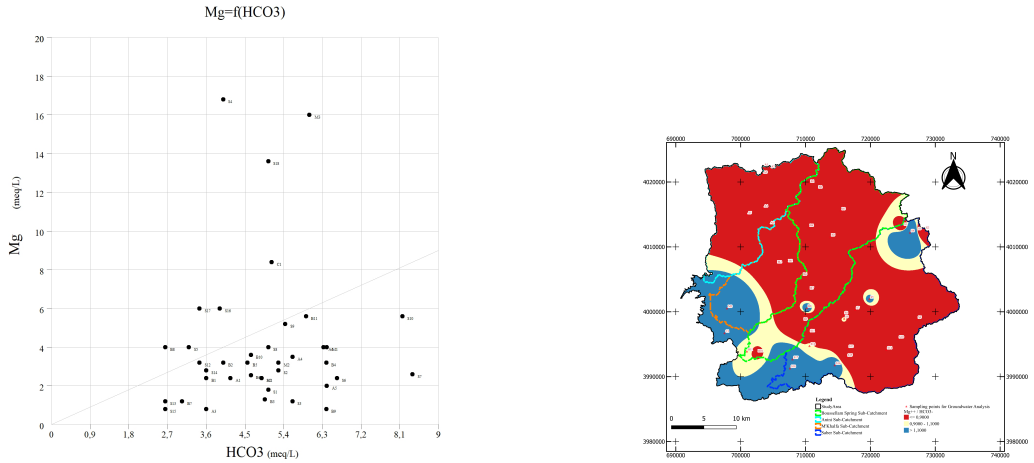
(a) Binary diagram



(b) Spatial IDW map

FIGURE 5.11: Ca^{2+}/SO_4^{2-} ratio: (a) sample-by-sample binary diagram; (b) IDW-interpolated spatial distribution.

– *Mg^{2+}/HCO_3^-:* Figure 5.12 highlights that sampling points S4, B8, S5, and those in the southern sector (S16, S17, S18, C1, M3) are more influenced by dolomite dissolution, as reflected by their Mg^{2+}/HCO_3^- ratios. Meanwhile, sampling points S9, S12, and B11 present ratios between 0.9 and 1.1, indicating a balanced interaction between dolomite dissolution and other geochemical influences. The remaining sampling points, with ratios less than 0.9, suggest relatively lower Mg^{2+} contributions.

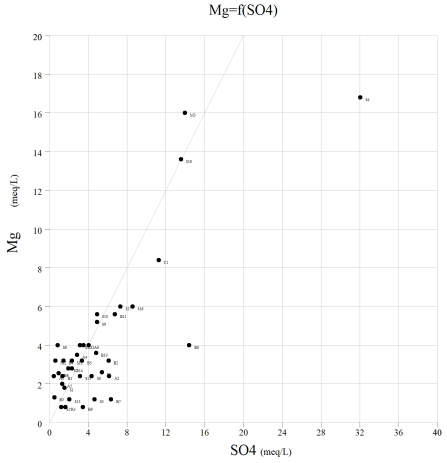


(a) Binary diagram

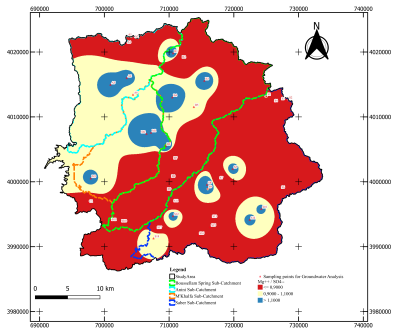
(b) Spatial IDW map

FIGURE 5.12: Mg^{2+}/HCO_3^- ratio: (a) sample-by-sample binary diagram; (b) IDW-interpolated spatial distribution.

– *Mg^{2+}/SO_4^{2-}:* As shown in Figure 5.13, the Mg^{2+}/SO_4^{2-} ratio exhibits clear spatial variability. Sampling points A1, A4, A5, M1, M2, B1, B3, B4, B6, S2, S1, S5, S8, S10, S12, S14, and M3 show ratios greater than 1.1, suggesting a dominance of Mg^{2+} ions—indicative of increased interaction with formations containing dolomite or clay. Conversely, in the western part of the study area, sampling points A6, B5, S9, and S18 have ratios between 0.9 and 1.1, where SO_4^{2-} becomes more prominent relative to Mg^{2+}.



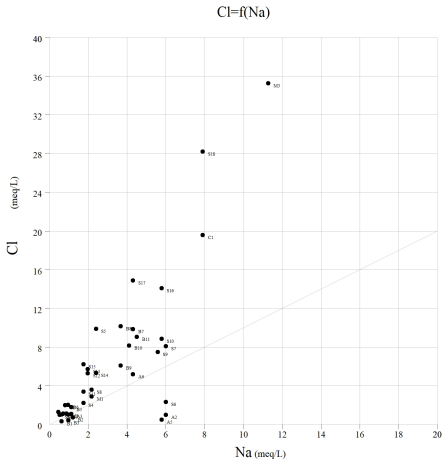
(a) Binary diagram



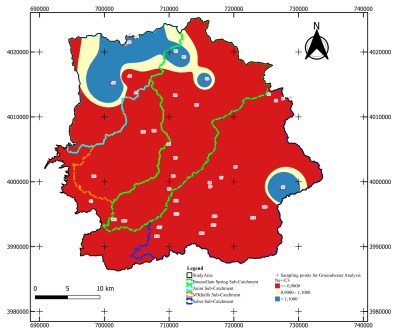
(b) Spatial IDW map

FIGURE 5.13: Mg^{2+}/SO_4^{2-} ratio: (a) sample-by-sample binary diagram; (b) IDW-interpolated spatial distribution.

– *Na^+/Cl^-:* As shown in Figure 5.14, distinct patterns are observed in the Na^+/Cl^- ratio. In the northern region around Djebel Megress and Djebal Anini, the ratio exceeds 1.1, possibly due to the use of road salt—a consequence of the high altitude, low temperatures, and presence of snow and ice during winter. At sampling point S6 in an agricultural area, fertilizer usage may be influencing the ratio. In all other parts of the study area, chloride appears dominant, resulting in a Na^+/Cl^- ratio below 1.



(a) Binary diagram

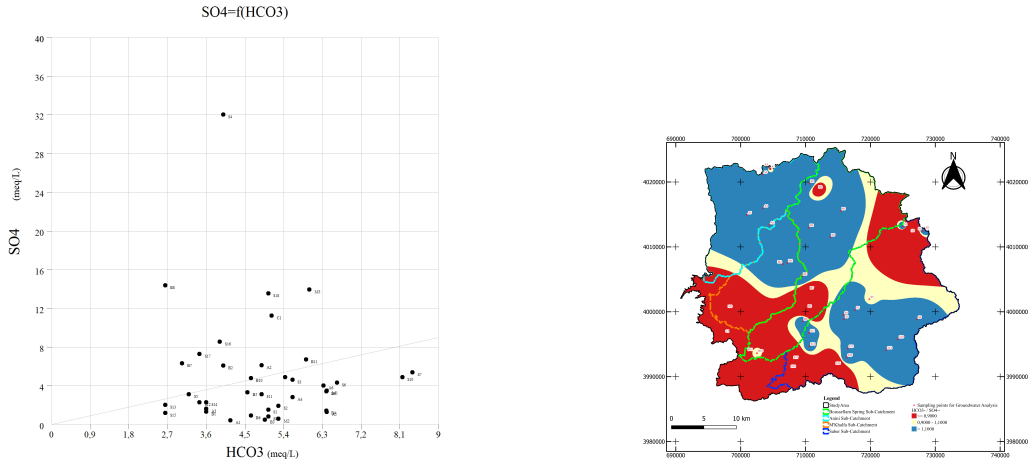


(b) Spatial IDW map

FIGURE 5.14: Na^+/Cl^- ratio: (a) sample-by-sample binary diagram; (b) IDW-interpolated spatial distribution.

– *HCO_3^-/SO_4^{2-}*:Figure 5.15, illustrates the spatial distribution of the HCO_3^-/SO_4^{2-} ratio. In the northern part of the study area, most sampling points exhibit a dominance of carbonate ions (HCO_3^-), which is indicative of underlying carbonate-rich formations. However, sampling points S4 and

B2 deviate from this trend, suggesting a greater influence of gypsum-rich formations at those locations. In the southern part, downstream of the subcatchments, sulfate ions begin to dominate—likely due to the influence of sebkhas (salt flats) that contribute sulfate to the groundwater. Additionally, sampling points B7 and B8, located in an industrial area, may reflect industrial influences on water chemistry.

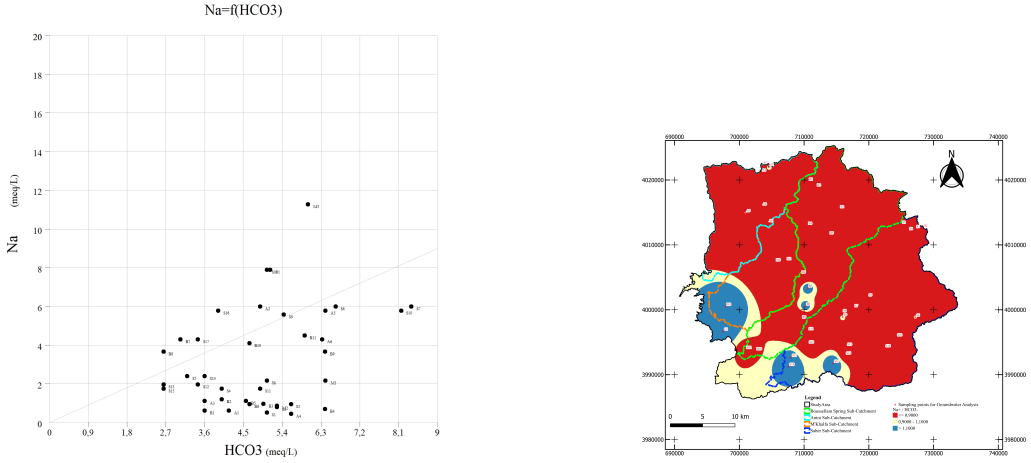


(a) Binary diagram

(b) Spatial IDW map

FIGURE 5.15: HCO_3^-/SO_4^{2-} ratio: (a) sample-by-sample binary diagram; (b) IDW-interpolated spatial distribution.

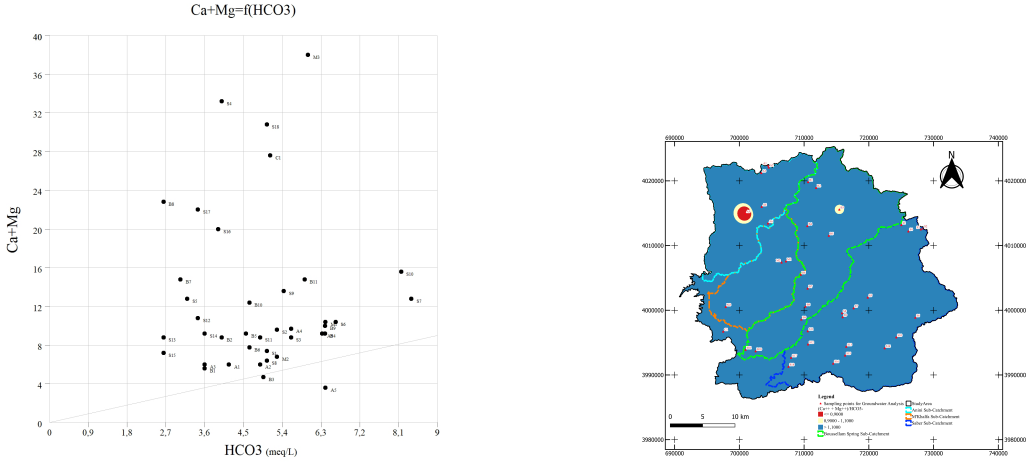
– *Na^+/HCO_3^-:* As illustrated in Figure 5.16 the Na^+/HCO_3^- ratio shows distinct patterns. In the southern part of the study area, downstream of each subcatchment, the ratio is greater than 1.1, which could be attributed to inputs from sebkhas. Sampling points B7 and B8, in an industrial zone, also exhibit elevated ratios, whereas the remainder of the study area shows a ratio below 0.9.



(a) Binary diagram (b) Spatial IDW map

FIGURE 5.16: Na^+/HCO_3^- ratio: (a) sample-by-sample binary diagram; (b) IDW-interpolated spatial distribution.

– *$(Ca^{2+}+Mg^{2+})/HCO_3^-$:* As shown in Figure 5.17, the $(Ca^{2+}+Mg^{2+})/HCO_3^-$ ratio demonstrates limited variation across sampling points. Only one water sample has a ratio below 0.9, signaling a dominance of bicarbonate at that site; one sample falls within the 0.9 to 1.1 range, suggesting balanced dissolution of calcium and magnesium relative to carbonate; the remaining samples exhibit ratios higher than 1.1, highlighting a predominance of calcium and magnesium ions over bicarbonate.

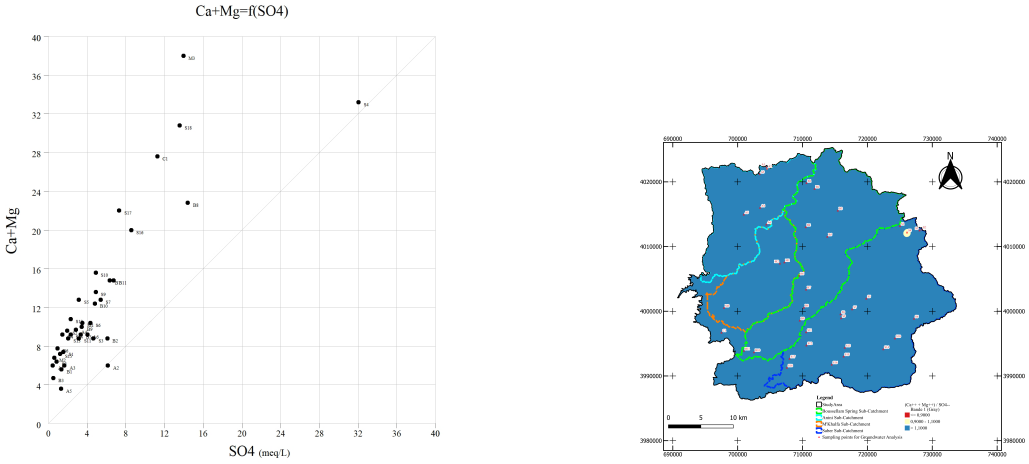


(a) Binary diagram (b) Spatial IDW map

FIGURE 5.17: $(Ca^{2+}+Mg^{2+})/HCO_3^-$ ratio: (a) sample-by-sample binary diagram; (b) IDW-interpolated spatial distribution.

– *$(Ca^{2+}+Mg^{2+})/SO_4^{2-}$:* Figure 5.18 shows that across the study area, the $(Ca^{2+}+Mg^{2+})/SO_4^{2-}$ ratio exceeds 1.1 at all sampling points. This uniform observation indicates that the sources of calcium and magnesium are not exclusively tied to gypsum dissolution—the primary source of

sulfate—suggesting additional sources or processes contribute to the calcium and magnesium content in the groundwater.



(a) Binary diagram (b) Spatial IDW map

FIGURE 5.18: $(Ca^{2+}+Mg^{2+})/SO_4^{2-}$ ratio: (a) sample-by-sample binary diagram; (b) IDW-interpolated spatial distribution.

5.7.2 Ionic Ratio Discussion

– Ca^{2+}/Mg^{2+}: The Ca^{2+}/Mg^{2+} ratio in water samples can provide valuable insights into the geochemical processes and the geological formations influencing the water chemistry. In our case, only sampling points A5 and S8 have a Ca^{2+}/Mg^{2+} ratio less than 1.1 which implies the dominance of Mg^{2+} over Ca^{2+} at these locations. Conversely, sampling point S4 belongs to the category between 0.9 and 1.1 which implies that Ca^{2+} and Mg^{2+} are released in water at the same levels of concentration, while all other 36 sampling points have a ratio greater than 1.1, suggesting that our study area contains more formations that contain Ca^{2+} ions.
A5: Located in a geological formation containing gray marl and limestone bedded at the summit. The Ca^{2+}/Mg^{2+} ratio less than 1 suggests that the water has interacted more with magnesium-rich minerals present in the marl or limestone, leading to a higher concentration of magnesium ions relative to calcium ions.
S8: Situated in a geological formation containing clay and conglomerates. The low Ca^{2+}/Mg^{2+} ratio could be due to the dissolution of magnesium-rich minerals present in the clay or conglomerates.
S4: Falls into the category where the ratio is between 0.9 and 1.1. This implies that Ca^{2+} and Mg^{2+} are released into the water at similar concentration levels, suggesting a balanced contribution of calcium and magnesium from the geological formations at this location. S4 is situated in the geological formation E 1,2 which contains limestone with flint and marly limestone, sometimes with gypsum. The low Ca^{2+}/Mg^{2+} ratio could be due to the dissolution of magnesium-rich minerals present in the marly limestone or gypsum.

- Ca^{2+}/HCO_3^-: The observed patterns in the Ca^{2+}/HCO_3^- ratio in our study area provide valuable insights into the extent of carbonate weathering, a key hydrogeological process. Carbonate weathering occurs when slightly acidic rainwater interacts with carbonate rocks (like limestone or chalk), leading to the dissolution of the rock and the formation of bicarbonate ions (HCO_3^-) and calcium ions (Ca^{2+}). The dominance of bicarbonate ions at sampling points A1, A2, B1, B3, A5, A6, M2, and S8 could be due to this carbonate weathering process, suggesting that these areas may be underlain by carbonate rocks and that the groundwater has interacted extensively with these formations. Specifically, water samples S8 and A6 are located in a formation containing lacustrine limestone. Sample A2 is located in a limestone formation K2 5-6, while A5 is located in a formation K2 3-6 containing gray marl and limestone bedded at the summit. The balanced Ca^{2+}/HCO_3^- ratio at sampling points B4 and M1 suggests a balanced interaction between carbonate weathering and other geochemical processes. The dominance of calcium ions at the remaining sampling points could suggest the presence of other geological formations or geochemical processes that are contributing to a higher concentration of Ca^{2+} ions in the water samples.

- Ca^{2+}/SO_4^{2-}: The Ca^{2+}/SO_4^{2-} ratio in water samples is a significant indicator of the geochemical processes and geological influences at play. In our study, sampling points S4 and A2 are affected by gypsum dissolution, as indicated by their Ca^{2+}/SO_4^{2-} ratios. Gypsum dissolution is a process where water interacts with gypsum (a mineral composed of hydrated calcium sulfate), leading to the dissolution of the gypsum and the formation of sulfate ions (SO_4^{2-}) and calcium ions (Ca^{2+}). Sampling point B2 has a ratio between 0.9 and 1.1, suggesting that at this location, sulfate ions (SO_4^{2-}) and calcium ions (Ca^{2+}) are being released into the water at similar concentration levels. This could indicate a balanced interaction between gypsum dissolution and other geochemical processes. The remaining sampling points have a ratio greater than 1.1, indicating a dominance of calcium ions. The water sample from location S4, situated within the E 1,2 geological formation characterized by limestone with flint and marly limestone occasionally interspersed with gypsum, suggests that the interaction of water with this formation results in a high concentration of sulfate ions (SO_4^{2-}), likely due to the dissolution of gypsum. For water sample A1, the proximity of the E 1,2 formation suggests that the groundwater flow has interacted with this formation. At location B3, which is characterized by agricultural activity, the high concentration of sulfate could be attributed to the use of fertilizers.

- Mg^{2+}/HCO_3^-: The Mg^{2+}/HCO_3^- ratio in water samples is a significant hydrogeochemical parameter that can be used to infer the influence of various geological formations on groundwater chemistry. In our study, sampling points S4, B8, S5, and those in the south (S16, S17, S18, C1, M3) show a dominance of Mg^{2+}, suggesting that the groundwater at these locations has interacted with formations that result in a high concentration of magnesium ions. This could be due to the dissolution of marl, clay, or conglomerates present in these areas. Sampling points S9, S12, and B11 have a Mg^{2+}/HCO_3^- ratio between 0.9 and 1.1, suggesting a balanced interaction between the dissolution of marl, clay, or conglomerates and

other geochemical processes. The remaining sampling points have a ratio less than 0.9, indicating a lower concentration of Mg^{2+} ions.

- Mg^{2+}/SO_4^{2-}: The Mg^{2+}/SO_4^{2-} ratio in water samples is a significant hydrogeochemical parameter that can be used to infer the influence of various geological formations on groundwater chemistry. In our study, sampling points A1, A4, A5, M1, M2, B1, B3, B4, B6, S2, S1, S5, S8, S10, S12, S14, and M3 show a dominance of Mg^{2+}, suggesting that the groundwater at these locations has interacted more with formations containing conglomerates or clay, and particularly with marl formations such as K2 3-6 MPl which are dominant in the east part of the study area as shown by the geological map. On the other hand, the western part of our study area contains more sampling points where the SO_4^{2-} ions are dominant over Mg^{2+}. Sampling points A6, B5, S9, and S18 have a Mg^{2+}/SO_4^{2-} ratio between 0.9 and 1.1, indicating a balanced interaction between the dissolution of gypsum and marl or clay at these locations.

- Na^+/Cl^-: The observed patterns in the Na^+/Cl^- ratio in our water samples provide valuable insights into the geochemical processes and geological influences at play in our study area. In the northern part, around Djebel Megriz and Djebal Anini, the high Na^+/Cl^- ratio suggests the presence of other sources of Na^+. This could be due to anthropogenic influences such as the use of road salt, which can contribute significant amounts of sodium to groundwater. Additionally, agricultural activities at location S6 could also be contributing to the observed Na^+/Cl^- ratio through the use of certain types of fertilizers that contain sodium. The dominance of chloride ions over sodium ions in the rest of the study area indicates the presence of more sources that release chloride ions. This could suggest the influence of geological formations containing chloride-bearing minerals, geochemical processes such as halite dissolution, or human activities (e.g., industrial processes or waste disposal) that increase the chloride ion concentration.

- HCO_3^-/SO_4^{2-}: The observed patterns in the HCO_3^-/SO_4^{2-} ratio in our water samples provide valuable insights into the hydrogeochemical processes at play in our study area. Sampling points situated in the northwest part are characterized by a dominance of carbonate ions (HCO_3^-), except for S4 and B2 which suggest the presence of formations that contain more gypsum at these locations. In the southern part, downstream of each subcatchment, sulfate ions (SO_4^{2-}) start to dominate. This could be due to the presence of sebkhas, salt flats that can be drained by rivers and reach the groundwater, contributing to the SO_4^{2-} content, and it is also characterized by the presence of Triassic formations, which imply the presence of gypsum-rich formations. For sampling points B7 and B8, which are situated in an industrial area, the geochemical characteristics could be influenced by industrial activities.

- Na^+/HCO_3^-: The observed patterns in the Na^+/HCO_3^- ratio in our water samples provide valuable insights into the hydrogeochemical processes at play in our study area. This ratio is higher than 1.1 in the southern part, downstream of each subcatchment, characterized by the dominance of SO_4^{2-} ions. This could be due to the presence of sebkhas,

which can be drained by rivers and contribute sulfate to the groundwater; it is also characterized by the presence of Triassic formations, which imply the presence of gypsum formation. For sampling points B7 and B8 in an industrial area, the geochemical characteristics could be influenced by industrial activities. In contrast, for the rest of the study area the Na^+/HCO_3^- ratio is lower than 0.9.

- $(Ca^{2+} + Mg^{2+})/HCO_3^-$*:* The $(Ca^{2+} + Mg^{2+})/HCO_3^-$ ratio in our water samples provides valuable insights into the hydrogeochemical processes at play.
  Water sample A5: This sample, located in the geological formation K2 3-6, has a ratio lower than 0.9, indicating a dominance of carbonate ions (HCO_3^-) at this location. This could suggest a higher rate of carbonate weathering or an enhanced interaction with the carbonate-rich formation K2 3-6.
  Water sample B3: Situated in the MPl formation that contains clay, conglomerates, and lacustrine limestone, this sample exhibits a ratio within the range of 0.9 to 1.1, suggesting that Ca^{2+} and Mg^{2+} are released into the water at similar concentration levels as HCO_3^-.
  Water samples with ratio higher than 1.1: The remaining water samples have a ratio higher than 1.1, indicating a dominance of calcium and magnesium ions over carbonate ions. This suggests that, in these areas, formations release Ca^{2+} and Mg^{2+} more readily than carbonate ions. Notably, the carbonate ions dominate only in one sample point, A5, implying that at this location the carbonate weathering is higher and the water has interacted extensively with carbonate formations. In contrast, the ratio for sample point B3 falls within 0.9 to 1.1, suggesting that Mg^{2+} and Ca^{2+} are released in the same concentration as HCO_3^-. For the rest of the study area, Ca^{2+} and Mg^{2+} are dominant over HCO_3^-, implying the presence of formations that release more Ca^{2+} and Mg^{2+} than HCO_3^-.
- $(Ca^{2+} + Mg^{2+})/SO_4^{2-}$*:* In the study area, the $(Ca^{2+} + Mg^{2+})/SO_4^{2-}$ ratio for all sampling points exceeds 1.1. This indicates that the sources of calcium and magnesium ions are not exclusively related to gypsum, a primary source of sulfate ions (SO_4^{2-}).

5.8 Piper Diagram

The Piper diagram, a tri-linear plot, will be used to examine the geochemical relationships between various ions in water samples. The sampling points are divided into two groups. The first group is within the Saber sub-catchment, influenced by groundwater flow from Djebal Mnaguer. The second group includes the Anini, Boussellam Spring, and M'khalfa sub-catchments, influenced by groundwater flow from Djebal Megris. The groundwater flow in these areas transitions from higher to lower elevations. The upcoming analysis using the Piper diagram will elucidate the major ion composition and geochemical processes within these sub-catchments.

5.8.1 Anini, Boussellam, and Mkhalfa subcatchments

As shown in Figure 5.19, the Piper diagram which includes both cation and anion ternary plots, provides a comprehensive overview of the hydrogeochemical characteristics of the Anini, Boussellam, and Mkhalfa subcatchments.

Cation Ternary Plot: The majority of sampling points are located in the calcium field, indicating a significant influence of calcium-rich minerals. However, points M2, B11, M3, and A6 are located in the mixed field, suggesting a more complex geochemical environment. Points A2 and A5 are located in the sodium and potassium field. **Anion Ternary Plot:** Points A2, B2, and B8 are located in the sulfate field. Points B7 and M3 are located in the chloride field. Points M1, A6, B5, B9, B10, and B11 are located in the mixed field. The remaining points are located in the bicarbonate field.

Diamond plot: In the Anini, Boussellam, and Mkhalfa subcatchments, the distribution of sampling points within the diamond plot of the Piper diagram suggests distinct hydrogeochemical characteristics. Sampling points A1, A3, A4, B1, B3, B4, B6, and M2 are located in the left quadrant. The only sampling point in the bottom quadrant is A5. The only sampling point in the right quadrant is A2. The remaining sampling points are located in the top quadrant.

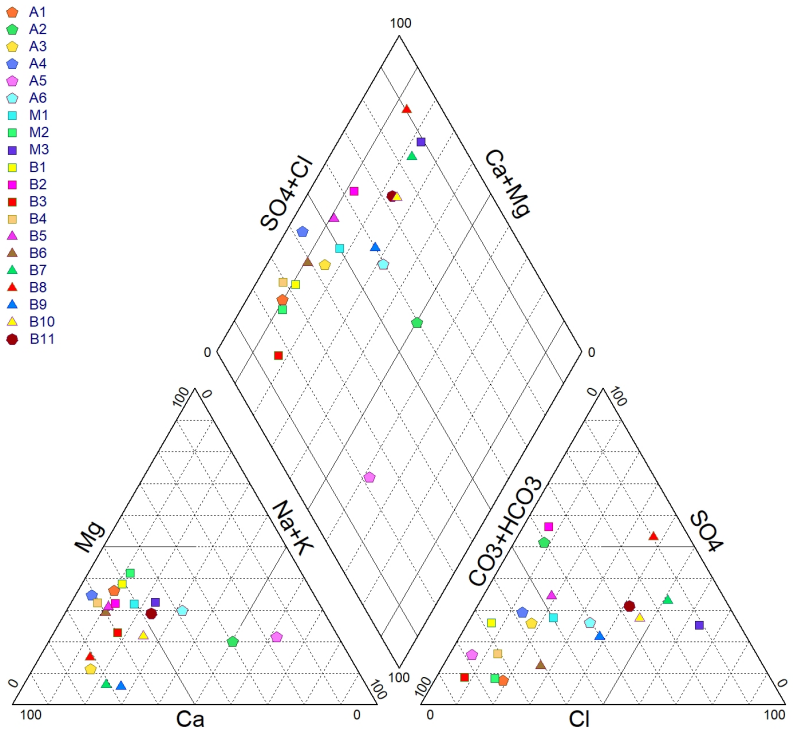


FIGURE 5.19: Piper trilinear diagram summarizing the major-ion chemistry of groundwater samples from the Anini, Boussellam and M'khalfa subcatchments.

5.8.2 Saber subcatchment

In the Saber subcatchments, the hydrogeochemical characteristics as depicted in the Piper diagram (Figure 36) are as follows:

Cation Ternary Plot: Sampling points S4, S6, S9, S10, S8, and S18 fall within the mixed field, indicating a complex geochemical environment with no dominant cation. The remaining sampling points are located within the calcium field, suggesting a significant influence of calcium-rich minerals.

Anion Ternary Plot: Point S4 is located in the sulfate field. Points S1, S2, and S8 are located in the bicarbonate field. Points S5, S13, S15, S16, S17, S18, and C1 are located in the chloride field. The remaining points are located in the mixed field.

Diamond plot:

- **Left Quadrant:** Sampling points S1, S2, and S8 are located in this quadrant.
- **Top Quadrant:** The remaining sampling points are located in this quadrant. Specifically, point S4 is located at a high position in this quadrant.

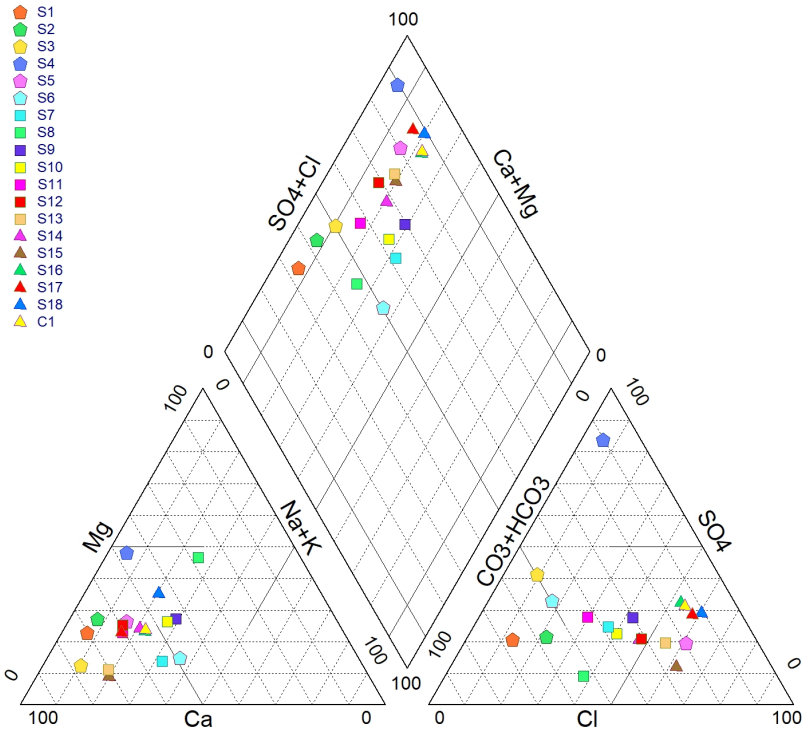


FIGURE 5.20: iper trilinear diagram summarizing the major-ion chemistry of groundwater samples from Ouled Saber subcatchment.

5.8.3 Discussion of Piper Diagram

Anini, Boussellam and Mkhalfa Subcatchments

The Piper diagram provides valuable insights into the geochemical processes influencing water chemistry in our study area. The dominance of calcium ions at most sampling points suggests that these locations have interacted more with formations containing limestone or clay or marl. Points A2 and A5 located in the sodium and potassium field could indicate potential influence from minerals rich in these elements or processes such as ion exchange, evaporation, or anthropogenic sources. In the anion ternary plot, points A2, B2, and B8 could indicate the influence of sulfate-rich minerals or anthropogenic sources. Points B7 and M3 suggest potential influences such as sea water intrusion, dissolution of halite, or anthropogenic sources.

The distribution of sampling points within the diamond plot of the Piper diagram for the Anini, Boussellam, and Mkhalfa subcatchments is as follows:

- **Left Quadrant:** Sampling points A1, A3, A4, B1, B3, B4, B6, and M2 suggest that these waters are primarily influenced by calcium and bicarbonate ions. This could indicate interaction with carbonate-rich minerals such as limestone or dolomite.
- **Bottom Quadrant:** Contains only one sampling point, A5. This water sample is primarily influenced by sodium + potassium and bicarbonate + carbonate ions. Given its location in gray marl and limestone bedded at the summit, it suggests a significant interaction with these alkaline minerals.
- **Right Quadrant:** There is only one sampling point, A2. This water sample is primarily influenced by sodium + potassium and chloride ions. Given its location near a road where salt is used for de-icing in winter, this could be a result of road salt runoff rather than sea water intrusion.
- **Top Quadrant:** The remaining sampling points located in this quadrant, which indicate a dominance of calcium + magnesium and sulfate + chloride ions, could suggest more complex geochemical interactions. This may imply that the groundwater at these locations has interacted with multiple geological formations during its flow path, leading to the dissolution of a variety of minerals.

Saber Subcatchment

The distribution of sampling points within the Piper diagram suggests distinct hydrogeochemical characteristics for both the Saber catchments and subcatchment.

- **Cation Ternary Plot (Saber Catchments):** In the cation ternary plot for Saber catchments, the presence of sampling points within the mixed field indicates a complex geochemical environment with no dominant cation. This could be due to a variety of factors such as weathering of different rock types or anthropogenic influences. In contrast, other sampling

points are located within the calcium field, suggesting a significant influence of calcium-rich minerals such as limestone or dolomite. This is due to the underlying geology of these areas which is rich in these minerals.

- **Anion Ternary Plot (Saber Catchments):** In the anion ternary plot for Saber catchments, point S4 is located in the sulfate field which indicates the influence from sulfate-rich minerals situated in the geological formation E 1,2. Points S1, S2, and S8 are located in the bicarbonate field which suggests significant influence from carbonate-rich minerals or biological processes that produce bicarbonate ions. Points in the chloride field could be indicating influences such as human activities or dissolution of halite.
- **Diamond Plot:** In the Saber subcatchment, sampling points in the left quadrant suggest that these waters are primarily influenced by calcium and bicarbonate ions, which could indicate interaction with carbonate-rich minerals such as limestone or dolomite. The remaining sampling points in the top quadrant indicate a dominance of calcium and sulfate ions which could suggest influence from gypsum dissolution or other sulfate-rich minerals.

These interpretations provide valuable insights into the hydrogeochemical processes occurring within these areas. However, these interpretations are based on general principles and may not fully capture the complexity of these specific areas. Further investigation involving more detailed geochemical analysis and an understanding of local geological and climatic conditions would provide a more comprehensive understanding of their hydrogeochemistry.

5.8.4 Schoeller-Berkaloff Diagram Results

In our study, we have used the Schoeller-Berkaloff diagram to analyze and discuss the hydrogeochemical processes and geological influences within our study area. Our discussion is based on the observed patterns in various ion ratios in water samples, which provide valuable insights into the extent of interaction between groundwater and geological formations such as marl, clay, conglomerates, or limestone. We have also considered the influence of human activities, such as industrial processes or agricultural practices, on the geochemical characteristics of water samples. Our discussion further extends to the interpretation of these observations in the context of groundwater flow direction, as indicated by the piezometric map.

In the following sections, we present our results and discuss our interpretations based on the Schoeller-Berkaloff diagram:

- **The Upper Part:** In the northern region as shown in Figure5.21, most sampling points generally exhibit lower ion concentrations. Specifically, the concentrations do not exceed 50 mg/L for magnesium (Mg^{2+}), 40 mg/L for sodium + potassium (Na+K), 80 mg/L for chloride (Cl^{-}), and 100 mg/L for sulfate (SO_4^{2-}). However, there is a high concentration of calcium (Ca^{2+}) and bicarbonate (HCO_3^{-}) ions. There are exceptions.

Specifically, sampling points A2, A4, A5, B2, B5, S3, and S4 show elevated concentrations of certain ions compared to other northern sampling points. These elevated concentrations are not uniform across all ions but are specific to certain ones. For instance, some of these sampling points exhibit higher concentrations of sulfate, while others show elevated levels of sodium + potassium, and yet others have increased levels of calcium and magnesium. Sampling point S4, situated in the E1,2 formation, demonstrates distinct hydrogeochemical characteristics. Despite being in a recharge zone, it presents higher ion concentration, hardness, and elevated levels of sulfate. Sampling points A2 and A5 exhibit elevated concentrations of sodium and potassium, possibly due to anthropogenic activities such as the use of fertilizers or road salting. Similarly, S4 also shows a higher concentration of sodium and potassium indicative of salinization. Sampling points M1 and A6 represent a transition in ion concentration in the northern part. They exhibit higher ion concentrations compared to other northern sampling points, indicating the beginning of a new ion concentration regime.



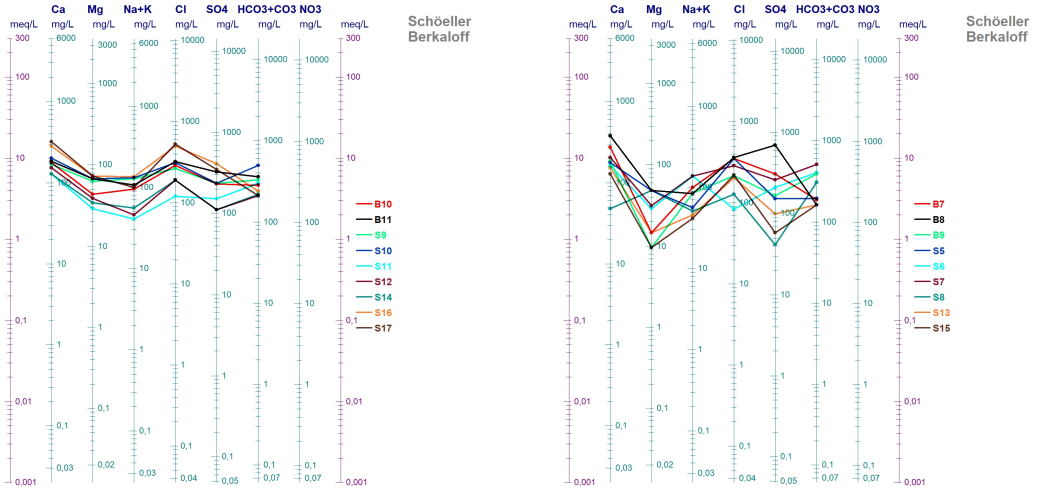
(a) Part 1 (b) Part 2

FIGURE 5.21: Schoeller–Berkaloff diagrams of major-ion concentration profiles for the northern sector.

– **The Middle Part:** The middle part of the study area as shown in Figure5.22 is characterized by higher ion concentrations compared to the northern region, where the groundwater flow originates. The ion concentrations in this middle region vary as follows:

  * Calcium (Ca^{2+}): Ranges from 110 mg/L to 450 mg/L.
  * Magnesium (Mg^{2+}): Ranges from 30 mg/L to 80 mg/L.
  * Sodium + Potassium (Na+K): Ranges from 40 mg/L to 150 mg/L.
  * Sulfate (SO_4^{2-}): Ranges from 100 mg/L to 400 mg/L.
  * Bicarbonate (HCO_3^-): Exceeds 200 mg/L and can reach up to 500 mg/L.

However, there are exceptions. Specifically, sampling points B7, B8, B9, S5, S6, S7, S8, S13, and S15 show variations in ion concentrations compared to other sampling points in the middle part. Some of these points exhibit elevated concentrations of certain ions, while others show lower concentrations. The sampling points B7, B9, S13, and S15 are rich in calcium (Ca^{2+}) but poor in magnesium (Mg^{2+}). Sampling point B8 shows a high sulfate (SO_4^{2-}) concentration. Sampling points S6 and S7 are rich in sodium + potassium. Sampling point S5 shows a high chloride (Cl^-) concentration. Sampling point S8 is rich in magnesium (Mg^{2+}) but poor in sulfate (SO_4^{2-}) and calcium (Ca^{2+}).



(a) Part 1 (b) Part 2

FIGURE 5.22: Schoeller–Berkaloff diagrams of major-ion concentration profiles for the middle sector.

* **The Lower Part:** Situated in the south around the main stream with a Strahler order of 6, this area has experienced extensive interaction with various sources during its flow from the north to the south. The highest ion concentrations are observed in this part qs shown in Figure 5.23, with high ion concentrations recorded at sampling points M3, S18, and C1.

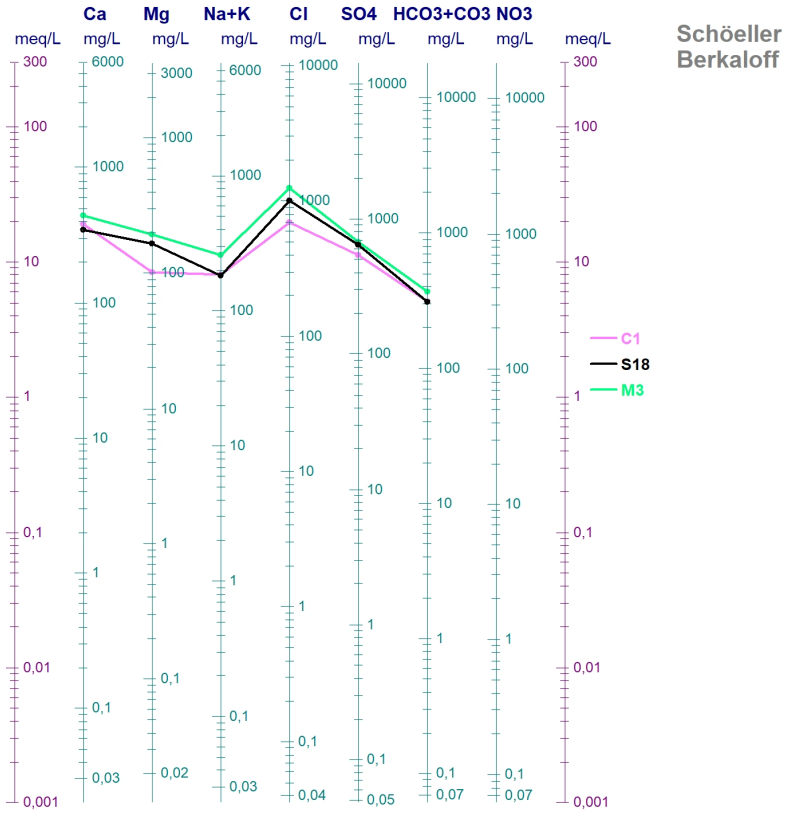


FIGURE 5.23: Schoeller–Berkaloff diagram of major-ion concentration profiles for the lower sector.

5.8.5 Schoeller-Berkaloff Diagram Discussion

* **Upper Part:**
  This geochemical signature can be attributed to the presence of geological formations such as K2 5-6 and K2 3-6, which predominantly contain limestone. Limestone, primarily composed of calcium carbonate ($CaCO_3$), can dissolve in water, leading to an increase in hardness and the bicarbonate ion concentration. The extensive surface area of these formations in the northern region compared to the middle and southern parts suggests a greater influence on the groundwater chemistry in this area. The dissolution of limestone increases the concentration of Ca^{2+} and HCO_3^- ions, which is consistent with the observed high concentrations at these sampling points.
  These observations highlight the significant role that geological formations play in influencing groundwater chemistry. The specific mineral composition of these formations, such as the presence of limestone, can lead to distinct ion profiles in the groundwater. The E1,2 formation comprises limestone with flint and marly limestone, occasionally with gypsum. The dissolution of these minerals can significantly influence the groundwater chemistry. Limestone can dissolve in water to increase hardness and bicarbonate ion concentration. The presence of gypsum can lead to an increase in both

calcium and sulfate ions. The presence of only one sampling point from this geological formation across the study area suggests that it has low permeability.

The elevated sulfate concentrations observed in sampling points A2, A4, S3, B2, and B5 could be attributed to the interaction with the E1,2 geological formation. Moreover, these points are located within an agricultural area where the use of fertilizers containing sulfate and sodium is common. The leaching of these fertilizers into the groundwater can further contribute to the high sulfate and sodium levels observed. The elevated concentrations of sodium (Na) and potassium (K) at sampling points A2 and A5 could be due to anthropogenic activities such as the use of fertilizers or road salting.

* **Middle Part:**
These observations highlight the significant spatial variability in groundwater chemistry across the study area. The variations in ion concentrations at specific sampling points could be influenced by various factors such as local geological formations, groundwater flow paths, and human activities.

The elevated calcium at sampling points B7, B9, S13, and S15 could be indicative of specific industrial processes or waste that affect the groundwater chemistry. Certain industries may use chemicals that contain calcium or influence its concentration in the groundwater. As shown in Figure 39, these sampling points are located in an industrial zone.

The high sulfate concentration at sampling point B8 could be a result of industrial activities that release sulfate-rich waste, which can leach into the groundwater and increase sulfate concentrations. It could also be due to fertilizers as it is close to an agricultural area.

The high sodium + potassium at sampling points S6 and S7 could be due to the use of fertilizers or salts in the agricultural practices in this area. The high chloride concentration at sampling point S5 could be due to urban areas producing a significant amount of wastewater, which can contain high levels of chloride. If this wastewater infiltrates into the groundwater, it can increase the chloride concentration.

The high magnesium but low sulfate and calcium at sampling point S8 could be due to the presence of conglomerates and clay in the MPl geological formation which could influence the groundwater chemistry.

These observations highlight the diverse ion profiles across these specific sampling points and how they can be influenced by both geological formations and human activities.

* **Lower Part:**
An area where groundwater has had extensive interaction with various geological formations during its flow from the north to the south. Human activities could also contribute to the elevated ion concentrations. Activities such as agriculture, industry, or waste disposal can introduce various ions into the groundwater system. This interaction can significantly influence the groundwater chemistry, leading to high ion concentrations.

These observations highlight the importance of understanding both natural processes, such as groundwater flow and geochemical interactions, and anthropogenic influences when interpreting hydrogeochemical data.

5.8.6 Wilcox and Riverside Diagrams

Graphical representations of water quality data are essential tools for interpreting the complex relationships between water chemistry and various influencing factors. Among these graphical tools, Riverside and Wilcox diagrams are widely used to assess the suitability of water for irrigation purposes.

Riverside Diagram

* **Riverside:** The Riverside diagram is a graphical representation that classifies water based on its salinity hazard and sodium hazard. Salinity hazard is represented by the electrical conductivity (EC) of the water, while sodium hazard is represented by the Sodium Adsorption Ratio (SAR). The diagram divides water into four categories: low salinity – low sodium, medium salinity – low sodium, high salinity – medium sodium, and very high salinity – high sodium. This classification helps in determining the suitability of water for irrigation in different types of soil.

Wilcox Diagram

* **Wilcox:** The Wilcox diagram classifies irrigation water based on its salinity (measured as total dissolved solids or electrical conductivity) and its relative sodium content (expressed as a percentage of total cations). The diagram categorizes water into nine classes ranging from excellent to unsuitable for irrigation. This classification provides a quick assessment of the potential risk of soil degradation due to the use of the water for irrigation.

Riverside Results

As shown in Figure 5.24, the Riverside hydrochemical polygon diagrams depict major-ion facies for our study area.

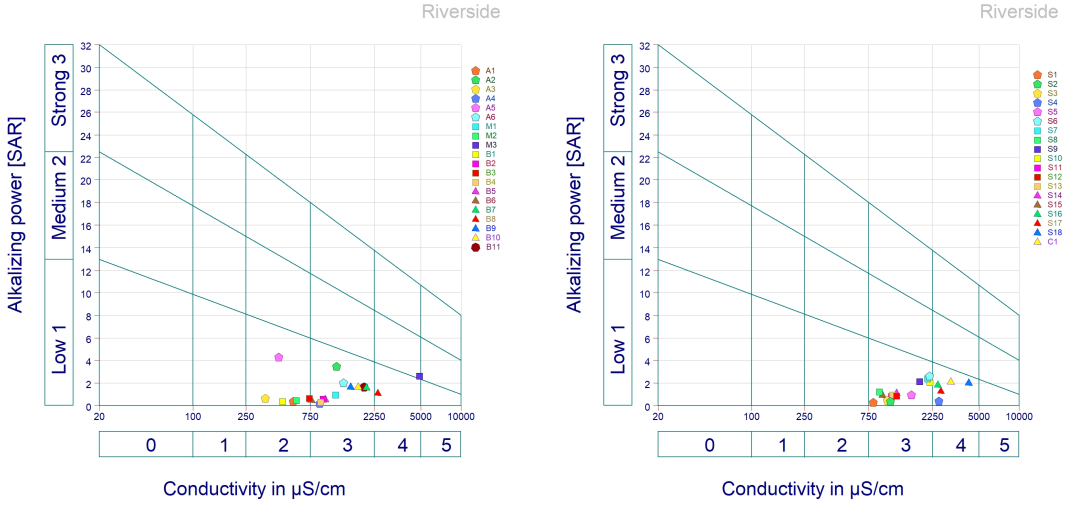
– **Based on the Riverside diagram analysis for the Anini, Boussellam, and Mkhalfa subcatchments**: As shown in Figure5.24a:

  * For the Sodium Adsorption Ratio (SAR), all of the sampling points are situated in the “low” category, indicating a low sodium hazard. However, there is one exception: sampling point M3 is situated in the “medium” category, indicating a higher risk of sodium accumulation.
  * For Electrical Conductivity (EC), which represents salinity hazard:
    · Sampling points M3 and B8 are situated at an EC value of 4.

- Sampling points A1, A3, A5, M2, B1, and B3 are situated at an EC value of 2.
- The rest of the sampling points are situated at an EC value of 3.

– **Based on the Riverside diagram analysis for the Ouled Saber subcatchments:** As shown in Figure5.24b:

* For SAR, all of the sampling points are situated in the "low" category.
* For EC:
  - Sampling points S4, S16, S17, S18, and C1 are situated at an EC value of 4.
  - The rest of the sampling points are situated at an EC value of 3.



(A) western Subcatchments.

(B) Ouled saber subcatchment.

FIGURE 5.24: Riverside hydrochemical polygon diagrams.

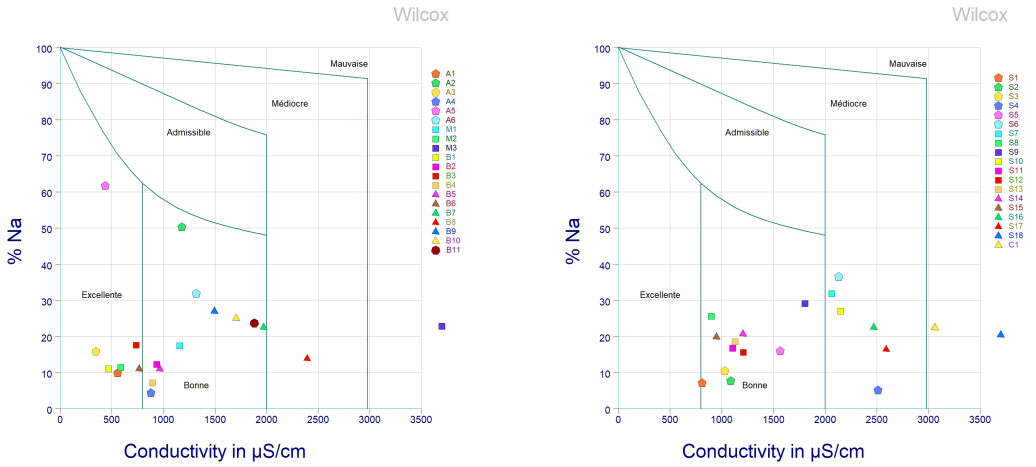
Wilcox Results

The Wilcox diagram classifications indicate varying levels of irrigation suitability based on sodium percentage (Na%) and electrical conductivity (EC), as shown in Figure 5.25.

– **Based on the Wilcox diagram analysis for the Anini, M'khalfa and Boussellam subcatchments (Figure 5.25a):**

* **For the percentage of sodium ions (Na%) and EC:**
  - Sampling points A1, A3, A5, B1, B3, B6 and M2 are situated in the "excellent" zone.
  - The remaining sampling points are situated in the "good" zone.
  - Sampling point B8 is situated in the "doubtful" zone.
  - Sampling point M3 is situated in the "unsuitable" zone.

- **Based on the Wilcox diagram analysis for the Ouled Saber subcatchment (Figure 5.25b):**
  - **For the percentage of sodium ions (Na%) and EC:**
    - Sampling points S18 and C1 are situated in the "unsuitable" zone.
    - Sampling points S17, S16, S4, S10, S7 and S6 are situated in the "doubtful" zone.
    - The remaining sampling points are situated in the "good" zone.



(A) Eastern subcatchments. (B) Ouled Saber subcatchment.

FIGURE 5.25: Wilcox diagrams of groundwater quality for (A) The Eastern subcatchments and (B) Ouled Saber subcatchment.

Discussion – Riverside

- These results provide valuable insights into the suitability of water from these subcatchments for irrigation.
- The low sodium hazard suggests that these water samples have a low concentration of sodium ions relative to calcium and magnesium ions, which is generally good for irrigation as it reduces the risk of sodium accumulation in the soil. However, sampling point M3 shows a higher risk of sodium accumulation.
- The EC values suggest varying levels of salinity hazard. Sampling points M3 and B8 show a relatively high salinity hazard, which can be harmful for many crops as it can decrease soil permeability and available water, inhibit seed germination, and reduce crop yield.
- Sampling points A1, A3, A5, M2, B1, and B3 indicate a moderate salinity hazard.

- In the Ouled Saber subcatchments, all sampling points show a low sodium hazard. However, sampling points S4, S16, S17, S18, and C1 show a relatively high salinity hazard while the rest indicate a moderate salinity hazard.
- The implications of these observations are significant for both environmental management and agricultural practices in the study area.

Discussion – Wilcox

- In the Anini, Mkhalfa, and Boussellam subcatchments, most sampling points fall into the "excellent" or "good" zones, suggesting suitability for most types of crops and soils.
- However, sampling point B8 falls into the "doubtful" zone and M3 into the "unsuitable" zone, indicating potential problems with certain crops and soils due to higher sodium percentage or salinity.
- In the Ouled Saber subcatchments, while most sampling points fall into the "good" zone indicating general suitability for irrigation, several points fall into the "doubtful" or "unsuitable" zones. This suggests that water from these points may cause problems with certain crops and soils due to higher sodium percentage or salinity.

5.8.7 Other Implications of Hydrochemical Sampling

Prior to detailed hydrochemical analyses, we conducted in situ measurements of total dissolved solids (TDS) on 44 groundwater samples—using a calibrated portable conductivity/TDS meter and a stratified sampling design to ensure uniform spatial coverage. Groundwater recharge potential often correlates inversely with solute concentration. These field-measured TDS values now serve as an independent validation tool for our groundwater-recharge potential zones model. In Chapter 6, the TDS dataset will play a role of a validation tool compared against the GIS-based weighted-overlay output to confirm the spatial plausibility of predicted recharge zones.

5.9 Conclusion

This study has successfully employed a comprehensive and rigorous methodology to investigate the subsurface hydrogeological characteristics of the northern part of the upper Boussellam. By combining a detailed piezometric survey with an extensive hydrochemical analysis, we have developed a holistic understanding of the groundwater system in the region. The piezometric survey conducted across 120 strategically located boreholes, analyzed using QGIS and the Thin Plate Spline method, provided valuable insights into the spatial distribution of the piezometric head. Meanwhile, the hydrochemical analysis of samples from 39 distinct locations, visualized with Inverse Distance Weighting in QGIS, revealed critical variations in the concentration of seven key ions.

The application of statistical tools, such as correlation matrix and linear regression, allowed us to discern relationships between ion concentrations, thereby

elucidating the underlying geochemical processes. Further, the use of Piper, Schoeller-Berkaloff, Riverside, and Wilcox diagrams, along with ionic ratio analysis, provided an integrated view of the water's chemical composition, its flow path interactions, and its suitability for irrigation.

In conclusion, this hydrogeochemical investigation represents a significant contribution to our understanding of groundwater quality in the study area. The findings have far-reaching implications for water resource management, environmental stewardship, and public health. Nonetheless, future studies could build on this work by addressing temporal variations and exploring additional parameters to refine groundwater management strategies. This work underscores the importance of employing robust, integrative methodologies in hydrogeological research to generate actionable insights. In the following chapter, we will employ remote sensing using Landsat imagery to assess land use and land cover classification in our region and to extract lineaments. This analysis will further enhance our understanding of the structural and surface controls on the groundwater system, providing additional context for our hydrogeochemical findings.

Chapter 6

Modeling Groundwater Recharge Potential Zones

6.1 Abstract

This chapter presents a GIS-based multi-criteria model to delineate groundwater-recharge potential in the northern Upper Boussellam. Six spatial layers —slope, Drainage density, land use/land cover (LULC), Lineament density, Precipitation and Lithology values— were reclassified on a 1–10 scale and weighted via the Analytic Hierarchy Process. A weighted-overlay of these factors produces recharge-potential classes (very low to very high). Model performance was independently validated using in situ total dissolved solids (TDS) measurements and ROC-curve analysis, yielding an AUC of 0.838. The results reveal spatially coherent recharge corridors in the north-central massifs and extensive low-potential areas in the south. This integrated framework offers a robust, transferable tool for targeting groundwater-harnessing and conservation efforts in semi-arid regions.

6.2 Introduction

Groundwater is a critical freshwater reserve, particularly in semi-arid regions where surface water is limited and climatic variability intensifies scarcity (Jaafarzadeh et al., 2021; Rahmani et al., 2017; Stigter et al., 2023). In areas like the northern Upper Boussellam, escalating pressures from urbanization, agriculture and industry have led to overexploitation and degradation of groundwater, threatening long-term water security and ecosystem sustainability (Boulgueraguer et al., 2018; Chennafi, 2012).

Recharge—the downward movement of water from the surface through the unsaturated zone—is a key process for sustaining aquifer systems (Andualem & Demeke, 2019; Ghazavi et al., 2018; Yeh et al., 2016). Its occurrence is governed by multiple variables, including precipitation, slope, drainage characteristics, geological structure and land use (Ajami, 2021). Recognizing and quantifying recharge potential is therefore crucial for guiding groundwater development and safeguarding quality (Jaafarzadeh et al., 2021; Megdal, 2018).

This study integrates spatial and decision-support tools to delineate recharge potential zones. Specifically, we employ:

- Geographic Information Systems (GIS) to process, overlay and classify spatial datasets (Thakur et al., 2017).
- Remote Sensing for thematic layer derivation (e.g., LULC, lineaments).
- The Analytic Hierarchy Process (AHP) for assigning weights to six key recharge drivers: slope, drainage density, LULC, lineament density, precipitation and hydrochemical (TDS) concentration.
- Receiver Operating Characteristic (ROC) analysis—based on in situ TDS measurements—to validate the spatial realism of the model output (Aissaoui et al., 2023; Dar et al., 2021).

Our primary goal is to produce a recharge potential map distinguishing harnessing-prone zones from those needing conservation. Secondarily, we propose a novel validation mechanism that links hydrochemical dilution (via TDS) to spatial recharge patterns.

By developing and validating this integrated approach, the chapter contributes a robust, transferable methodology for sustainable groundwater resource planning in semi-arid settings like the Setifian High Plateaux.

6.2.1 Review of Literature

Groundwater recharge—the process by which water percolates through the unsaturated zone to replenish aquifers—is central to sustainable groundwater management, particularly in semi-arid regions (Hasan et al., 2023; Shapiro & Day-Lewis, 2021). Despite its importance, accurately estimating recharge remains a complex task due to data limitations and the heterogeneity of hydrological systems (Healy & Cook, 2002; Sajil Kumar et al., 2021).

Several approaches have been developed to quantify recharge, each with strengths and constraints. Water balance methods provide broad estimates but lack spatial detail. Tracer and unsaturated zone methods offer local insights but are data- and equipment-intensive (Goldscheider et al., 2008; Karamouz et al., 2022). Groundwater modeling and advanced statistical approaches provide dynamic analysis yet depend on many assumptions and parameter sensitivities (Collenteur et al., 2021; Parveen et al., 2023).

Given these challenges, GIS-based methods have gained prominence for delineating recharge zones. By integrating spatial datasets—such as slope, lineaments, LULC, and rainfall—within a multi-criteria decision-making (MCDM) framework, recharge-prone areas can be effectively identified (Arulbalaji et al., 2019; Thakur et al., 2017). Among the various MCDM techniques, the Analytic Hierarchy Process (AHP) remains widely adopted for its transparency and structured weighting system (Dar et al., 2021; Owolabi et al., 2020).

Although AHP has been criticized for its subjectivity (Zarour et al., 2019), comparative studies in Tunisian basins report that it often yields more consistent results than other MCDM tools, such as the Multi Influencer Factor (MIF) method (Missaoui et al., 2023; Zghibi et al., 2020). In our approach, we prioritized precipitation as the most influential factor—supported by several studies (Castillo et al., 2021; Kim & Jackson, 2012)—followed by lithology, slope, lineament density, LULC and drainage density.

To validate the spatial model, Receiver Operating Characteristic (ROC) analysis was combined with in situ measurements of total dissolved solids (TDS) from shallow wells. TDS levels, especially after the recharge season, offer practical insight into recharge efficiency and water quality. This validation approach adds robustness and affordability, particularly in data-scarce environments.

Overall, the integration of GIS, AHP and TDS-based validation provides a scalable framework for assessing groundwater recharge potential with both scientific rigor and practical relevance.

6.3 Methodology

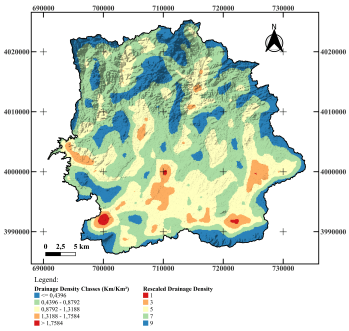
To delineate groundwater recharge potential zones with high spatial precision, we used QGIS to preprocess, integrate and analyze six thematic layers derived from preceding chapters. These layers include: slope, drainage density, lithology (interpreted from a regional geological map), precipitation intensity, lineament density, and land use/land cover (LULC). Each input layer was first reclassified into thematic classes according to its influence on groundwater recharge, and rescaled on a 1–10 suitability scale, where higher values represent greater favorability for recharge.

To determine the relative contribution of each layer, the Analytic Hierarchy Process (AHP) was employed. Pairwise comparisons were made among the six factors to generate a normalized weight matrix, from which a consistency ratio (CR) was calculated to ensure logical coherence of the judgments. The finalized weights were then applied to each reclassified raster layer. A weighted overlay function was used to compute the final groundwater recharge potential map using the equation:

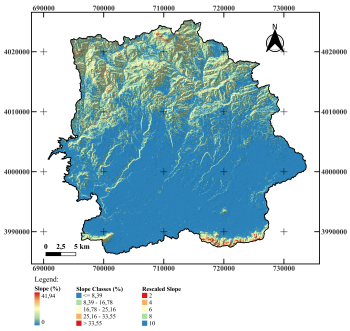
$$\text{GRPZ} = \sum_{i=1}^{6} W_i \times R_i \tag{6.1}$$

where W_i denotes the weight assigned to the i^{th} factor, and R_i is the reclassified raster score.

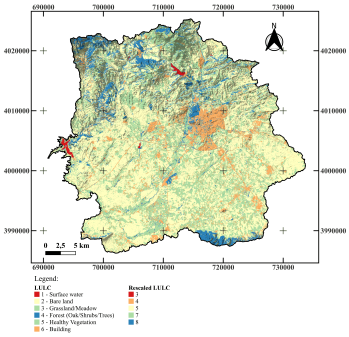
For model validation, total dissolved solids (TDS) values from 44 spatially distributed boreholes were used as an independent metric. A Receiver Operating Characteristic (ROC) analysis was performed by cross-referencing the recharge potential class at each well location with its corresponding TDS value. The resulting Area Under the Curve (AUC) score provides a quantitative measure of model performance and classification accuracy. As a result, each thematic layer was reclassified and rescaled on a 1–10 suitability scale according to its relative influence on groundwater recharge (higher values indicate greater contribution). Figure 6.1 presents the six rescaled maps in three rows.



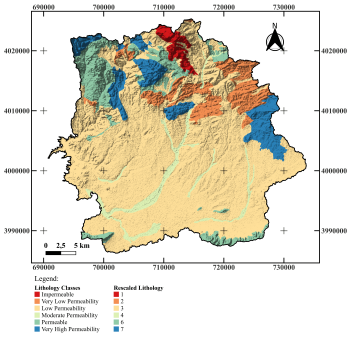
(A) Drainage density



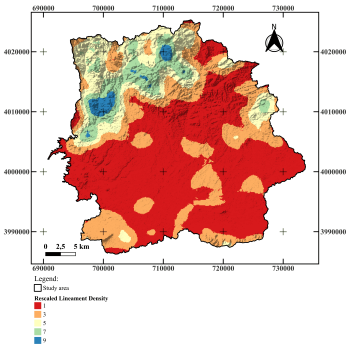
(B) Slope



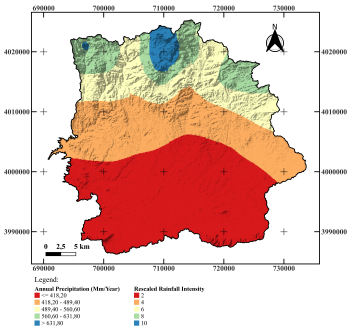
(C) LULC



(D) Lithology



(E) Lineament density



(F) Precipitation intensity

FIGURE 6.1: Thematic layers rescaled on a 1–10 scale according to their contribution to groundwater recharge: (a) drainage density; (b) slope; (c) LULC; (d) lithology; (e) lineament density; (f) precipitation intensity.

6.3.1 Rating Maps using AHP

Weights for each thematic layer were derived via pairwise comparisons in AHP and normalized to ensure consistency (CR < 0.10). Following Khemmal et al. (2025), the final groundwater-recharge potential index (GWRZ) was calculated in QGIS by the raster calculator as:

$$GWRZ = 0.3631\,R_w + 0.2163\,L_w + 0.1256\,S_l + 0.1558\,L_d + 0.0873\,\mathrm{LULC} + 0.0518\,D_d \tag{6.2}$$

The resulting recharge-potential map is presented in Figure 6.2.

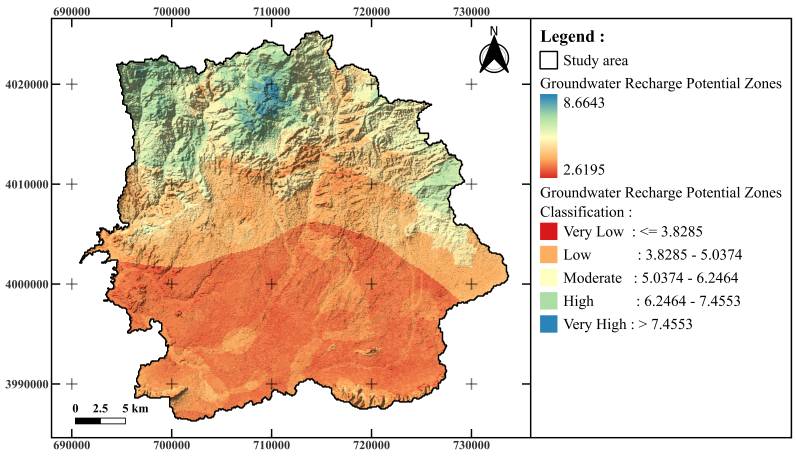


FIGURE 6.2: Groundwater-Recharge Potential Zone classes map (GWRPZ), generated via the AHP-weighted overlay (Eq. 6.2). Source: Khemmal et al. (2025)

The GWRPZ map (Figure 6.2) shows that the highest recharge potential is concentrated in the northern mountainous sectors, where gentle slopes, dense lineaments and higher precipitation coincide. Intermediate (moderate) potential zones form a transitional belt around these uplands, while the lowest potential areas dominate the southern lowlands, characterized by steeper slopes, sparse structures and reduced rainfall.

6.3.2 Validation of the Model

In this study, 44 spatially distributed TDS measurements (Fig. 6.3) were used to validate the recharge-potential model.

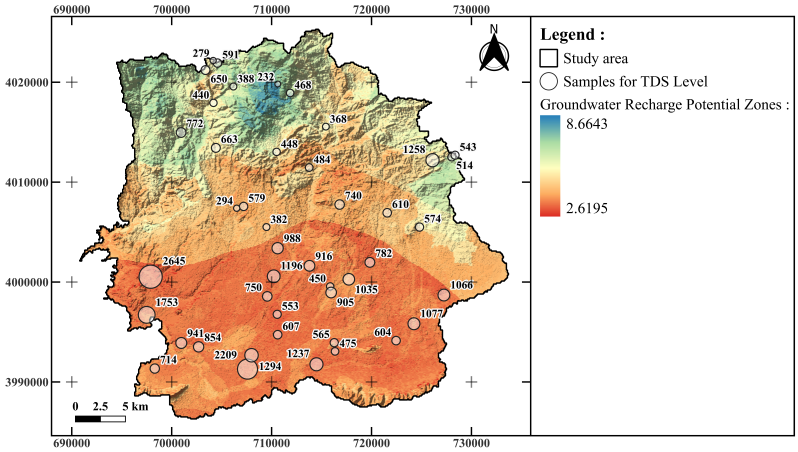


FIGURE 6.3: Spatial distribution of TDS sampling points overlaid on the groundwater recharge potential zones map. Source: (Khemmal et al., 2025)

The ROC analysis (Fig. 6.4) returned an AUC of 0.835 (SE = 0.064, $p < 0.001$; 95 % CI: 0.711–0.960), indicating excellent discrimination between high and low recharge zones. Classifier metrics further support model performance: a Gini index of 0.671 and a maximum K–S statistic of 0.650 at a TDS cutoff of 688.5 mg L^{-1} confirm the model's strong ability to separate recharge-rich from recharge-poor areas.

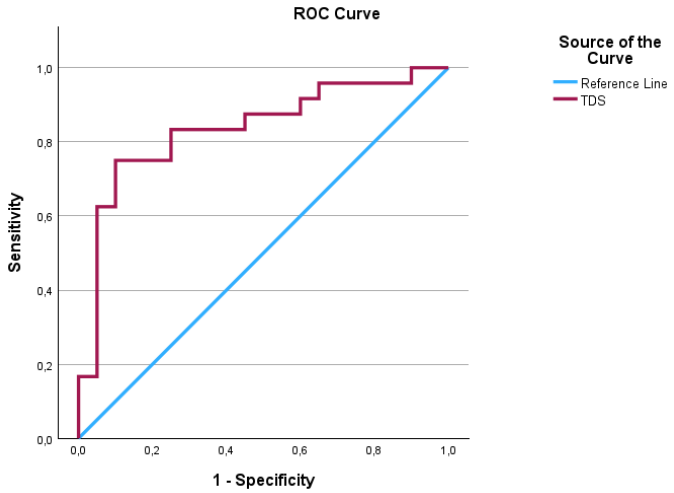


FIGURE 6.4: Receiver Operating Characteristic (ROC) curve for the groundwater recharge potential zones model, illustrating classification performance. Source: Khemmal et al. (2025)

6.4 Discussion

Our integrated workflow builds on the groundwork laid in earlier chapters: Chapter 1's geological mapping defined lithological controls; Chapter 2's DEM analysis quantified drainage density and slope influences; Chapter 3's climate assessment characterized rainfall distribution and established the recharge onset; Chapter 4's hydrochemical study and TDS sampling supplied a novel validation metric; and Chapter 5's Landsat-derived LULC map captured surface cover at the start of recharge. Together, these elements feed into the GIS–AHP model and ROC-based validation presented here.

This work synthesizes insights from preceding chapters—geospatial data preparation, hydrochemical characterization, and LULC mapping—to deliver a holistic recharge-potential assessment. By integrating slope, drainage density, lithology, precipitation, lineament density and LULC in a GIS–AHP framework, we have produced a spatially coherent recharge potential map validated by TDS-based ROC analysis.

Key findings align with known hydrogeological patterns: the northern highlands, underpinned by karstified limestone, dense fractures and elevated rainfall, exhibit the greatest recharge potential, while southern lowlands remain recharge-limited by lower precipitation and less permeable strata. Intermediate zones capture transitional conditions where topography and land cover moderate infiltration.

The use of NASA–POWER precipitation data (Chapter 3) addressed gaps in local rainfall records, refining the weight assigned to rainfall and enhancing model reliability. Similarly, LULC patterns captured via November Landsat 8 imagery (Chapter 4) ensured that surface conditions at recharge onset were accurately represented. Hydrochemical sampling and TDS analysis (Chapter 5) provided an independent metric for model validation, yielding an AUC of 0.835, Gini index of 0.671 and K–S statistic of 0.650, confirming the model's discriminative power.

Practically, this approach offers a replicable workflow for semi-arid regions: • Water-managers can target high-potential zones for managed aquifer recharge or conservation easements, while low-potential sectors warrant stricter abstraction controls and pollution safeguards. • The integration of readily available remote sensing and TDS data makes the methodology accessible for data-scarce contexts. • ROC-based validation using chemical proxies introduces a robust, low-cost alternative to gauge recharge dynamics where hydrometric data are lacking.

Collectively, the chapters converge to deliver a decision-support tool that not only pinpoints recharge hotspots but also embeds quality checks through hydrochemistry. This fusion of geospatial analysis and field-based validation sets a new standard for groundwater-recharge studies in semi-arid plateaux.

6.5 Conclusion

6.6 General Conclusion

This study has delivered a fully integrated, GIS-based framework for understanding and managing water resources in the Northern Upper Boussellam catchment. By leveraging a 30 m ASTER GDEM v3, we hydro-conditioned the terrain to extract a Strahler-ordered stream network, delineate sub-catchments, and compute key indices—drainage density and slope gradient—each optimized through separate workflows. These morphometric layers, together with relief and areal parameters (form factor, infiltration number, ruggedness), revealed dominant subsurface flow, zones of preferential infiltration, and areas prone to concentrated runoff and erosion.

Concurrently, hydroclimatological analysis of NASA-POWER precipitation (347–703 mm yr^{-1}) and temperature records (mean 13.5 °C) defined semi-arid to sub-humid regimes across sub-catchments and identified the annual recharge window. This timing guided targeted LULC mapping using multi-temporal Landsat 8 OLI/TIRS imagery— classified via maximum-likelihood—to capture phenological stages critical for assessing surface conditions during recharge periods.

Together, these datasets underpin a recharge-potential model that prioritizes high-infiltration zones, informs piezometric and hydrochemical sampling, and supports sustainable land-and-water management. The reproducible, DEM-driven approach can be readily transferred to other small-scale basins, offering a robust decision-support tool for semi-arid regions facing climate variability and growing water demands.

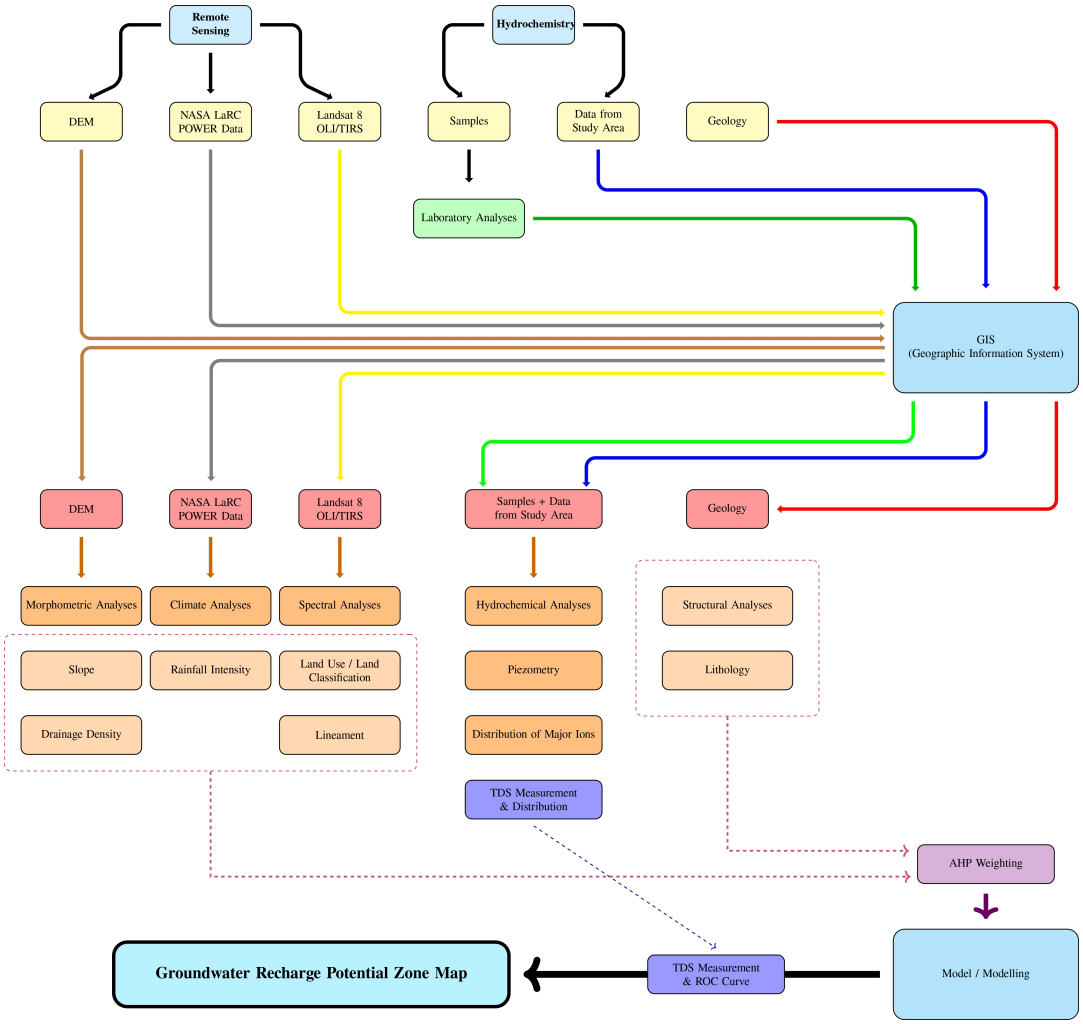


FIGURE 6.5: Modeling Groundwater Recharge Potential Zone across Remote Sensing, GIS, and Hydrochemistry: integrated framework with AHP and validation.

Bibliography

Aissaoui, M., Maizi, D., Benhamza, M., Azzouz, K., Belaroui, A., & Bengusmia, D. (2023). Identification and mapping of potential recharge in the middle seybouse sub-catchment of the guelma region (north east of algeria): Contribution of remote sensing, multi-criteria analysis, roc-curve and gis. *Acque Sotterranee-Italian Journal of Groundwater*, *12*(1), 25–37.

Ajami, H. (2021). Geohydrology: Groundwater. In *Encyclopedia of geology* (2nd ed., pp. 408–415, Vol. 6). Elsevier. https://doi.org/10.1016/B978-0-12-409548-9.12388-7

Andualem, T. G., & Demeke, G. G. (2019). Groundwater potential assessment using gis and remote sensing: A case study of guna tana landscape, upper blue nile basin, ethiopia. *Journal of Hydrology: Regional Studies*, *24*, 100610.

Anhurt, F. (1970). Functional relationship between denudation, relief and uplift in large, mid-latitude drainage basins. *American Journal of Science*, *268*, 243–263.

Arulbalaji, P., Padmalal, D., & Sreelash, K. (2019). Gis and ahp techniques based delineation of groundwater potential zones: A case study from southern western ghats, india. *Scientific reports*, *9*(1), 2082.

Bogale, A. (2021). Morphometric analysis of a drainage basin using geographical information system in gilgel abay watershed, lake tana basin, upper blue nile basin, ethiopia. *Applied Water Science*, *11*, 122.

Boulaacheb, N. (2010). Les paysages végétaux du djebel mégriss (tell septentrional, algérie) : Diversité des écosystèmes, richesse floristique, ampleur de l'anthropisation. *Physio-Géo*, *7*, 183–210. https://doi.org/10.4000/physio-geo.3187

Boulgueraguer, Z., Chaffai, H., Toumi, N., Saidi, S., Djorfi, & Djabri, L. (2018). Origin of mineralization and impact of anthropogenic pollution on water quality in boussellam wadi and its environment, wilaya of sétif (north-east algeria). *Journal of Biodiversity and Environmental Sciences*, *12*(6), 176–185.

Castillo, J. L. U., Ramos Leal, J. A., Martínez Cruz, D. A., Cervantes Martínez, A., & Marín Celestino, A. E. (2021). Identification of the dominant factors in groundwater recharge process, using multivariate statistical approaches in a semi-arid region. *Sustainability*, *13*(20), 11543.

Chennafi, H. (2012). Decadal evaluation of durum wheat water requirements to improve rainfed agriculture under semi-arid conditions. *Energy Procedia*, *18*, 896–904.

Chopra, R., Dhiman, R. D., & Sharma, P. K. (2005). Morphometric analysis of sub-watersheds in gurdaspur district, punjab using remote sensing and gis techniques. *Journal of the Indian Society of Remote Sensing*, *33*(4), 531–539.

Chorley, R. J. (1969). The drainage basin as the fundamental geomorphic unit. In R. J. Chorley (Ed.), *Introduction to fluvial processes* (pp. 30–52). Methuen & Co. Ltd.

Clarck, J. J. (1966). Morphometry from maps. In *Essays in geomorphology* (pp. 235–274). Elsevier.

Collenteur, R. A., Bakker, M., Klammler, G., & Birk, S. (2021). Estimation of groundwater recharge from groundwater levels using nonlinear transfer function noise models and comparison to lysimeter data. *Hydrology and Earth System Sciences*, *25*(5), 2931–2949.

Congedo, L. (2021). Semi-automatic classification plugin (scp): A python tool for the download and processing of remote sensing images in qgis. *Journal of Open Source Software*, *6*(64), 3378. https://doi.org/10.21105/joss.03378

Dar, T., Rai, N., & Bhat, A. (2021). Delineation of potential groundwater recharge zones using analytical hierarchy process (ahp). *Geology, Ecology, and Landscapes*, *5*(4), 292–307.

Davraz, A., & Batur, B. (2021). Hydrogeochemistry characteristics of groundwater and health risk assessment in yalvaç–gelendost basin (turkey). *Environmental Geochemistry and Health*, *43*(3), 1015–1037.

Elewa, H. H., Ramadan, E. M., & Nosair, A. M. (2016). Spatial-based hydromorphometric watershed modeling for the assessment of flooding potentialities. *Environmental Earth Sciences*, *75*, 906–926.

Faniran, A. (1968). The index of drainage intensity—a provisional new drainage factor. *Australian Journal of Science*, *31*, 328–330.

Gaussen, H., & Bagnouls, F. (1952). L'indice xérothermique [the xerothermic index]. *Bulletin de l'Association de géographes français*, *29*(222–223), 10–16.

Ghazavi, R., Babaei, S., & Erfanian, M. (2018). Recharge wells site selection for artificial groundwater recharge in an urban area using fuzzy logic technique. *Water resources management*, *32*, 3821–3834.

Goldscheider, N., Meiman, J., Pronk, M., & Smart, C. (2008). Tracer tests in karst hydrogeology and speleology. *International Journal of speleology*, *37*(1), 3.

Gregory, K. J., & Walling, D. E. (1973). *Drainage basin form and process: A geomorphological approach*. Edward Arnold.

Hasan, N., Pushpalatha, R., Manivasagam, V., Arlikatti, S., & Cibin, R. (2023). Global sustainable water management: A systematic qualitative review. *Water Resources Management*, *37*(13), 5255–5272.

Healy, R. W., & Cook, P. G. (2002). Using groundwater levels to estimate recharge. *Hydrogeology journal*, *10*, 91–109.

Horton, R. E. (1932). Drainage basin characteristics. *Transactions of the American Geophysical Union*, *13*, 350–361.

Horton, R. E. (1945). Erosional development of streams and their drainage basins: Hydrophysical approach to quantitative morphology. *Geological Society of America Bulletin*, *56*, 275–370.

Imran, A., Prabu, P., & Mithas, D. (2013). Erosion modeling in hard rock terrain using morphometry: A case study from tamilnadu, india. *Environmental Quality Management*, *23*(10).

Jaafarzadeh, M. S., Tahmasebipour, N., Haghizadeh, A., Pourghasemi, H. R., & Rouhani, H. (2021). Groundwater recharge potential zonation using an

ensemble of machine learning and bivariate statistical models. *Scientific Reports*, *11*(1), 5587.

JM, V. (1980). *The alpine chain of oriental algeria and the algerian-tunisian confines* [Doctoral dissertation, Pierre et Marie curie University, Paris VI].

Karamouz, M., Meidani, H., & Mahmoodzadeh, D. (2022). Inverse unsaturated-zone flow modeling for groundwater recharge estimation: A regional spatial nonstationary approach. *Hydrogeology Journal*, *30*(5), 1529–1549.

Khemmal, H. Y., Hani, A., & Benmarce, K. (2025). Exploring groundwater recharge potential zones mapping in the northern upper boussellam region: A novel approach integrating total dissolved solids levels. *Applied Water Science*, *15*(1), 103. https://doi.org/10.1007/s13201-025-02413-5

Kim, J. H., & Jackson, R. B. (2012). A global analysis of groundwater recharge for vegetation, climate, and soils. *Vadose Zone Journal*, *11*(1).

Kumar, P. J. S., Elango, L., & James, E. J. (2014). Assessment of hydrochemistry and groundwater quality in the coastal area of south chennai, india. *Arabian Journal of Geosciences*, *7*(10), 4293–4306.

Leopold, L. B., & Miller, J. P. (1956). Ephemeral streams: Hydraulic factors and their relation to the drainage network. *U.S. Geological Survey Professional Paper*, *282A*, 1–30.

Megdal, S. B. (2018). Invisible water: The importance of good groundwater governance and management. *NPJ Clean Water*, *1*(1), 15.

Mezrag, M. (2018). Modeling the impact of future climate change on wheat yield in the sétif region (algeria) under the a2 scenario. *Climate*, *10*(4), 50.

Miller, V. C. (1953). A quantitative geomorphic study of drainage basin characteristics in the clinch mountain area, virginia and tennessee. In C. N. O. (ed.) (Ed.), *Contributions to the geology of the southern appalachians* (pp. 1–30). Columbia University Press.

Missaoui, R., Abdelkarim, B., Ncibi, K., Gentilucci, M., Brahmi, S., Ayadi, Y., & Hamed, Y. (2023). Mapping groundwater recharge potential zones in arid region using remote sensing and gis perspective, central tunisia. *Euro-Mediterranean Journal for Environmental Integration*, *8*(3), 557–571.

Morisawa, M. E. (1962). Quantitative geomorphology of some watersheds in the appalachian plateau. *Geological Society of America Bulletin*, *73*, 1025–1046.

Nautiyal, M. D. (1994). Morphometric analysis of a drainage basin using aerial photographs: A case study of khairkuli basin, district dehradun, uttar pradesh. *Journal of the Indian Society of Remote Sensing*, *22*(4), 251–261.

Olszevski, N., Filho, E. I. F., Costa, L. M. D. A., Schaefer, C. E. G. R., Souza, E. D. E., & Costa, O. D. V. (2011). Morphology and hydrological aspects of black river basin, division of state of rio de janeiro and minas gerais. *Brazilian Journal of Forest Science*, *35*, 485–492.

Owolabi, S., Madi, K., Kalumba, A., & Orimoloye, I. (2020). A groundwater potential zone mapping approach for semi-arid environments using remote sensing (rs), geographic information system (gis), and analytical hierarchical process (ahp) techniques: A case study of buffalo catchment, eastern cape, south africa. *Arab J Geosci*, *13*(1184), 1–17.

Parveen, S., Praveen, B., & Akram, V. (2023). A systematic review on groundwater management: Opportunities and challenges. *Environmental Processes and Management*, 85–91.

Prabhakaran, A., & Raj, N. J. (2018). Drainage morphometric analysis for assessing form and processes of the watersheds of pachamalai hills and its adjoinings, central tamil nadu, india. *Applied Water Science*, *8*(31).

Prabu, P., & Rajagopalan, B. (2013). Mapping of lineaments for groundwater targeting and sustainable water resource management in hard rock hydrogeological environment using rs- gis. *Climate Change and Regional/Local Responses*.

Rahmani, S. A., Chibane, B., & Boucefiene, A. (2017). Groundwater recharge estimation in semi-arid zone: A study case from the region of djelfa (algeria). *Applied Water Science*, *7*(5), 2255–2265.

Sajil Kumar, P. J., Schneider, M., & Elango, L. (2021). The state-of-the-art estimation of groundwater recharge and water balance with a special emphasis on india: A critical review. *Sustainability*, *14*, 340.

Sakthivel, R., Raj, N. J., & Sivasankar, V. (2019). Geo-spatial technique-based approach on drainage morphometric analysis at kalrayan hills, tamil nadu, india. *Applied Water Science*, *9*(24).

Sander, P. (2007). Lineaments in groundwater exploration: A review of applications and limitations. *Hydrogeology jounal*, *15*(1), 71–74.

Sankriti, R., Subbarayan, S., & Aluru, M. (2021). Morphometric analysis and prioritization of sub-watersheds of himayatsagar catchment, ranga reddy district, telangana, india using remote sensing and gis techniques. *International Journal of System Assurance Engineering and Management*.

Schumm, S. A. (1954). The relation of drainage basin relief to sediment loss. *IAHS Publication*, *36*(1), 216–229.

Schumm, S. A. (1956). The evolution of drainage systems and slopes in badlands at perth amboy. *Geological Society of America Bulletin*, *67*, 597–646.

Shapiro, A. M., & Day-Lewis, F. D. (2021). Estimating and forecasting time-varying groundwater recharge in fractured rock: A state-space formulation with preferential and diffuse flow to the water table. *Water Resources Research*, *57*. https://doi.org/10.1029/2020WR029110

Shekar, P. R., & Mathew, A. (2022). Morphometric analysis for prioritizing sub-watersheds of murredu river basin, telangana state, india, using a geographical information system. *Journal of Engineering and Applied Sciences*, *69*(44).

Smith, K. G. (1950). Standards for grading texture of erosional topography. *American Journal of Science*, *248*, 655–668.

Stigter, T., Miller, J., Chen, J., & Re, V. (2023). Groundwater and climate change: Threats and opportunities. *Hydrogeology Journal*, *31*(1), 7–10.

Strahler, A. N. (1952). Dynamic basis of geomorphology. *Geological Society of America Bulletin*, *63*, 923–938.

Strahler, A. N. (1957). Quantitative analysis of watershed geomorphology. *Transactions of the American Geophysical Union*, *38*(6), 913–920.

Strahler, A. N. (1958). Dimensional analysis applied to fluvially eroded landforms. *Geological Society of America Bulletin*, *69*, 279–300.

Strahler, A. N. (1964). Quantitative geomorphology of drainage basins and channel networks. In *Handbook of applied hydrology* (pp. 439–476).

Thakur, J., Singh, S., & Ekanthalu, V. (2017). Integrating remote sensing, geographic information systems and global positioning system techniques with hydrological modeling. *Applied Water Science*, *7*(4), 1595–1608.

Thomas, J., Joseph, S., & Thrivikramaji, K. P. (2010). Morphometric aspects of a small tropical mountain river system, the southern western ghats, india. *International Journal of Digital Earth*, *3*(2), 135–156.

Wang, L., & Liu, H. (2006). An efficient method for identifying and filling surface depressions in digital elevation models for hydrologic analysis and modelling. *International Journal of Geographical Information Science*, *20*(2), 193–213.

Withanage, S. N., Dayawansa, K. D. N., & Silva, P. R. D. (2014). Morphometric analysis of the gal oya river basin using spatial data derived from gis. *Tropical Agricultural Research*, *26*(1), 175–188.

Yao, R., Liu, C., Wang, Y., Ma, T., & Yang, Y. (2021). Hydrochemical characteristics and groundwater quality assessment using an integrated approach of the pca, som, and fuzzy c-means clustering: A case study in the northern sichuan basin. *Water*, *13*(10), 1405.

Yeh, H.-F., Cheng, Y.-S., Lin, H.-I., & Lee, C.-H. (2016). Mapping groundwater recharge potential zone using a gis approach in hualian river, taiwan. *Sustainable Environment Research*, *26*(1), 33–43. https://doi.org/10.1016/j.serj.2015.09.005

Yuan, H., Yang, S., & Wang, B. (2022). Hydrochemistry characteristics of groundwater with the influence of spatial variability and water flow in hetao irrigation district, china. *Environmental Science and Pollution Research*, *29*, 71150–71164. https://doi.org/10.1007/s11356-022-20685-1

Zarour, K., Benmerzoug, D., Guermouche, N., & Drira, K. (2019). Automating the generation of comparison weights for enhancing the ahp decision-making process. *Computational Science–ICCS 2019: 19th International Conference, Faro, Portugal, June 12–14, 2019, Proceedings, Part V 19*, 573–580. https://doi.org/10.1007/978-3-030-22750-0_53

Zghibi, A., Mirchi, A., Msaddek, M. H., Merzougui, A., Zouhri, L., Taupin, J.-D., Chekirbane, A., Chenini, I., & Tarhouni, J. (2020). Using analytical hierarchy process and multi-influencing factors to map groundwater recharge zones in a semi-arid mediterranean coastal aquifer. *Water*, *12*(9), 2525. https://doi.org/10.3390/w12092525

Zhang, Y., Wu, J., Xu, B., Wang, J., & Li, F. (2021). Groundwater hydrochemistry, source identification and pollution assessment in intensive industrial areas, eastern chinese loess plateau. *Environmental Pollution*, *273*, 116367.